Assessment of SERS-active nanosensors as a tool for pH measurements within living cells

Helena E.M. Engman

Doctor of Philosophy with Integrated Study

Optical Medical Imaging with Healthcare Innovation and
Entrepreneurship

The University of Edinburgh and The University of Strathclyde

2022

Declaration of Authorship

I declare that this thesis and the work presented within has been composed by myself unless stated otherwise by reference or acknowledgement. The work presented has not been submitted, in whole or in part, in any previous application for any other degree or professional qualification.

This thesis describes the results of research carried out in the Centre for Clinical Brain Sciences and the School of Chemistry, University of Edinburgh, under the supervision of Dr Paul A. De Sousa and Prof. Colin J. Campbell. The research was funded by the Scottish Funding Council [grant number H14052 / SIRL ID: 691]; as well as the Engineering and Physical Sciences Council and the Medical Research Council [grant number EP / L016559 / 1] through the OPTIMA CDT.

Helena E.M. Engman

University of Edinburgh

2022

Abstract

Intracellular and intraorganellar pH is an essential aspect of the maintenance of proper cellular functions. Measurement of pH within cells could therefore elucidate crucial information regarding cell behaviour and pathology. Surface Enhanced Raman spectroscopy (SERS) is a method which has shown great potential as a method for pH measurement.

SERS in combination with gold nanoparticles (AuNP) covalently bound to a pH sensitive molecule, 4-mercaptobenzoic acid (MBA), was assessed as a method to measure pH within live mammalian cells. The protonation states of MBA can be detected via the change of pH sensitive peaks within its Raman spectrum, and this information can be used to determine the pH. Within this thesis the MBA-AuNP were characterised in terms of cytotoxicity, reversibility, intracellular localisation, and capability of the MBA-AuNPs to measure pH within healthy and disease model mammalian cells, specifically human embryonic stem cells and primary sheep subventricular zone (SVZ) cells from Batten Disease affected and unaffected animals, respectively.

The sensor was shown to cause no decrease in cell viability or proliferation and were able to respond to pH changes in a reversible manner. Large numbers of MBA-AuNP were shown to accumulate in perinuclear regions in close association with vesicles positive for the lysosomal marker LAMP1, but not LAMP2. Furthermore, assessment of pH perturbations in a cell model for the lysosomal storage disorder, Batten Disease, showed that the sensors are capable of discrimination of slight physiological pH changes within lysosomes.

Lay Summary

Cells are the smallest structural and functional unit of living organisms. Their existence and health is defined by physio-chemical interactions between the diverse and complex biomolecules of which they are comprised. One measure of these interactions is through the quantification of hydrogen ion concentrations, pH, as a reflection of the acidity or alkalinity of aqueous solutions outside and inside cells and compartments within. Perturbations in intracellular pH are a feature of several diseases including Parkinson's disease, Alzheimer's disease, Down's Syndrome, lysosomal storage diseases such as Batten Disease and even cancer.

Several techniques exist to measure the pH within cells and relate this back to what is going on within the cell. We have evaluated one of these techniques, Surface Enhanced Raman Spectroscopy (SERS), which uses highly focused laser light in combination with pH-sensitive molecules attached to gold nanoparticles (pH-sensors). To evaluate how well these pH-sensors work to measure pH within cells, we looked at the effect they had on the normal cell function, where they ended up within the cells, and if pH differences between healthy cells and diseased model cell could be distinguished (Batten Disease). Our study used human embryonic stem cells and primary subventricular zone (SVZ) cells from Batten Disease affected, and unaffected, sheep as models.

We found that the pH-sensors did not negatively affect normal cell growth and function, and that they can detect changes in pH. We also recorded the uptake of the pH-sensors into the cells and found that they end up in specialised compartments of the cell called lysosomes. Importantly, the pH-sensors were able to discriminate the differences in pH between healthy and Batten Disease cells.

Acknowledgements

I would like to thank my supervisors Dr Paul A. De Sousa and Prof. Colin J. Campbell for letting me carry out this PhD in their labs; OPTIMA CDT, the SFC, the ESPRC and the MRC for funding; and Dr Daniel Y.H. Soong for all your: help, guidance, and support; without you this thesis would not have been possible.

I would also like to thank the Barcelona Stem Cell bank for letting me carry out a 3-month placement with them; especially Dr Bernd Kuebler who was a joy to work with and taught me endless things about stem cell culture.

I would also like to give thanks to: Dr Tom Burdon, Dr Thomas Wishart, Samantha Eaton, and Dr Stephen Meek from the Roslin Institute, for providing me with the sheep SVZ cell line, helping me with the PPT1 assay, and providing me with the detailed information regarding their origin. These cells were crucial to some of the work within this thesis.

Finally, I would like to thank my whole family for their continuing support, I love you all.

Contents

List of Figures

List of Tables

List of Equations

1 List of Abbreviations

ATP	Adenosine 5′-triphosphate
AUC	Area under the curve
AuNP	Gold nanoparticles
BafA1	Bafilomycin A1
BCECF	2',7'-Bis-(2-Carboxyethyl)-5-(and-6)-Carboxyfluorescein, Acetoxymethyl Ester
BF	Brightfield
BSA	Bovine serum albumin
CaF_2	Calcium fluoride
CE	Chemical enhancement
ClioQ	Clioquinol
CLN3	Ceroid-lipofuscinosis, neuronal 3
CO_2	Carbon dioxide
DMEM	Dulbecco’s Modified Eagle’s Medium
EM	Electromagnetic enhancement
FBS	Foetal bovine serum
FCS	Foetal calf serum
hESC	Human Embryonic Stem Cell
HET	Heterozygous
IF	Immunofluorescence
iPSC	Induced pluripotent stem cell
KO	Knock-out

LAMP	Lysosomal associated membrane protein
MBA	Mercaptobenzoic acid
MBA-AuNP	Mercaptobenzoic acid conjugated gold nanoparticles
mESC	Mouse Embryonic Stem Cell
MFI	Mean fluorescence intensity
NBF	Neutral buffered formaldehyde
NMR	Nuclear Magnetic Resonance
PBS	Phosphate buffered saline
PC	Phase contrast
pH_i	Intracellular pH (cytoplasmic pH)
P_i	Inorganic phosphate
PPT1	Palmitoyl-protein thioesterase 1
ROCKi	Rho kinase inhibitor (ROCK, Y27632 inhibitor)
SERS	Surface Enhanced Raman Spectroscopy
SNARF	Seminaphtarodafluor
SVZ	Subventricular zone
TEM	Transmission electron microscopy
UV-vis	Ultraviolet-visible
VTN	Vitronectin
WT	Wild-type

2 Introduction

2.1 Intracellular pH

Intracellular pH is an expression of the concentration of H^+ ions within the cell, which originate from a multitude of biochemical substances and pathways as well as from the ionisation of water [1]. The cytoplasmic pH (pH_i) of cells is around 6.8-7.2, which is higher than the calculated theoretical pH_i of 6.4 [2,3]. This difference between the theoretical and actual pH_i of cells come about since the pH_i is in a state of dynamic equilibrium in which ions are transported both actively and passively across the cell membrane [4]. pH_i requires tight regulation as most processes within a cell are pH sensitive. This includes cell metabolism and growth, the structure and function of virtually all proteins, the transportation and homeostasis of ions, endocytosis, and contraction of muscle cells [5–7]. One example where pH plays an important role is the regulation of the activity of enzymes, which all have a pH optimum. For instance, changes in pH_i may alter cell metabolism through a pH-sensitive metabolic enzyme called phosphofructokinase [3]. Other enzymes, such as lysosomal proteolytic enzymes, require low pH in order to function properly, whereas enzymes residing in the cytoplasm require a pH of around 7.3 [1]. pH_i can also influence the cytoskeleton in cells by: influencing the cross-linking and polymerisation of actin and tubulin, promoting cell growth and proliferation through activation of membrane bound transporters, and influencing intracellular signalling [3].

pH_i is regulated through two main methods: cellular buffers and membrane-bound transporters. These membrane-bound transporters can be divided into five categories including: cation-H^+ exchangers, HCO_3^- dependent transporters, H^+ ATPases, Na^+ organic anion co-transporters, and Cl^- organic anion exchangers [3].

2.1.1 Compartmentalisation of the cell

Within the cell there are a multitude of different microenvironments which all play specific roles and require tight regulation of the biochemical machinery that allow cells to function. These microenvironments arise from: membrane-bound reactions, spatially polarised reactions, gradients, and from the physical compartmentalisation into cellular organelles. The pH within the various families of cellular organelles is regulated to ensure an optimal pH for their specific functions and the consensus pH values of these key organelle families from the literature are summarised in Figure 1.

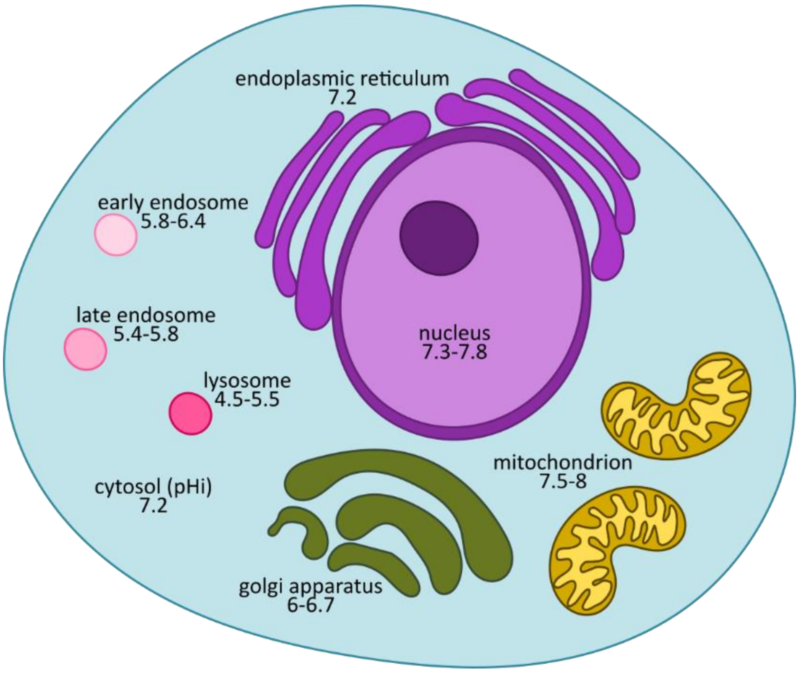

Figure 1. Examples of pH differences in cellular compartments
Illustration showing some examples of pH differences between various cellular compartments based on values in the literature [3,5,7–9].

For instance, the lysosomal pH is around 4.5-5.5, which is essential for the proper function of the proteolytic enzymes which reside within them, as mentioned in the previous section [10,11]. Without proper pH regulation of lysosomal pH, the cell would be unable to properly degrade and recycle cellular macromolecules and other by-products of metabolic processes. Regulation of pH is not just important for enzymatic degradation, but also for synthesis of macromolecules and energy production; for example, the mitochondrion has a pH of around 7.5-8 which is significantly more alkaline than of the pH_i at around 7.2 [2,3]. This difference in pH is essential for the generation of adenosine triphosphate (ATP) and is only possible due to the proton gradient across the inner mitochondrial membrane. The nucleus, which has large nuclear membrane pores that allow transport of large macromolecules, was initially believed to have the same pH as the cytoplasm. However, it has been shown that the nuclear pH is around 0.1-0.5 pH values higher than that of the cytoplasmic pH [3]. This is thought to be a result of active pH regulation by Na^+ - H^+ exchangers in the nuclear envelope [3,12].

2.1.2 Intracellular pH and disease

Even slight pH perturbations within cells and their organelles may cause cellular dysfunction and lead to, or be part of, disease development and even cell death through several processes including: perturbation of posttranslational protein modification, processing of secreted proteins, and functionality of the intracellular organelles [2,6,13]. Examples of such pathologies include neurodegenerative diseases like Parkinson’s disease, Alzheimer’s disease, Down’s Syndrome, lysosomal storage diseases such as Batten Disease, and even cancer [14,15]. Because pH plays a crucial role in almost all cellular processes it has gained an increasing interest for the study, diagnosis, and treatment of various conditions and diseases [16,17].

2.1.3 pH in stem cells and the role of pH during differentiation and pluripotency

Stem cells can be defined as a cell that is able to self-renew indefinitely as well as being able to differentiate into various cell types. Human embryonic stem cells (hESC) are harvested from the inner cell mass of the developing blastocyst and are able to give rise to all three germ layers, the ectoderm, mesoderm and endoderm [18]. Induced pluripotent stem cells (iPSC) are another type of pluripotent stem cell utilised in research and result from the reprogramming of somatic cells with specific transcription factors [19,20]. Both hESC and iPSC hold great potential for the field of regenerative medicine because of their ability to turn into any cell type; however, application of these stem cells to regenerative medicine requires homogeneity of the stem cell population. It is known that hESC exist as heterogeneous populations *in vitro* and that genetic changes may occur in response to selective pressures that are applied during culturing [21–23]. It is therefore important to understand the various aspects that affect stem cell differentiation potential and self-renewal. As mentioned in the previous sections, pH greatly influences the function of proteins and enzymes in all cells, so it is reasonable to assume it also plays a role in the myriad of signalling pathways that occur during the self-renewal and differentiation of a stem cell.

For instance, lysosomal acidification via the dysregulation of the vacuolar H^+-ATPase activity has been suggested to be affected during cellular aging, and it has been shown that small molecules can be used to promote lysosomal acidification and inhibit senescence in mesenchymal stem cells [15,24]. Studies have also suggested that the reprogramming efficiency of somatic cells into iPSC cells decreases with increasing age, for example: murine dermal fibroblasts isolated from young mice showed a two-fold increase in reprogramming efficiency compared to cells isolated from older mice [25,26]. This finding has further been validated in other studies with older cells showing reduced replicative ability and lower reprogramming efficiencies [27,28]. The steady-state pH_i of human iPSCs has been shown to be more alkaline than in most adult cells, at a pH of 7.5-7.68 compared to 7.2 [29]. An increased pH_i has been implicated in the efficient differentiation of both Drosophila adult prefollice and follicle stem cells as well as mouse embryonic stem cells (mESC) [30].

It is clear that pH_i and intraorganellar pH plays a significant role in normal cell function, and also during self-renewal and differentiation of stem cells. To realise the true potential of these cells in tissue engineering, disease modelling, and regenerative medicine it is essential to unveil the various mechanisms that influence their fate and function, one of these being pH.

2.2 Raman spectroscopy and SERS

2.2.1 Raman spectroscopy

Raman scattering was first described in a *Nature* paper in 1928 by Raman and Krishnan [31]. Raman scattering is a phenomenon where an inelastic scattering of light occurs, as a result of the loss or gain of energy of incident photons, in response to the vibrational and rotational motion of bonds within the analyte molecule [32]. In elastic scattering (Rayleigh scattering) the kinetic energy of the incident photon stays the same, in comparison inelastic scattering (Raman scattering) which results in the loss (Stokes scattering) or gain (Anti-stokes scattering) of energy (Figure 2). Most photons scatter elastically; only a very small number (about 1 in 10^6-10^{10}) scatter inelastically, resulting in a relatively weak signal compared to elastic scattering [32,33].

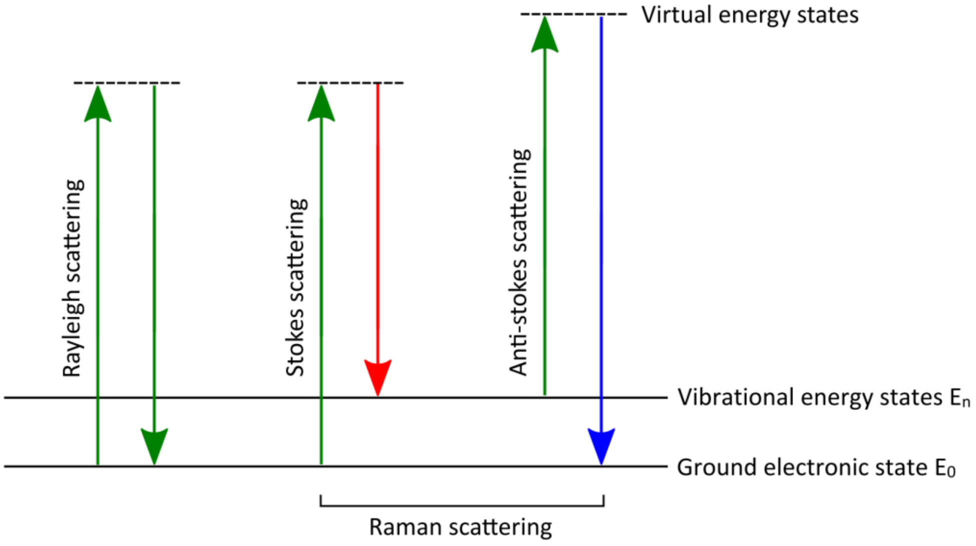

Figure 2. Jablonski diagram.
Diagram showing the process of Rayleigh and Raman scattering.

Raman spectroscopy is a non-invasive and non-destructive technique which utilises a monochromatic laser beam to excite an analyte molecule resulting in light scattering. The resulting Raman scattering can then be detected and a Raman spectrum can be constructed by plotting the scattered intensity on the Y-axis as a function of the change in intensity between the incident and scattered photons [34]. This change in intensity between the incident and Raman-scattered light is known as a Raman shift, and is measured as the shifts in wave numbers, which is the inverse of wavelength, cm^{-1}. Raman spectra are a unique collection of Raman peaks associated with the vibration of distinct chemical bonds and/or functional groups within the analyte molecule and can therefore be thought of as a molecular fingerprint

2.2.2 Surface-enhanced Raman spectroscopy

One of the main drawbacks of Raman spectroscopy is that it usually results in a weak signal due to the low number of photons that scatter inelastically. Fortunately, the weak Raman signal can be enhanced by the adsorption of molecules onto metal surfaces, a technique named Surface-enhanced Raman spectroscopy (SERS). SERS was first discovered by accident in 1974 by Fleischmann and co-workers when they discovered an enhancement of signal while measuring the Raman scattering of pyridine on rough silver electrodes [35]. The enhancement effect of SERS can be up to 14 orders of magnitude greater compared to traditional Raman spectroscopy, and can enable single molecule detection in some cases [35]. This enhancement effect is a result of the generation of an oscillating field of valence electrons (surface plasmon) when the electric component of the laser beam interacts with the metal surface (Figure 3). Under these circumstances when the correct laser wavelength interacts with the metal surface it causes the surface plasmon to resonate leading to both an enhancement of the incident and scattered electromagnetic radiation from the laser. There is a general consensus in the literature that this enhancement effect arises from both an electromagnetic (EM) enhancement factor and a chemical enhancement (CE) factor [36]. The EM factor is thought to be the main contributor of the enhancement whereas the CE factor only contributes a much smaller part. The metal substrate is usually made out of silver or gold; but, although a greater enhancement can be achieved by using silver, gold is the preferred choice due to its higher biocompatibility and because it has been shown to be non-toxic in cells making it ideal for studies in cells [37]. SERS substrates come in various shapes and sizes including spheres, nanostars and nanorods; and both of these properties influences the surface plasmon resonance and the corresponding enhancement effect [35,38].

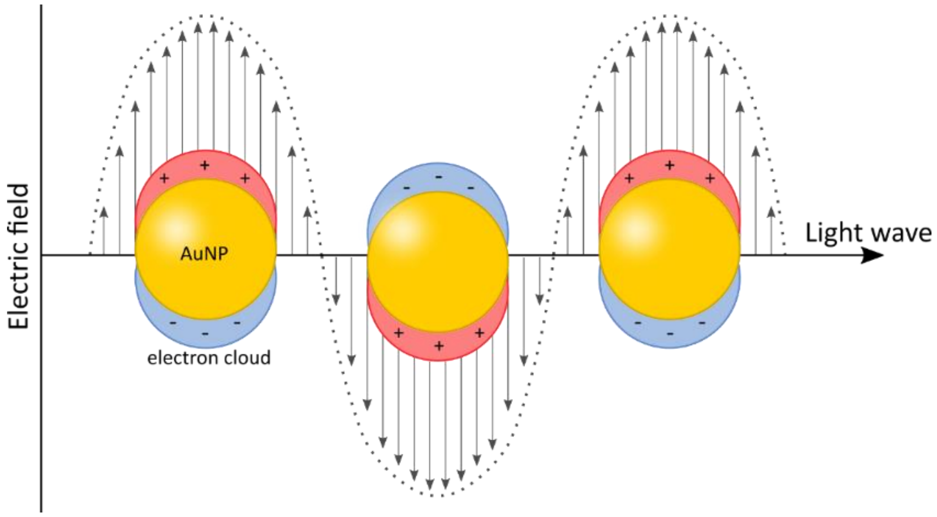

Figure 3. Surface plasmon resonance of gold nanoparticles (AuNP)
Illustration depicts the response of the oscillating electron cloud (surface plasmon) on the surface on a gold nanoparticle in response to the electromagnetic light wave from a laser. When a suitable wavelength is used it causes a resonance of the surface plasmon which increases the signal intensity of the incident and scattered laser light. Arrows emanating from the AuNP represent an increase in the amplitude of the light wave and an increase in signal intensity.

Another important factor to consider when utilising SERS or Raman spectroscopy in live cells is the wavelength of the laser. Shorter laser wavelengths in the visible spectrum have been demonstrated to both degrade and cause photodamage in cells even when being used at lower powers and with shorter acquisition times [39]. Conversely, because cells are invisible to near-infrared laser light, lasers in the near-infrared spectrum cause less damage [40]. Near-infrared lasers also cause less autofluorescence of the sample compared to lasers in the visible spectrum. However, there are advantages to shorter wavelengths as well as they are able to scatter more photons than longer wavelengths leading to a stronger Raman signal. Therefore, it is important to weigh the strengths and weaknesses of each laser wavelength before choosing an appropriate laser for each experiment.

The metal nanoparticles used in SERS may be functionalised with various reporter molecules which respond to different conditions within cells such as Redox potential or pH [8,41–44]. Changes to the structure of these molecules in response to the surrounding environment causes changes in the molecular fingerprint corresponding to their Raman spectra which allows for the determination of Redox potential or pH within cells. The use of SERS to measure pH will be discussed in further detail in section 2.3.2.

2.3 Methods of measuring Intracellular pH

Due to the significance of pH regulation within biological systems, several studies have been performed to create various methods for intracellular and organellar pH sensing. These methods include optical techniques such as fluorescent and surface-enhanced Raman (SERS) probes, electrodes and nanoneedles, and Phosphorus 31 nuclear magnetic resonance (^{31}P NMR), all of which will be discussed in the sections below.

2.3.1 Fluorescence-based techniques

Perhaps the most widely used pH probes are based on fluorescent dyes (fluorophores) which responds to changes in pH. The technique allows the study of pH within both whole cell populations or within individual cells and can be accessible to most labs as fluorescent microscopes are commonly available at research facilities. Fluorescent probes rely on the excitation of a fluorophore at a certain wavelength and the collection of the resultant emitted light. Some examples of fluorescent pH probes include BCECF, Seminaphtarodafluor (SNARF), LysoSensor probes, and Oregon green dyes [7].

BCECF is perhaps one of the most popular pH_i indicators [11,45]. BCECF has a pK_a of 6.98 which makes it ideal for the measurement of cellular pH_i as it is sensitive within a pH range of 6.0-8.0 [46]. It is also ratiometric, since it has what is called an isosbestic point, which is a point in the spectra insensitive to pH (Figure 4). The isobestic point is a great advantage as it allows normalisation of the pH sensitive region of the spectra which may either reduce or eliminate variability caused by photobleaching. BCECF requires dual-excitation of the pH insensitive region which is excited at a wavelength of ~440 nm, and the pH sensitive peak at ~490 nm, the pH is then calculated by determining the ratio of the emission intensity at 535 nm to the emission intensity of the isobestic point at ~454 nm [7]. One of the disadvantages of BCECF include a time lag between the acquisitions at 440 nm and 505 nm, which may cause artefacts caused by rapid cellular movement. BCECF has also been shown to exhibit high phototoxicity to cells [45,47]. To determine the pH values of the recorded spectra a calibration is generated using a nigericin/high-potassium method at the end of each experiment. Nigericin is a H^+/K^+ ionophore, which in combination with strongly pH-buffered high-concentration K^+ solutions equilibrate the extracellular pH with the intracellular pH and eliminates all proton gradients. Using this method, spectra are acquired for three different pH solutions and a calibration curve is plotted [7].

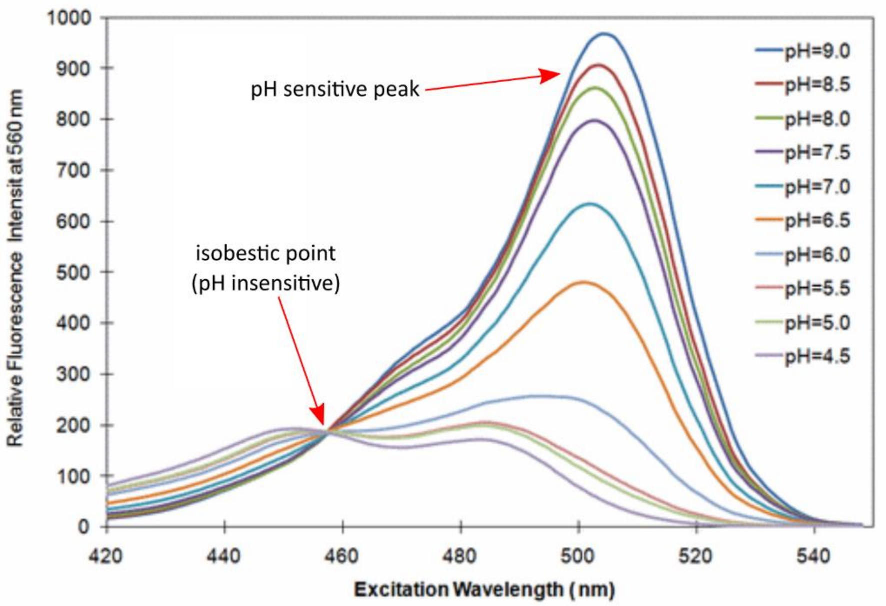

Figure 4. BCECF fluorescent spectra, example of an isobestic point
Figure shows the fluorescent spectra of BCECF. The crossover point at 454 nm is what is known as an isobestic point, where the intensity of the fluorescent signal remains constant regardless of pH. The peak at 535 nm is pH sensitive and its intensity increases as pH increases.
Figure modified from Abpbio.com [48].

SNARFs are another type of pH sensitive fluorescent dyes which also display an isobestic point, however, SNARF dyes exhibit dual emission which makes them much more desirable compared to pH_i indicators such as BCECF which requires dual excitation and exhibit high phototoxicity. Examples of SNARFs include SNARF-1, SNARF-4F and SNARF-5F, which have pK_a values of 7.5, 6.4 and 7.2 respectively [49]. These dyes have been used to measure the pH within cells such as hiPSC derived endothelial cells, mammalian cell spermatozoa, and adult rabbit cardiac myocytes [45,50,51].

LysoSensor dyes and Oregon Green 488 are some other commonly used pH sensitive fluorophores. LysoSensor and Oregon Green 488 have pK_a of 5.1 and 4.7 respectively, making them more suited to the measurement of acidic organelles than BCECF and SNARFs [11].

In addition to the already wide variety of commercially available fluorescent pH sensors, more continue to be developed, and techniques have been developed allowing the precise tuning of the pK_a of the specific indicators by chemical modification of their chemical structure [11,52–54].

2.3.2 Surface-enhanced Raman spectroscopy

As covered in section 2.2 Raman spectroscopy is an optical method that involves the inelastic scattering of photons by a laser light source. Surface-enhanced Raman spectroscopy (SERS) is a method whereby the analyte molecule is attached to or put in close proximity to a metal surface such as gold or silver, which enhances the inherently weak Raman signal by several orders of magnitude. By covalently attaching pH sensitive molecules to metal nanoparticles SERS has been used to measure the pH within a wide variety of cell types such as NIH/3T3, MCF7, A549, HeLa, CaSki, EA.hy926, macrophages, adenocarcinoma and more [8,37,42,55–65]. Some examples of pH sensitive molecules which can be used for SERS pH sensing include 4-mercaptobenzoic acid (4-MBA), 4-mercaptopyridine (4-Mpy), 4-aminobenzenethiol (2-ABT) and 4-aminophenol (4-ATP) and 2/3,5-dimercaptobenzoic acid [66]. Out of these 4-MBA and 4-Mpy are the most widely used in SERS-based pH assessment and allow for pH assessment within a wide range between pH 4 to 9 [67].

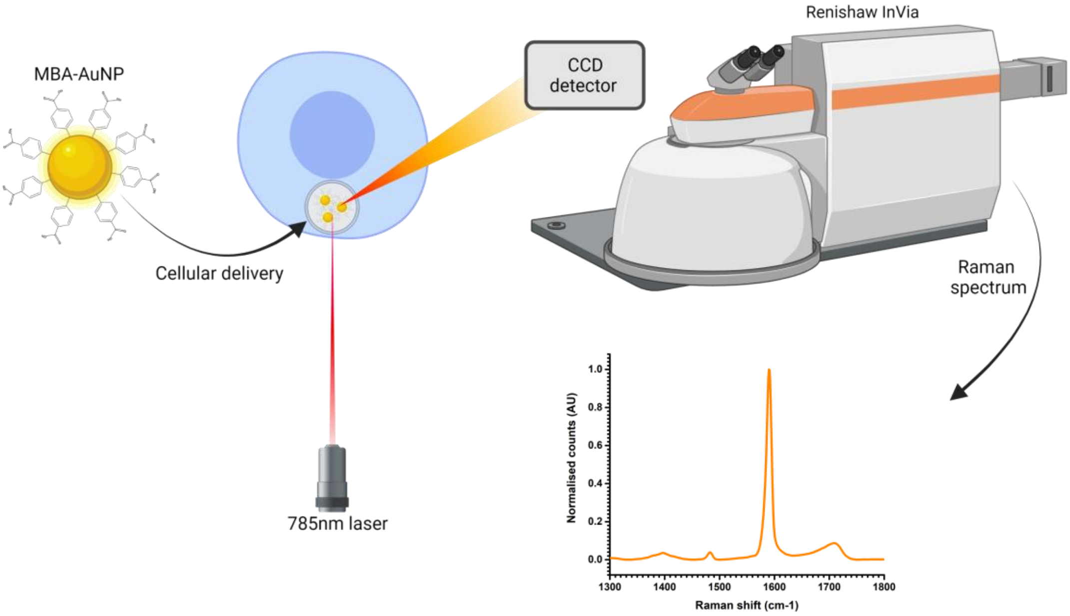

Figure 5. Raman spectroscopy illustration
Schematic diagram of experimental procedure for measuring spectra from mercaptobenzoic acid functionalised gold nanoparticles (MBA-AuNP) within living cells. Created with BioRender.com.

2.3.3 Nanoneedles

Another specialised technique to measure pH_i is by using nanoneedles. Nanoneedles are also known by several other names within the literature such as: nanowires, nanospears, nanocapillaries, nanostraws, nanopipettes, nanotubes, nanopillars, nanoelectrodes; just to name a few [68]. To measure pH using nanoneedles they are covalently conjugated to molecular probes which respond to changes in pH. These molecular probes may either be optical or electrochemical in nature. For example, pH sensitive fluorophores in combination with a pH insensitive reference fluorophore attached to Si nanoneedles have been used to ratiometrically measure pH within cells. These types of biodegradable nanoneedles with pH sensitive fluorophores have also been used in order to simultaneously deliver nanoparticles and measure pH within cells [69]. Additionally, microneedles have been used in conjugation with SERS for the measurement of redox potential and pH simultaneously in rat joints [70]. Some disadvantages with using nano and microneedles are that they may be complicated to fabricate and precisely insert and are quite invasive in nature [68,71].

2.3.4 NMR

Another technique for the determination of pH_i is the use of ^{31}P NMR [72–74]. All cells contain inorganic phosphate (P_i) within their cytosol. Since the P_i has been shown to display a chemical shift in response to pH within the range of 6.0 and 7.3, ^{31}P NMR has been extensively used to quickly, quantitatively and noninvasively monitor the pH_i. Despite its extensive study and potential there are several drawbacks to the technique: the chemical shift between the protonated and deprotonated states of P_i is relatively weak, the concentration of P_i varies in response to the cells metabolic state and the fact that the pK_a of Pi is strongly influenced by ions which may vary greatly between cellular organelles. These drawbacks may prevent the accurate detection of spectra and renders the technique ineffective for the measurement of organelles with a pH less than 6 and between pH variations that are less than 0.2 pH units apart [72]. In addition, ^{31}P NMR has a fairly low sensitivity and requires high cell densities, which can cause complications as some cells may suffer oxygen and nutrient depletion resulting in a heterogeneous sample [73]. In order to overcome some of the drawbacks of ^{31}P NMR pH probes that are capable of measuring acidic organelles, and ratiometric pH probes based on slow-proton-exchange have been developed [72,75].

3 Project Aims

The primary aim of the experiments presented in this thesis was to explore SERS as a tool to measure the pH within cells using gold nanoparticles covalently bound to a pH sensitive molecule, 4-mercaptobenzoic acid (MBA), the pH sensor. This exploration focused on application to human embryonic stem cells and study of a lysosomal storage disorder as contemporary and high value cell models and disease contexts for which the ability to assess pH_i would have current demand and research utility.

Research began with assessment of biocompatibility and cytotoxicity of the pH-sensor and its ability to change in response to pH in a reversible manner. Next, experiments assessed the sensitivity and accuracy of the pH sensor to measure pH within cells. To do this the location of the sensor within cells had to be determined to draw conclusions on the biological significance of the acquired measurements. The response of the cells to pH changing stimuli was also assessed to determine the sensitivity of the sensor. Finally, experiments applied SERS sensors to a disease model known to display dysfunctional pH to determine if they are suitable to assess pH in a biological setting.

4 Materials and Methods

4.1 Cell culture

4.1.1 Haemocytometry

For experiments where single cell suspensions were required, the cells were manually counted using a Neubauer haemocytometer. Cells were washed with PBS, no calcium, no magnesium (-/-, Gibco, #14190094) and incubated with CTS^{TM} TrypLE^{TM} Select enzyme (Gibco, #1285901) for either 5 min (hESC) or 8-10 min (SVZ cells) at 37^{o}C. The cells were then dislodged from the vessel and pipetted to yield single cells, spun down at 200 x *g* for 2 min, and resuspended in appropriate media. 10 µL of the resuspended cells were then mixed with 10 µL 0.2% Trypan Blue on parafilm. The cell concentration (cells / µL) was determined using the equation below.

$$\frac{Cell\ count}{Quadrants\ counted\ x\ 0.1} \times 2 = Concentration\ (cells\ per\ \mu L) \qquad \textbf{\textit{Equation 1}}$$

4.1.2 Maintenance of cell lines

4.1.2.1 Human Embryonic Stem Cells

Human embryonic stem cells (hESC) were maintained in mTESR1 medium (Stemcell Technologies, #85850) in vitronectin (VTN-N, Gibco, # A14700) coated 6-well plates. Once confluent, the cells were passaged in clumps using ReLeSR^{TM} (Stemcell Technologies, #05872) according to manufacturer protocol, and normally split at a 1:20 ratio every 5-7 days.

For single cell passaging the cells were washed with PBS (-/-) and detached with CTS^{TM} TrypLE^{TM} Select enzyme (Gibco, #1285901) unless stated otherwise. ROCK inhibitor Y-27632 (ROCKi, Biotechne Tocris, #1254) was added to the medium at a final concentration of 10 µM and removed the following day.

For Raman experiments Penicillin-Streptomycin (Gibco, #1507) was supplemented to the medium at a final concentration of 1%.

4.1.2.2 *Sheep subventricular zone cells*

Primary sheep subventricular zone (SVZ) cells were generously donated from Dr Thomas Burdon's lab, Roslin Institute.

The method of collection and derivation of these cell lines were according to the protocol below, provided by Dr Stephen Meek, Roslin Institute, who dealt with the tissue and was involved in the derivation of the cell line, with added information from Dr Thomas Wishart and Samantha Eaton:

"Sheep were culled by overdose of barbiturate at 3 months of age as part of a natural history study. Tissue was isolated from the anterior horn of the subventricular zone (SVZ) by Thomas Wishart, Roslin Institute. The SVZ was dissected and placed in Neurobasal medium (Life Technologies, #21103049) on ice. The tissue was cut into smaller fragments using a scalpel then transferred to a 50 mL tube, washed with 10 mL Neurobasal medium, and centrifuged at 700 x *g* for 3 minutes. The pellet was resuspended in 10 mL Accutase (Life Technologies, #00455556) and incubated at 37^{o}C for 10 minutes. The SVZ fragments were disrupted by pipetting several times. Following disruption, 20 mL PBS was added, and the fragments allowed to pellet under gravity for 5 minutes. The supernatant, containing dissociated cells, was transferred to a separate tube, and retained. A second round of dissociation was performed on the remaining fragments using 5 mL Accutase. The supernatants were pooled and centrifuged at 1000 x *g* for 4 minutes. The final pellet was resuspended in 3 mL Neurobasal medium and 200 µL plated onto a gelatinised well of a 6-well plate in 3 mL of fibroblast culture medium [G-MEM (Sigma, #G5154), 10% FBS (Gibco, #10500064) 1xNEAA (Gibco, #11140035), 1 mM sodium pyruvate (Gibco, #11360039), 2 mM L-glutamine (Gibco, #25030024), 0.1 mM β-mercaptoethanol (Gibco, #31350010)]. Medium was changed every two days. After approximately 7 days the cells had reached 90 % confluency and were re-plated into a gelatinised T75 flask. The cells were passaged 1:8 every 3-4 days."

Six of the derived cell lines were donated from Dr Thomas Burdon's lab. Details of each cell line are found in Table 1.

Table 1. Sheep SVZ cell line animal origin details

Sheep number	Genotype	Sex	Age
75	WT	Male	50 days
79	WT	Male	49 days
77	HET	Male	49 days
78	HET	Male	49days
73	KO	Male	52 days
80	KO	Male	50 days

Once received in our lab the cells were maintained in DMEM (Gibco, #13476146) supplemented with 1% Penicillin-Streptomycin and 10% foetal calf serum in 0.5% gelatin-coated tissue culture flasks. For passaging, cells were washed with PBS (-/-) and detached using CTS^{TM} TrypLE^{TM} Select enzyme and split at a 1:10 ratio.

4.1.3 Cryopreservation

For cryopreservation, cells were frozen in CryoStor®CS10 freezing medium (Stemcell Technologies, #07930). Cells were detached from vessels using appropriate methods and resuspended or pooled in fresh medium. The cells were then spun down at 200 x *g* for 2 min and supernatant was removed. The cell pellet was resuspended in freezing medium and aliquoted into an appropriate number of cryotubes. The cryotubes were placed in a Mr Frosty unit and placed in a -80^{o}C freezer overnight. Samples were finally transferred to liquid nitrogen deep storage.

4.1.4 Thawing

Cells were quick-thawed at 37^{o}C in a water-bath until only a small ice pellet remained. The cryotube was wiped with ethanol and transferred to a tissue culture cabinet. Contents were transferred to a 15 mL falcon tube, and 10 mL of appropriate media was added to the falcon tube dropwise. The cells were then spun at 200 x *g* for 2 min, supernatant was removed, the tube was gently tapped to dislodge cell pellet and resuspended in medium. Resuspended cells were added to plasticware coated with appropriate matrix if needed.

4.1.5 Growing cells on CaF_2 substrate

4.1.5.1 Coating of CaF_2 discs for Raman spectroscopy

For Raman spectroscopy the cells were grown in 12-well plates on 20 mm x 2 mm calcium fluoride (CaF_2) discs to minimise background signals. To clean the discs, they were left overnight in 1% Alconox solution, gently scrubbed with a sterilised toothbrush, and rinsed thoroughly under running water. The discs were sterilised by soaking in 70% ethanol for minimum 10 min, after which the ethanol was removed, and the discs were left to airdry. For hESC, discs were coated with 0.01% poly-l-lysine (molecular weight 70 000-150 000) for 10 min followed by 3 washes in sterile water. The discs were then left to air-dry overnight in a tissue culture hood.

The following day the discs were coated with either 0.3 mL/disc VTN-N for at least an hour at room temperature (for hESC culture), or 0.3 mL/disc 0.5% gelatin for minimum 10 min at room temperature (for SVZ cell culture). The VTN-N or gelatin was aspirated before the addition of cells and medium to the well, and the plates were transferred to a humidified incubator at 37°C and 5% CO_2.

4.1.5.2 Giemsa staining

On day 0 the RC9 cells were passaged as clumps using 0.5 mM EDTA onto either CaF_2 discs or tissue culture treated plastic coated with either nothing, vitronectin alone, or poly-l-lysine and vitronectin together (Figure 6). The next day phase contrast images were recorded. On day 3 the cells were fixed in 70% ethanol followed by Giemsa staining for 5 min and rinsed in PBS until excess was removed. The cells were then left to dry. The wells were then imaged using an iPhone 7 Plus phone camera to document the attachment on the various surfaces.

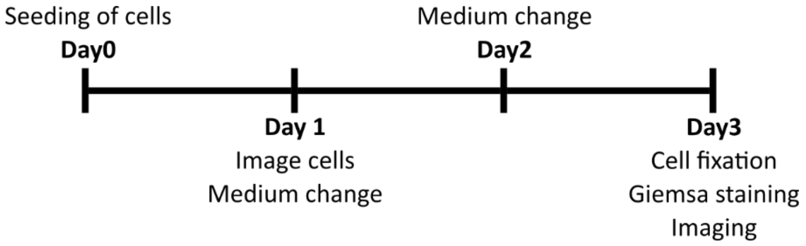

Figure 6. Timeline for Giemsa staining
Cells were seeded on Day 0 and left to grow until Day 1 when medium was exchanged, and the cells were imaged using phase contrast imaging. Medium was changed again on Day 2, and the cells were finally fixed and stained using Giemsa stain on Day 3.

4.1.6 Drug treatments

4.1.6.1 Bafilomycin A1 (BafA1)

Bafilomycin A1 (Cell Signalling Technology: #54645) was reconstituted in DMSO to obtain a 1mM stock solution as per manufacturer instructions and then frozen in aliquots. Before adding to cells, the frozen aliquots were thawed and diluted in an appropriate amount of culture medium.

4.1.6.2 Clioquinol (ClioQ)

ClioQ (Sigma-Aldrich Chemie GmbH, #33931) was purchased from Merck Life Sciences UK, weighed out and reconstituted in DMSO to obtain a 1mM stock solution. ClioQ was diluted in medium and was added straight into wells containing cells to obtain a final concentration of 250nM.

4.2 Nanoparticle functionalisation

4.2.1 MBA-AuNP

A 1mM stock solution of 4-mercaptobenzoic acid (MBA) was prepared by dissolving 1-3 mg of MBA powder (Sigma, #662534-5G) in 100% ethanol, followed by a 1:10 dilution in tissue culture grade water. The 1mM stock solution was transferred to a tissue culture hood and sterile filtered once using a 0.22 µm filter.

MBA functionalised gold nanoparticles (MBA-AuNP) were prepared by first sterile-filtering 100nm citrate buffered gold nanoparticles (CytoDiagnostics Inc., #742031) through a 0.22 µm filter. The sterile-filtered AuNP were then mixed with 100 µL of sterile 1 mM MBA solution and left overnight at room temperature in the dark.

The following day, the MBA-AuNP were mixed gently and washed twice by centrifugation at 400 x *g* for 30 min. All but 200 µL supernatant was removed and replaced with sterile tissue culture water between washes.

4.2.2 UV-vis spectroscopy

For concentration determination, the absorbance of the functionalised nanoparticle conjugates was determined using a Varian Cary 50 Bio UV/Visible Spectrophotometer. Functionalised MBA-AuNP (400 µL) was measured in fluorimeter cuvettes at wavelengths between 200-900 nm with baseline correction and fast scanning. Concentration was determined using the Beer Lambert Law (Equation 2), where ABS = absorbance, 1.57 x 10^{11} = Molar extinction coefficient for 100AuNPAuNcm^{-1} M^{-1cm-1} [76], and 1 is the path length of the cuvettes in cm. For determination of particles/mL Equation 3 was used, where 3.84 x 10^{9} is the stock concentration in particles per ml of the purchased nanoparticle solution.

$$\frac{ABS}{1.57\ x\ 10^{11}\ x\ 1} = Concentration\ (M) \qquad \textit{Equation 2}$$

$$ABS\ x\ 3.84\ x\ 10^{9} = particles/mL \qquad \textit{Equation 3}$$

4.3 Surface Enhanced Raman Spectroscopy

All surface enhanced Raman spectroscopy (SERS) measurements were acquired using a Renishaw InVia microscope with upright configuration equipped with a 785nm diode laser. The Renishaw InVia was equipped with a Renishaw CCD Camera (1040 x 256), and all spectra were acquired with a laser grating of 1200 l/mm (633/780) between Raman shifts of 1300-1800cm^{-1} with a centre of 1400cm^{-1}.

4.3.1 MBA-AuNP pH calibration curve

To determine pH in cells using the MBA-AuNPs a calibration curve was made. Droplets of MBA-AuNP (5 µL/ drop) was dried onto CaF_2 slides. For the measurements 20 µL of standard pH solution (pH4 - pH10) was placed onto the dried MBA-AuNPs and an immersion objective (60X, Olympus LUMPlanFL 60X NA1.0) was lowered into the droplet. Spectra were acquired for 1 s at 0.5% laser power from 6 locations/droplet along the outer perimeter of the dried MBA-AuNP droplet using a point map acquisition. All data were smoothened using 13 points, baselined, cropped, and normalised to 1 in Wire 4.4.1 software. The area under the curve and peak at the 1380-1450 and 1680-1730 regions were extracted using a Mathematica script written by Dr Daniel Y.H. Soong (Supplementary files 1 and 2). The data were then taken into OriginLab software and plotted to obtain the calibration curves.

4.3.2 Reversibility test

MBA-AuNP were dried onto CaF_2 discs as described in section 4.3.1. Standard pH buffers of either pH4 or pH10 were added onto the dried MBA-AuNP in an alternating fashion with water washes in between. Spectra were acquired using a point map acquisition for 1 s at 0.5% laser power from 6 locations along the outer perimeter of the dried MBA-AuNP. Maps (and washes) were repeated 3x per pH on different days using 3 different batches of MBA-AuNP. Data was extracted and analysed as in section 4.3.1.

4.3.3 Intracellular SERS measurements

For all intracellular SERS measurements, an Olympus LUMPlanFL 60x NA1.0 water-immersion objective was used. In preparation for SERS the cells were grown on CaF_2

discs in 12 well plates. The CaF_2 discs were prepared as described in section 4.1.5.1. MBA-AuNP was added straight to wells containing cells to make a final concentration of 2.5×10^{-13} M (1.5×10^{8} particles/mL) and incubated overnight unless stated otherwise. Before imaging the cells were washed 3x with PBS followed by the addition of fresh medium. The cells were transferred to the microscope and kept in a 37°C heated benchtop incubator until imaging. Just before imaging the CaF_2 discs with cells were placed in a 35mm Petri dish with fresh room temperature medium to prevent temperature fluctuations. Cells were normally imaged for between 20-40 min. To determine the position of AuNPs within cells the transmitted light source was turned off, leaving only chamber-mounted reflected light sources on, and exposure was set to approximately 60s to acquire scattered light from the AuNPs (Figure 41). Point spectra were then manually acquired from points of interest using 10% laser power for 5 s. Data was processed and extracted as described in section 4.3.1.

4.4 PrestoBlue cytotoxicity assay

On day 0, RC9 hESC cells were passaged as single cells using CTS^{TM} TrypLE^{TM} Select enzyme and 5000 cells/well were seeded into 96 well white walled plates in mTESR1 medium supplemented with 10 µM ROCK Y-27632. The medium was replaced on day 1 with fresh mTESR1 medium and the cells were left to grow overnight. On day 2 the medium was replaced with mTESR1, then MBA-AuNP or controls were added to the wells before overnight incubation. On day 3 PrestoBlue™ Cell Viability Reagent was added to the wells at a 1/10 dilution and the plates were read after 1 hour of incubation using a GloMax® Discover Microplate Reader with manufacturer settings, using an excitation filter of 520 nm and an emission filter of 580-640 nm. The experiment was performed in triplicate wells and repeated on 3 separate days.

4.5 Microscopy

4.5.1 Timelapse

RC9 hESC cells (5 x 10^4 cells/well) were seeded as single cells with rock inhibitor (ROCKi) into single wells of a glass-bottomed 6-well plate (0.17 mm coverslip-thickness) and grown for 3 days. On day 3, MBA-AuNP were added straight to the well just before imaging on a Zeiss Observer 7 microscope with a 37°C environmental chamber and maintained at 5% CO_2. A 63x Plan-Apochromat 1.4 NA phase contrast oil-immersion objective was used to acquire multiple fields of two-channel Phase Contrast and Brightfield images from this well with 10 min intervals between acquisitions for 16 hours using software autofocus on the Phase Contrast channel before each timepoint. Images at different focal planes were acquired by setting a Z-stack to start at the coverslip interface and end at the top of the cells in the field. While these Z-stacks are not confocal images, they allowed capture of AuNPs at multiple focal levels because they do not transmit light and therefore create dark spots in the acquisition field (Figure 7). A Hamamatsu Flash 4 LT+ sCMOS camera (Hamamatsu Photonics K.K., Hamamatsu, Japan) with 2048 x 2048 pixels was used to acquire each channel with exposures of 25 ms (Phase Contrast), and 10 ms (Brightfield).

The resulting acquisitions were imported into Zen, Volocity, and ImageJ for processing and creation of montage timelapse figures and .avi movies.

Image processing was as follows: individual fields were contrast adjusted to highlight the cellular features of interest in Phase Contrast (4500 lower threshold, 11500 upper threshold), and AuNPs in brightfield (8300 lower threshold, 12000 upper threshold).

Since the AuNPs are non-transmitting, they create dark spots on the image field while the cellular material, without contrast optics, transmit almost all incident light. As such, standard greyscale LUT images for brightfield were processed with a minimum intensity Z-projection rather than a maximum intensity projection resulting in light-background images with dark spots (Figure 7, A). Conversely, to create images of bright AuNPs on a dark background for purposes of visualisation, an inverse LUT was applied to the brightfield images with contrast set to effectively binarise the image (8800 lower threshold and 10000 upper threshold) (Figure 7). These inverted LUT binarised z-stacks were exported into ImageJ where a maximum intensity projection was conducted to create flattened multi-focus timelapse images which were then combined with a single plane from the matching Phase contrast timelapse which most clearly showed the motility of the cell margin and uptake of AuNP by the cell from the surrounding matrix (Figure 7, C and D).

The resulting two-channel Phase Contrast and binarized brightfield timelapse images were pseudocoloured grey (PC) and yellow (BF) to enhance visibility and clearly show the AuNP and cellular processes in overlaid timelapse movies (Movies 1-3).

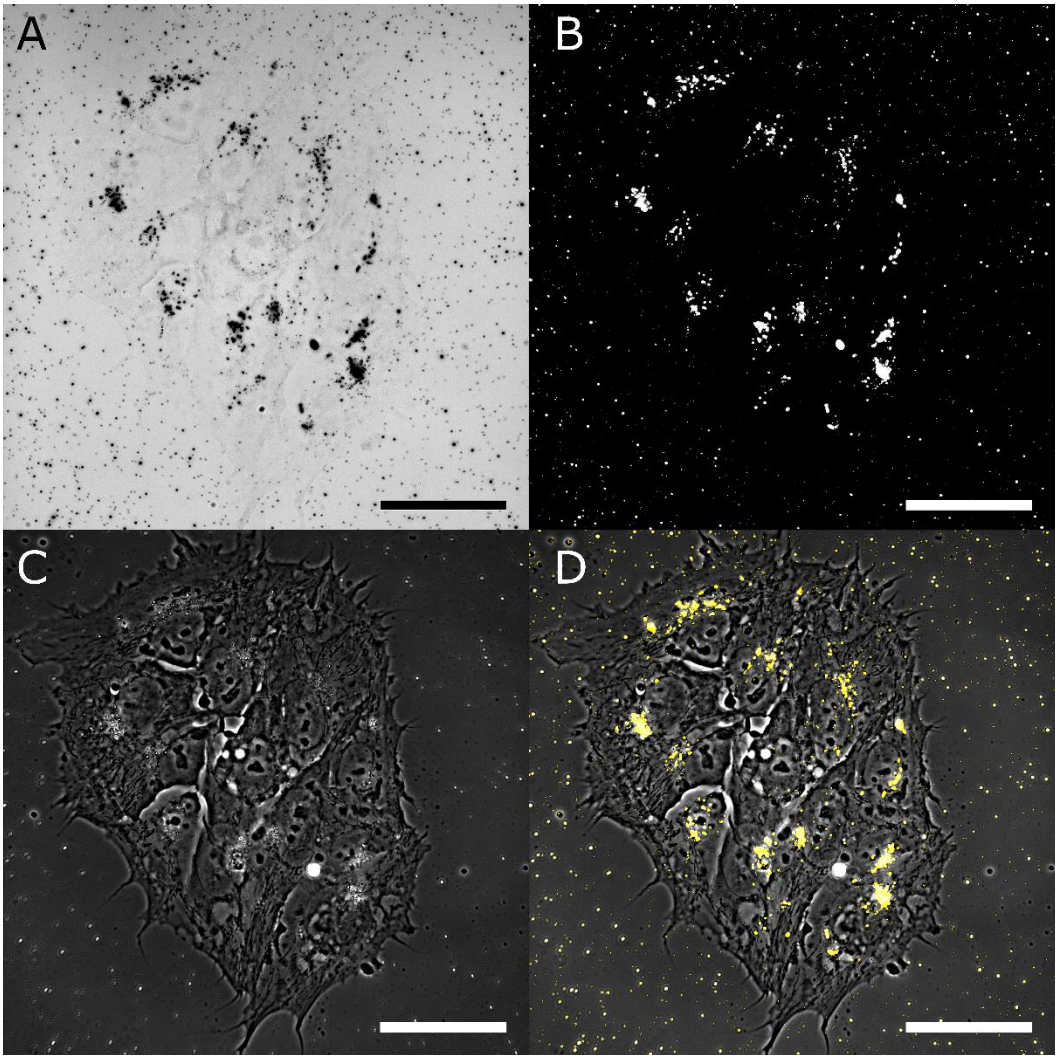

Figure 7. Inversion and binarisation of Brightfield images from timelapse
Brightfield image of a single timepoint of a single field from a timelapse acquisition of hESC grown on glass-bottomed multi-well plates. (A) shows a minimum intensity Z-projection with histogram contrast set to 8300 levels lower threshold and 12000 upper threshold to highlight dark (non-light-transmitting MBA-AuNP. (B) Shows the same image displayed in an inverted LUT with contrast set to 8800 lower threshold and 10000 upper threshold, creating a pseudobinarised image that clearly show bright MBA-AuNP. (C) Shows the phase contrast of the same cell colony, and (D) shows the phase contrast image overlaid with the inverted LUT brightfield image Pseudocoloured yellow clearly highlighting the MBA-AuNPs. Scalebar = 50µm.

4.5.2 LAMP1 and LAMP2 imaging

4.5.2.1 Immunofluorescence staining

RC9 hESC cells were grown in poly-l-lysine and vitronectin coated glass-bottomed 12-well plates and fixed for 10 min in 4% neutral buffered formaldehyde (nbf), followed by 2x washes in PBS. Triton X-100 (0.1%) in PBS was added to the cells for 5 min to permeabilise the cells, after which the cells were washed 2x in PBS. The cells were then blocked for 1 hour in blocking solution [10% FCS + 5% BSA] at room temperature, followed by the addition of primary antibody diluted in blocking solution and incubation for 1 hour at 37°C. The coverslips were then washed 4x for 3 min/wash and blocked with blocking solution for a further 5 min before the addition of secondary antibody diluted in blocking buffer and 1 hour incubation at 37°C. The coverslips were then washed 4x for 3 min/wash, followed by nuclear staining using Hoechst for 20 min and 3x washes in PBS. The coverslips were left in PBS at 4°C until imaging.

Table 2. List of Antibodies

Antibody:	Catalogue number:	Dilution:
Anti-LAMP1 antibody [H4A3]	ab25630	1:50
Anti-LAMP2 antibody [H4B4]	ab25631	1:50
Goat anti-Mouse IgG (H+L) Highly Cross-Adsorbed Secondary Antibody, Alexa Fluor 488	A-11029	1:500
Hoechst 33342	R37605	4drops/mL

4.5.2.2 Image acquisition

Fixed and stained cultures were imaged on a Zeiss LSM 710 confocal microscope using a 63x Plan-Apochromat 1.4 NA phase contrast oil-immersion objective using line-by-line multitrack laser switching with 3.15 µs pixel dwell time, 8 averages per line, 405 nm excitation with 410-470 nm bandpass for Hoechst, 488 nm excitation with 505-540 nm bandpass for LAMP-1 & LAMP-2, 633 nm laser and collection of 633 nm reflected light for MBA-AuNP (bandpass 631-636 nm), and collection of 488nm transmitted light for Phase Contrast.

Fields were acquired at 2x optical zoom and 512 x 512 pixels with a pixel resolution of 130 nm/pixel. Confocal z-stacks were acquired using a pinhole size of 1 airy unit at 525 nm and z-step size of 0.2 µm. Number of z-slices per field varied with each acquisition and were set such that the confocal stack began and ended outside of the cellular volume, ensuring that entire cell volumes were captured.

Unless otherwise stated, at least 12 fields of each condition were acquired over three technical replicates.

4.5.2.3 Image processing, object detection, and analysis

Raw .czi confocal stacks were imported into Volocity 6.2 where object detection was conducted on each slice of each z-stack to detect 3-dimensional objects as follows:

LAMP1: Pixels with an intensity ≥ 2000 grey levels and larger than 0.15 μm^2 in area in the LAMP IF channel were labelled as LAMP-objects

LAMP2: Pixels with an intensity ≥ 700 grey levels and larger than 0.15 μm^2 in area in the LAMP IF channel were labelled as LAMP-objects

AuNP: Pixels with an intensity ≥ 3000 grey levels and larger than 0.02 μm^2 in area in the reflection channel were labelled as AuNP-objects. These objects were subject to 2 rounds of dilation followed by one round of touching-object separation with a size guide of 0.05.

Quantification of objects detected was achieved by exporting values from Volocity and graphing them in OriginLab software. Statistical tests were conducted in GraphPad Prism.

4.5.3 Cell proliferation assay (Hoechst)

4.5.3.1 Experimental setup

RC9 hESC cells (2.5 x 10^3 cells/well) were seeded as single cells with ROCKi into 96-well plates and grown for 2 days with mTESR1 medium change every day (Figure 8). On day 2 post-passage, the cell culture medium was changed and 2.5 x 10^{13} MBA-AuNP or sterile H_2O control was added to corresponding wells. On day 3 BafA1 (2nM, 20nM or 200nM) was added to corresponding wells. Medium was changed every day supplemented with corresponding BafA1 concentration. For MBA-AuNP treated cells MBA-AuNP or H_2O control was added to the medium only on Day 2. The cells were fixed with 4% PFA in PBS and then stained with Hoechst dye to label nuclei 1h after BafA1 addition (Timepoint 1), 24h after (Timepoint 2), 48h after (Timepoint 3) and 72h after (Timepoint 4). These timepoints corresponds to 24h, 48h, 72h and 96h MBA-AuNP incubation respectively. Cells were imaged immediately after fixation and staining.

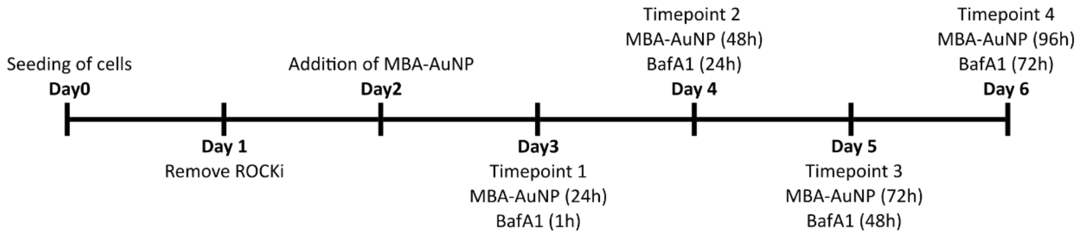

Figure 8. Cell proliferation assay, experimental timeline
Cells were seeded on Day 0, followed by removal of ROCKi on Day 1. If MBA-AuNPs were added this was done on Day 2. BafA1 was added on Day 3 to corresponding wells and was supplemented into every medium feed after this. Medium was changed every day.

4.5.3.2 Image acquisition

Whole wells of fixed cells were imaged on a Zeiss Observer 7 microscope using an EC Plan-Neofluar 10x/0.30 Ph1 in Phase Contrast and a DAPI filter set for fluorescence. Zen 2.6 software was set to acquire overlapping tiled fields with 100% coverage of each well and using software autofocus in the Hoechst channel. Whole-well images were then imported into Volocity 6.2 where a circular ROI was used to crop each image to each well’s surface area. Cropped images were subject to nuclear detection using a custom nuclear detection algorithm on the Hoechst channel with the following parameters: the detection pipeline was configured to detect objects ≥ 373 grey levels and 5 μm^2 with a rolling contrast window of 10 µm diameter before an average nuclear size of 50 um^2 was used to separate touching objects. Any detected objects smaller than 20 μm^2 were considered cell debris and were discarded. An example result of the nuclear detection pipeline can be seen in Figure 9. Numbers of nuclei per well were automatically extracted and exported in .csv format. Conditions were repeated with 3 wells each for each of three technical replicates.

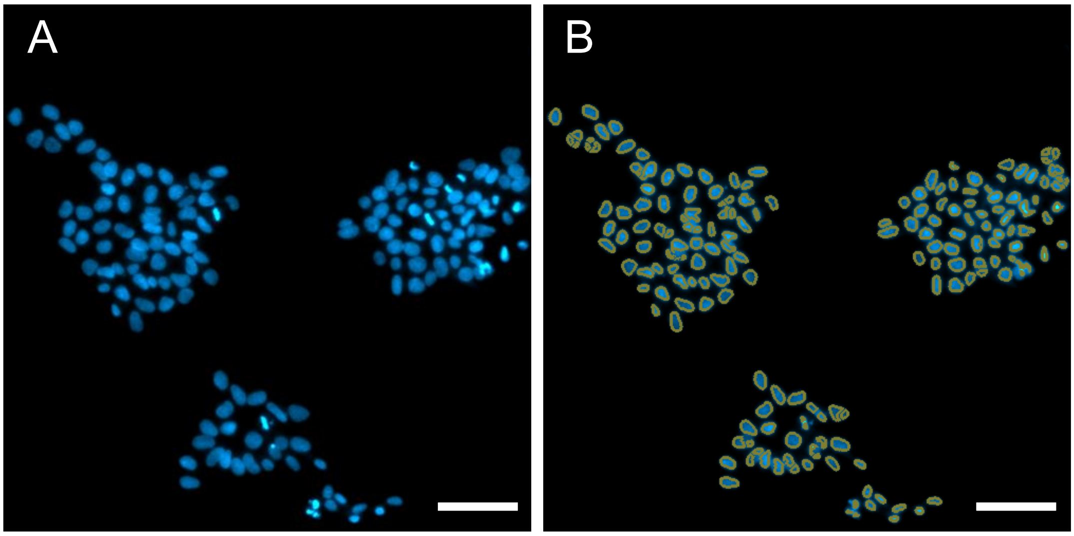

Figure 9. Hoechst object detection
Object detection of cells stained with Hoechst, for nuclear detection, using Volocity software. Images show a representative area of stained nuclei (A) and the corresponding detected objects (B). Each identified object is surrounded by a yellow border. Scalebar = 100 µm.

4.5.4 Autofluorescence of SVZ cells

4.5.4.1 Experimental setup

Six primary SVZ cell cultures (2x WT, 2x HET, and 2x KO) were seeded onto gelatin coated 22 x 22 mm glass coverslips (0.17 mm thickness) in 6-well plates at a density of approximately $5x10^4$ cells/well. The cells were grown for 2 days, after which they were fixed in 4% NBF in PBS and mounted onto microscope slides using PermaFluor Hard-set mountant (#TA-030-FM).

4.5.4.2 Imaging

The mounted coverslips were imaged on an Olympus BX63 microscope attached to a Yokogawa CSU-W1 spinning disk confocal unit equipped with two Hamamatsu C9100-14 ImagEM emCCD cameras and controlled by Slidebook 6.0 software. Filter sets for DAPI, FITC, and TRITC were used to acquire three discrete wavelength ranges of autofluorescence with excitation from a CoolLED PE4000 LED unit (385 nm LED, 490nm LED, and 525 nm LED) and the CSU-W1 set to widefield mode for maximum light collection. To acquire such low levels of light that emit from autofluorescent sources the electron multiplication gain of the emCCD cameras were set to 200 and each acquisition was averaged on-chip 8 times. Exposure times were as follows: 150ms seconds for blue channel, 250ms seconds for green channel, 400ms seconds for red channel.

4.5.4.3 Image processing and object detection

Images were exported in OMETIFF format and imported into Volocity 6.2 for object detection and analysis as follows:

First, a cell mask was defined to remove any non-cellular fluorescent material by thresholding the green channel with pixels ≥ 3800 grey levels and a minimum object size of 0.42 μm^2. Detected objects smaller than 120 μm^2 were excluded and then the remaining objects were dilated 4 times.

Blue autofluorescence objects were defined as pixels in the blue channel ≥ 1.5 standard deviations more intense than the blue channel image mean, with an object size ≥ 0.2 μm^2, and contained within the cell mask.

Green autofluorescence objects were defined as pixels in the green channel ≥ 1.3 standard deviations more intense than the green channel image mean, with an object size ≥ 0.2 μm^2, and contained within the cell mask.

Red autofluorescence objects were defined as pixels in the red channel ≥ 1.7 standard deviations more intense than the red channel image mean, with an object size ≥ 0.2 μm^2, and contained within the cell mask.

Examples of object detection for all three channels can be seen in Figure 10. Mean fluorescent intensity measurements for all objects in all channels were then exported to Excel, averaged across all channels, and all data were graphed in OriginLab software.

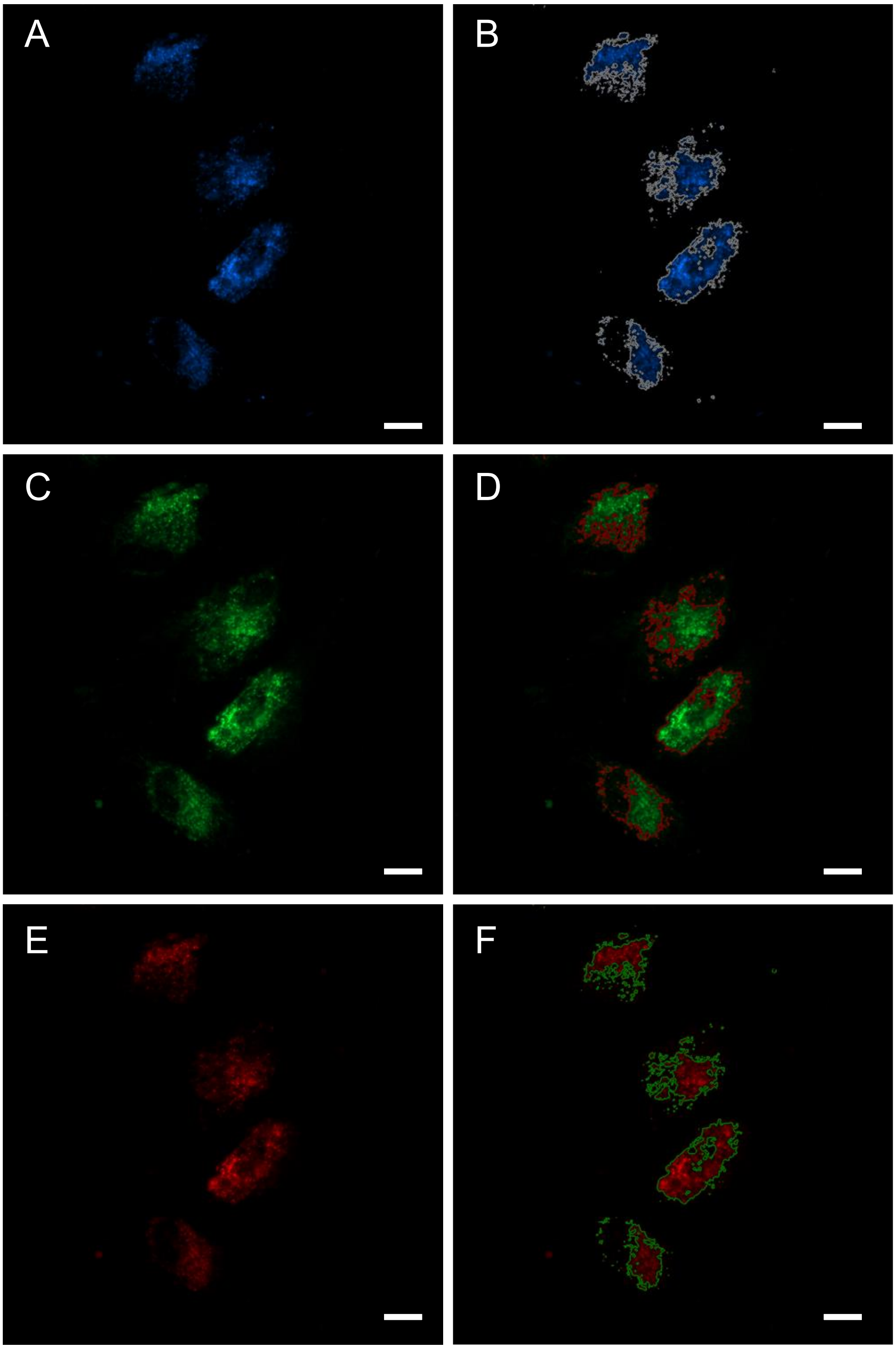

Figure 10. Object detection of autofluorescence in primary sheep SVZ cells
Autofluorescence of primary sheep SVZ cells in the blue (A, B), green (C, D), and red (E, F) channels. Pseudocoloured images are shown on the left and the same images are shown on the right overlaid with object detection outlines. Scalebars are 20 µm.

4.6 PPT1 assay

Primary sheep SVZ cells (KO, HET and WT) were grown in T75 flasks until confluent. Cells were rinsed 2x in PBS (-/-) and incubated with CTS™ TrypLE™ Select enzyme for around 7 min at 37°C. PBS was then added to the flask and the cells were pipetted until a single cell suspension was obtained. The cells were then counted and spun down at 200 x *g* for 2 min. The supernatant was removed, and the cells were resuspended in sterile water at a final concentration of 1 x 10^7 cells/mL and kept on ice until sonication. Just before sonication the cells were mixed by pipetting followed by a brief vortex and transferred to a Bioruptor Plus Sonicator. The cells were sonicated on high power for 10 cycles (1 cycle: 30s ON/ 30s OFF) at 4°C. Halfway through the cycles the cells were briefly mixed by vortex. After sonication the cells were centrifuged at 17000 x *g* for 20 min at 4°C. The supernatant was collected and transferred to a fresh Eppendorf tube and transferred to a -80°C freezer for storage until the assay was performed.

The protein concentration for each sample was determined using Pierce™ BCA Protein Assay Kit according to the manufacturer's 96-well microplate procedure. Each sample was diluted 1/5 before the assay.

The samples were transported on dry ice to Samantha Eaton, Roslin Institute, who performed the PPT1 assay according to published protocol [77].

5 Characterisation of MBA-AuNPs as a pH sensor

As outlined in Chapter 2, Raman spectroscopy has shown potential for the investigation of intracellular signals and functions. However, as also detailed in the main introduction, Raman scattering is a weak phenomenon. Therefore, attempts have been made to increase the signal by utilising metal nanoparticles through a technique called Surface Enhanced Raman Spectroscopy (SERS).

SERS has been utilised before to measure pH within cells. One of the most frequently used pH-sensitive molecules for this purpose is 4-mercaptobenzoic acid (MBA). MBA can be attached to the gold nanoparticle (AuNP) surface via covalent gold-thiol bonds [43]. MBA has a SERS spectrum which is characterised by two main reported pH insensitive peaks, at 1080 cm^{-1} and 1590 cm^{-1}, and two main reported pH sensitive peaks, at 1420 cm^{-1} and 1700 cm^{-1} (Figure 11) [8,42,43]. The experiments in this study will only involve the analysis of the two main pH sensitive peaks and the pH insensitive peak at 1590 cm^{-1}.

This chapter will outline the process of making MBA-AuNPs and the assessment of the functionality and analysis of the particles. The analysis of resultant SERS spectra and pH calibration curves will also be discussed. In addition, the reversibility and cytotoxicity of the sensor is evaluated.

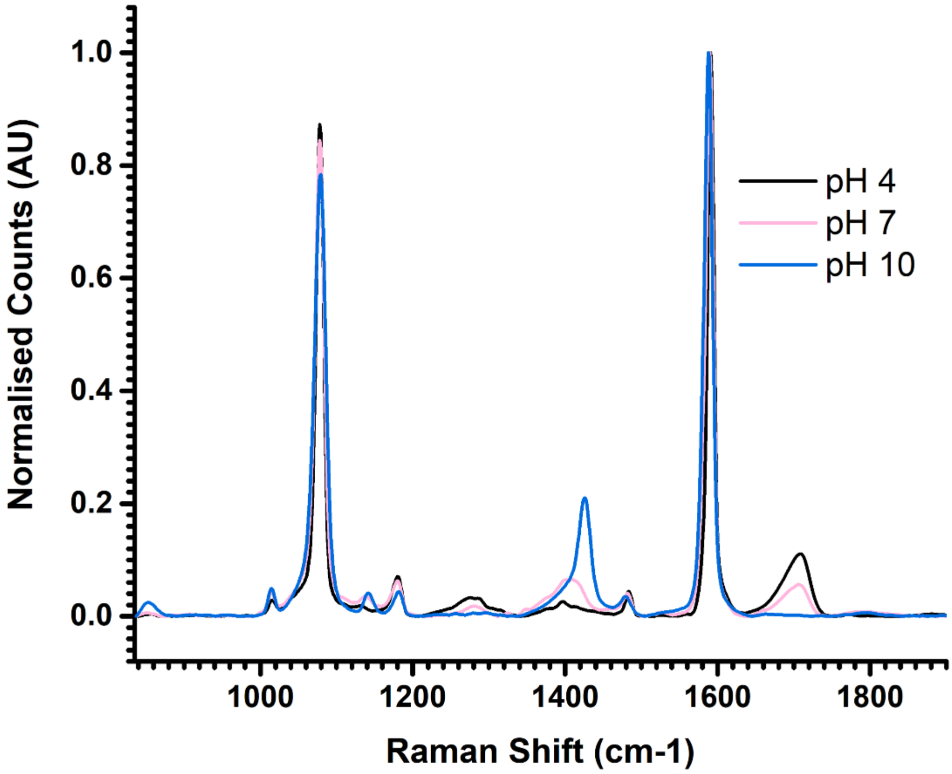

Figure 11. Raman spectrum of 4-Mercaptobenzoic acid

Image shows smoothened, baseline-corrected, and normalised (to the 1590 cm^{-1} peak) spectra of MBA at pH 4, 7 and 10 between 835 cm^{-1} and 1900 cm^{-1}. The spectrum displays two pH-insensitive peaks at approximately 1080 cm^{-1} and 1590 cm^{-1}. The two main pH-sensitive peaks are found at approximately 1420 cm^{-1} and 1700 cm^{-1}.

5.1 Functionalisation of gold nanoparticles with 4-Mercaptobenzoic acid

To perform intracellular pH measurements, 100 nm citrate-capped gold nanoparticles (AuNPs) were functionalised with mercaptobenzoic acid (MBA), as described in section 4.2.1, to form Surface Enhanced Raman Spectroscopy (SERS) nano-sensors. To confirm successful functionalisation, UV-vis spectra were recorded at the end of each functionalisation for every batch. Figure 12 shows the UV-vis spectra of stock AuNPs, unwashed MBA-AuNPs, and MBA-AuNPs following one and two washes. As can be seen, the excess MBA seen in the unwashed MBA-AuNP (orange line, peaks at between 200-250 nm) is successfully removed after two washes in water (Figure 12, A). Furthermore, the integrity of the AuNP peak at 570 nm is maintained before and after functionalisation and washes indicating no aggregation, which would otherwise result in a significant redshift, broadening and intensity decrease of the peak. Another feature that can be observed is a small redshift of the AuNP peak from 570 nm to 573 nm (Figure 12, B), which is an indication of successful binding of the MBA to the gold surface.

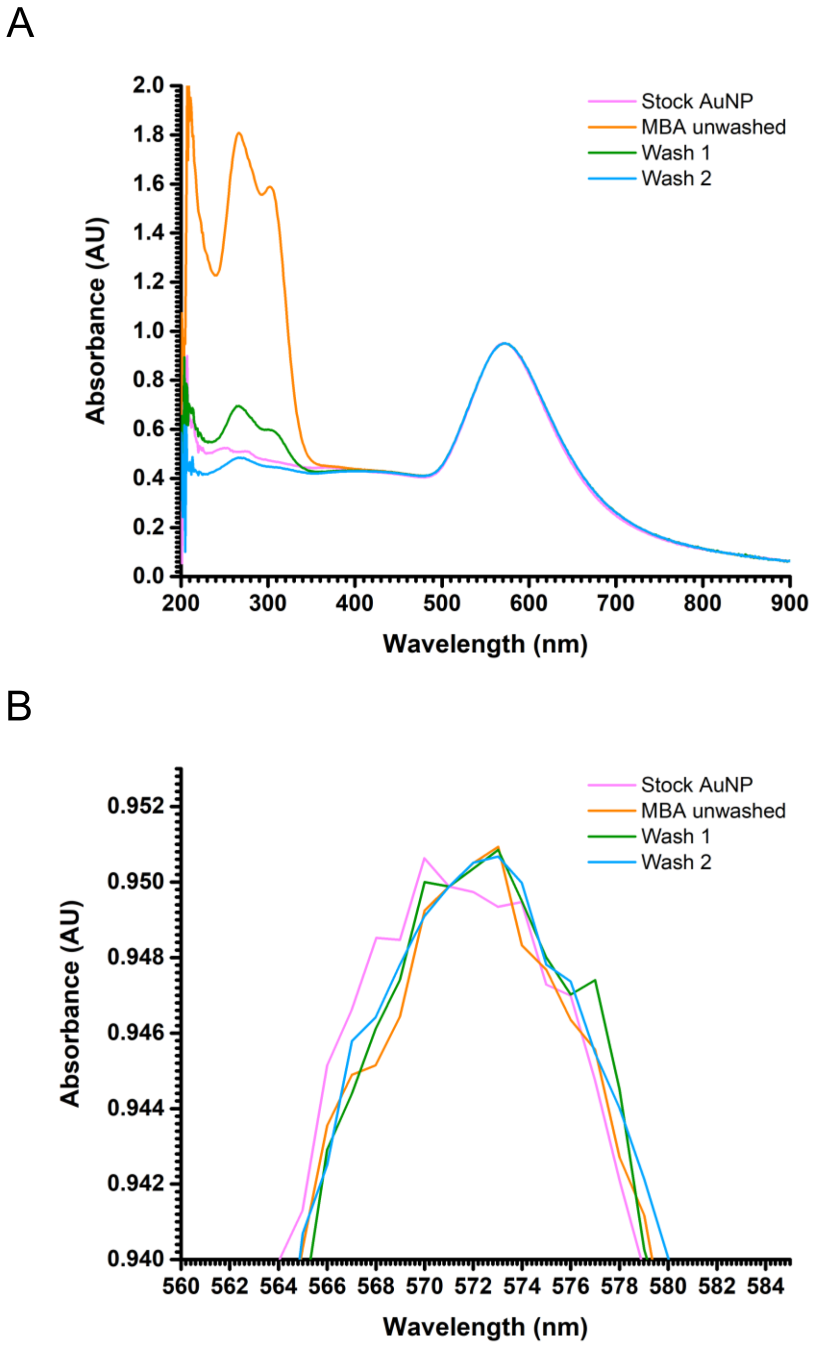

Figure 12. UV-visible spectra of AuNPs, normalised to the 570 nm peak.
(A) Absorbance spectra from wavelength range 200-900 nm of Stock AuNP (pink), MBA-coated unwashed AuNP (orange), and MBA-coated particles washed 1 time (green) and 2 times (blue). Absorbance peaks at 200-300 nm after MBA coating return to stock-levels after wash steps. (B) Subset wavelength range of plots in (A) from wavelengths 560-584 nm showing 3 nm shift of the peak from 570 nm to 573 nm between Stock AuNP vs MBA-coated, 1x washed, and 2x washed.

5.2 MBA-AuNP calibration curve and analysis

5.2.1 Spectral acquisition and characteristics

To be able to determine the pH using the MBA-AuNP nano-sensors, a calibration curve measuring the response of MBA-AuNP to pH had to first be made. To do this MBA-AuNP droplets were dried onto CaF_2 microscope slides and alternating measurements of standard pH solutions between pH4 and pH10 were taken using SERS. Point spectra Raman maps were taken along the outer edge of the dried MBA-AuNP droplet, where the nanoparticles tended to accumulate due to surface tension (Figure 13). Averaged spectra for all collected pH values between 1300 cm^{-1} and 1800 cm^{-1} Raman shifts can be seen in Figure 14. The peak at approximately 1420 cm^{-1} (Figure 14, B) represents COO^- symmetric stretching, and the counts, or intensity of the peak, is related to the deprotonated state of MBA. As can be seen, as pH increases to more alkaline values the counts of the peak increases correspondingly. The peak at approximately 1700 cm^{-1} (Figure 14, C) is instead related to the C = O stretching of the COOH group, which happens when MBA is in its protonated form. Conversely to the peak at 1420 cm^{-1}, the count of the 1700 cm^{-1} peak increases as pH decreases and becomes more acidic. Most literature have utilised the 1420 cm^{-1} peak for pH measurements, but in theory either can be used because as one increases the other decreases and vice versa. To decide which peak would be the most appropriate for this study, both peaks were characterised and used to create calibration curves in sections 5.2.2.1 and 5.2.2.2.

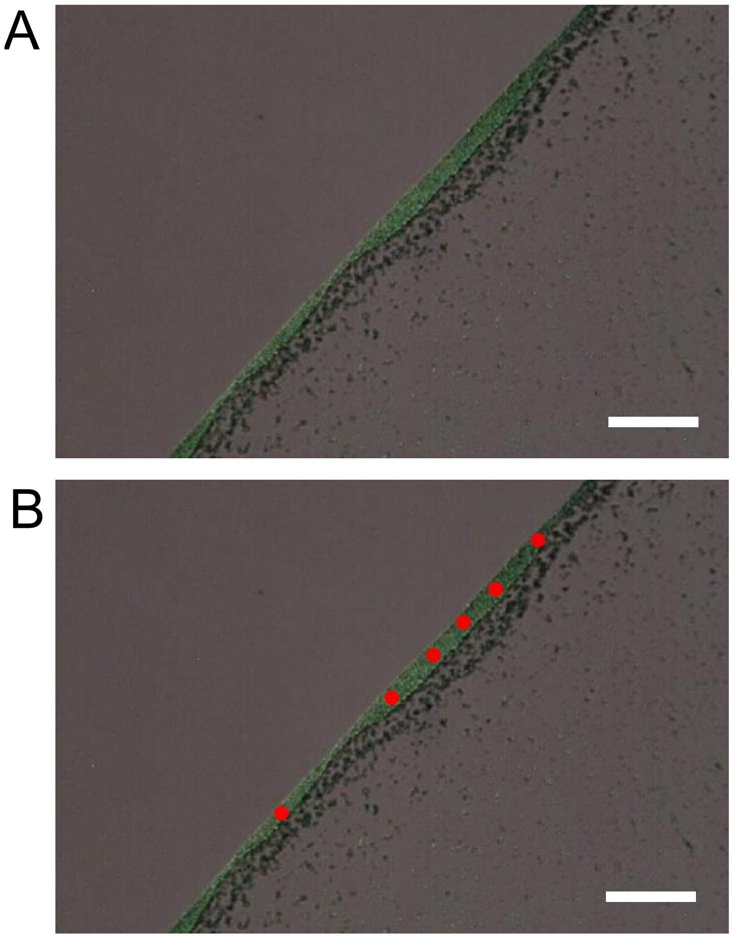

Figure 13. Dried AuNPs.
Representative image of dried AuNPs (A) and areas where point spectra were acquired to create a map (B). Scalebar = 20µm.

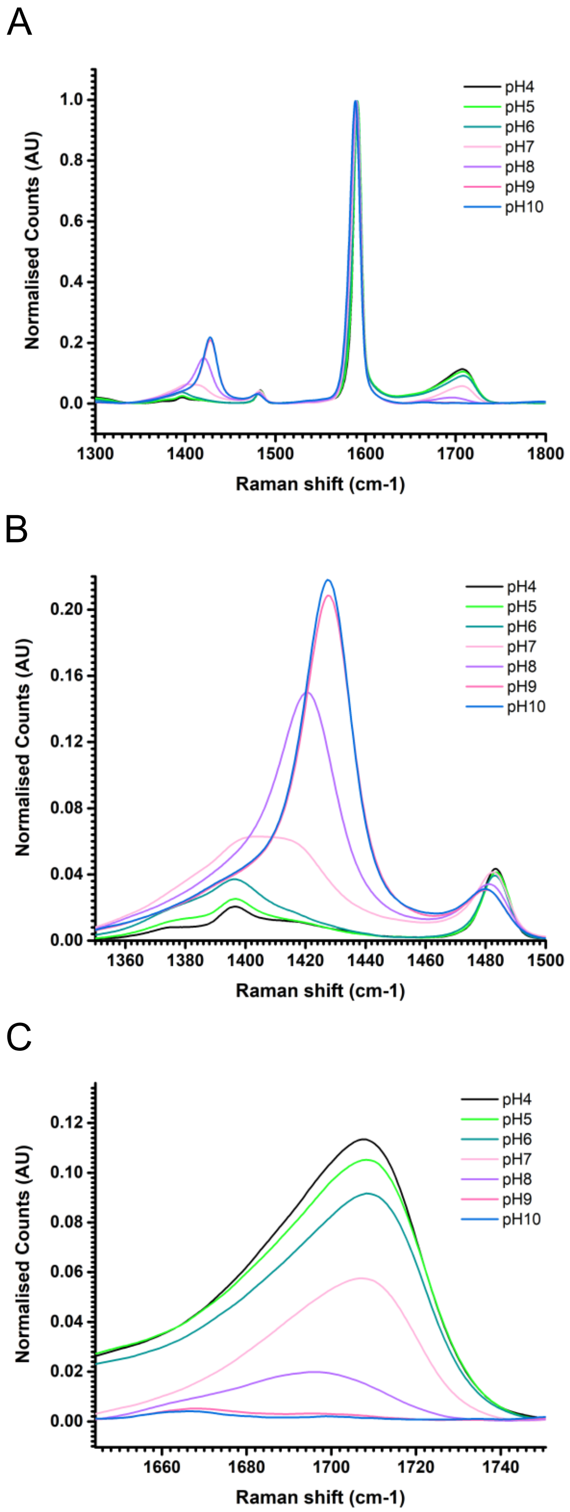

Figure 14. Raman spectra of MBA-AuNP at pH4-pH10.

Raman spectra of standard pH buffers (pH4-pH10) using dried MBA-AuNP recorded at 1300-1800cm^{-1} (A). Coloured plots represent pooled averaged spectra from all measurements of each pH standard (pH4, n=35; pH5, n=36; pH6, n=34; pH7, n=36; pH8, n=34; pH9, n=33; pH10, n=35). Spectra are normalised to non-pH-responsive reference peak at 1590 cm^{-1}. The alkaline-sensitive peak at 1420 cm^{-1} is expanded in (B), while acid-sensitive peak at 1700 cm^{-1} is expanded in (C).

5.2.2 AUC vs Peak height

In addition to the characterisation of the two pH sensitive peaks, there are discrepancies in some publications and labs regarding how the peaks are measured [8,57,78]. Some studies use area under the curve (AUC) while others use peak height to generate their calibration curves. The Raman spectra from MBA includes two pH unresponsive peaks, at 1075 cm^{-1} and 1590 cm^{-1}, which can be used as reference peaks. The ratio between the pH responsive 1420-peak and the 1700-peak has also been used to generate a calibration curve [79]. In this study, an AUC and peak method for the 1420 peak and the 1700 peak normalised to the 1590 reference peak were compared. Firstly, each acquired spectra was manually inspected and spectra with low signal to noise ratio or unusual peaks were excluded to assure the accuracy and quality of the resulting calibration curve (Figure 15). Only 11 out of 254 spectra that were acquired were removed, with most of them only displaying minor differences to the reference spectra, apart from the single spectral curve removed for pH 4 which displayed a very low signal to noise ratio.

All data were smoothened using 13 points, baselined, cropped, and normalised to 1 in Wire 4.4.1 software. Using a Mathematica script produced by Dr Daniel Y.H. Soong (CRH, University of Edinburgh) the AUC and maximum peak heights of the pH sensitive peaks were extracted and plotted in OriginLab. Boltzmann curves were fitted for each dataset generating the calibration curves in the following sections, 5.2.2.1 and 5.2.2.2.

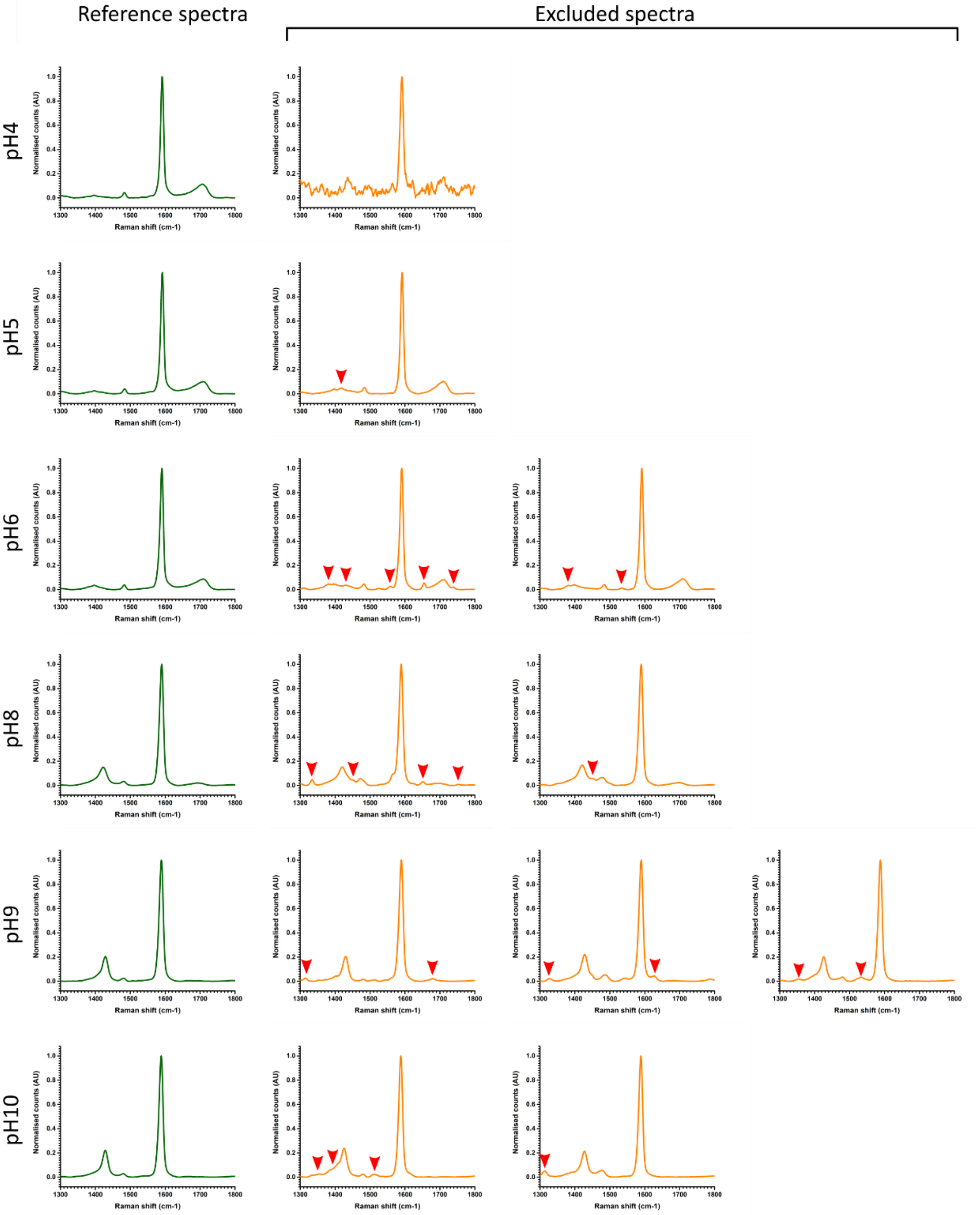

Figure 15. Spectra excluded from calibration curves.

Figure show all Raman spectra that were excluded (orange) from the calibration curve analysis compared to reference spectra (green). Spectra was excluded based on criteria such as low signal to noise ratio, odd extra peaks, or other irregularities (red arrows). In total 11 spectra out of 254 total spectra were excluded.

5.2.2.1 Calibration curves based on AUC and peak height: 1420-peak

The resulting calibration curves based on either the AUC or peak height methods for the 1420-peak are displayed in Figure 16. Datapoints were collected for buffers with a pH value of a range from pH 4 - pH 10, plotted, and had a Boltzmann curve fitted. An adjusted R^2 value of 0.989 and 0.995 was obtained for Figure 16 A and B respectively, indicating a good fit, and the 95% confidence interval lay close to the fitted Boltzmann curve indicating good accuracy of calibration curve. Interestingly, the pK_a obtained for the 1420-peak calibration curves (Figure 16) are quite different between the AUC method ($pK_a = 7.149$) and the maximum peak method ($pK_a = 7.710$). There also appear to be more outliers for the AUC method compared to the peak method. All this highlights that the method used to generate the calibration curve needs to be carefully considered depending on which pH range needs to be investigated if the 1420cm^{-1} peak is to be used for analysis.

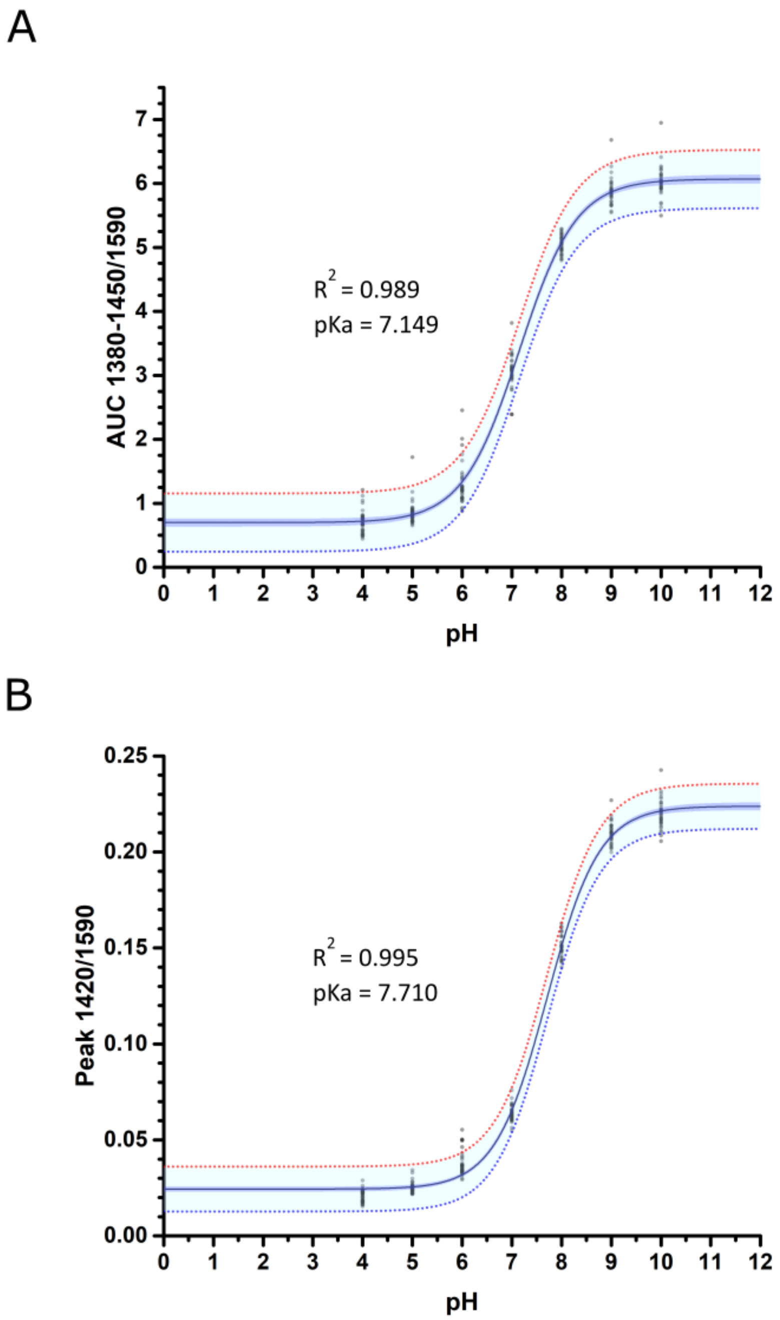

Figure 16. Calibration curve AUC and peak: 1420 cm^{-1} region.

(A) Calibration curve based on the area-under-curve for the normalised 1420 cm^{-1} peak (integrated from 1380-1450 cm^{-1}) for each pH standard buffer.

(B) Calibration curve based on the maximum value recorded for the acidic peak (~1420 cm^{-1}) for each pH standard buffer. Spots represent individual measurements at each pH standard. Central plot line represents the sigmoid fit of the data overlaid with 95% confidence interval (dark blue bands). Red and blue dotted lines and light blue area between represent 95% prediction interval where 95% of future data would be expected to lie.

5.2.2.2 Calibration curves based on AUC and peak height: 1700-peak

Figure 17 shows the resulting calibration curves based on the AUC and peak height methods for the 1700-peak. Datapoints were collected for buffers with a pH value of a range from pH 4 - pH 10, plotted and had a Boltzmann curve fitted. An adjusted R^2 value of 0.992 and 0.993 was obtained for the AUC and peak height method, respectively, indicating a good fit for both methods. The results were also very similar when looking at the pK_a values, which was 6.959 for the AUC method and 7.003 for the peak height method. Since the pK_a values are very close between the AUC and maximum peak method both methods were deemed equally acceptable; however, because the AUC method displayed more outliers and larger range of values, the maximum peak height method was preferred.

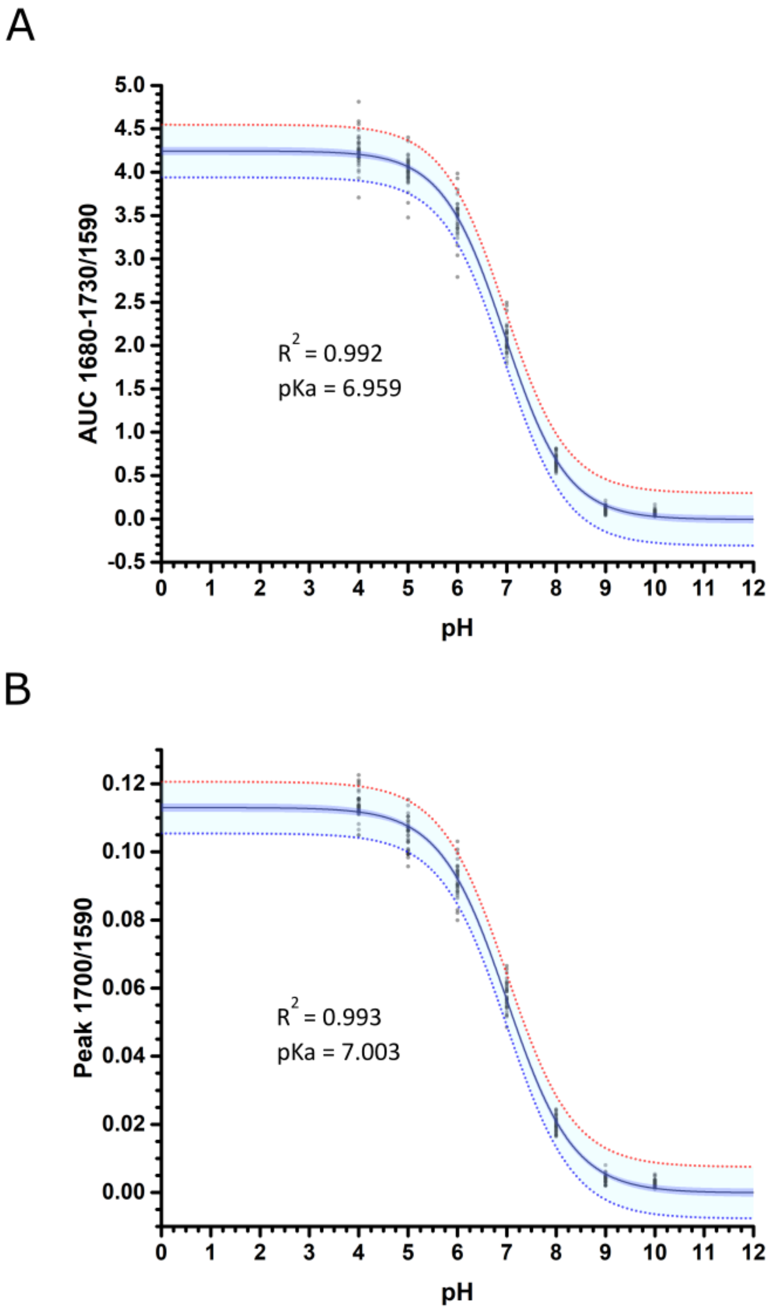

Figure 17. Calibration curve AUC and peak: 1700 cm^{-1} region.

(A) Calibration curve based on the area-under-curve for the normalised 1700 cm^{-1} peak (integrated from 1680-1730 cm^{-1}) for each pH standard buffer.

(B) Calibration curve based on the maximum value recorded for the acidic peak (~1700 cm^{-1}) for each pH standard buffer. Spots represent individual measurements at each pH standard. Central plot line represents the sigmoid fit of the data overlaid with 95% confidence interval (dark blue bands). Red and blue dotted lines and light blue area between represent 95% prediction interval where 95% of future data would be expected to lie.

5.2.3 Assigning pH values from spectra

To visualise the accuracy of using each method for pH determination the raw calibration data were assigned pH values based on the calibration curves using the ‘Find X from Y’ function within OriginLab. Values that were outside of the calibration range were excluded, and the assigned pH values and the percentage of data that were able to be converted were plotted against each other (Figure 18, Figure 19). For all methods 100% designation was possible for pH values between 6-8. When looking at the more extreme ends of the pH range, however, the calibration curves based on the 1420-peak resulted in fewer designations compared to the 1700-peak. It is notable that the assigned pH values at the range extremities is highly variable, whereas pH values that are closer to the pK_a of the curves cluster more closely. When comparing AUC vs peak height methods, it can be seen for the 1420-peak that less than 70% of pH 10 measurements were assignable using AUC compared to greater than 75% using peak height while approximately 40% of pH 4 measurements were assigned using AUC vs approximately 10% for peak height. When looking at the 1700-peak, however, almost all spectra were assignable except at pH 4 where approximately 40% were assigned for each method, and pH 5 where approximately 95% were assigned.

Considering the observations in the previous sections combined with the fact that the AUC method resulted in more outliers, the peak height method using the 1700-peak was chosen for analysis of all collected spectra presented from here on.

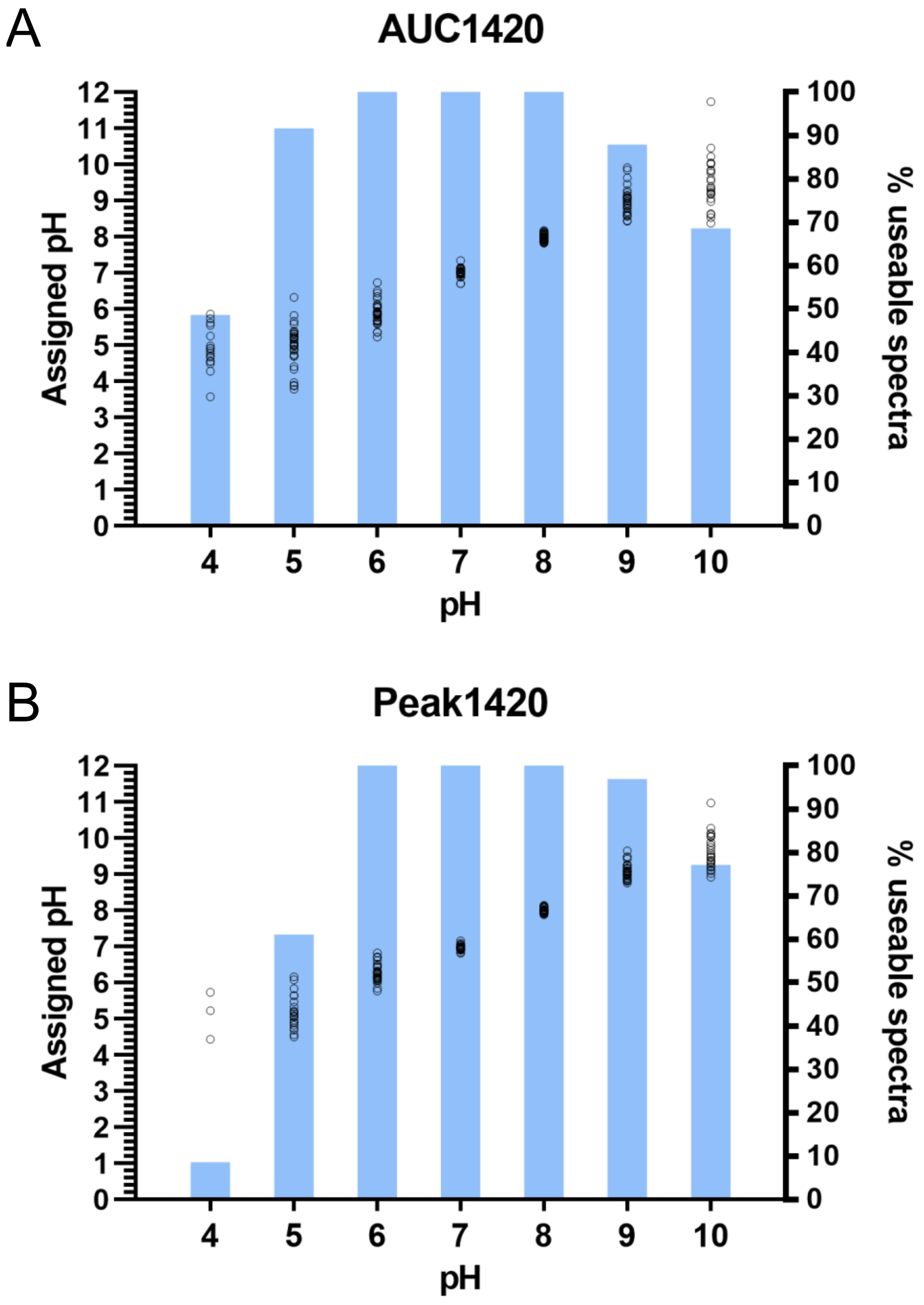

Figure 18. Assigned pH and % useable spectra of the 1420-peak.

Comparison of assigned pH and % useable spectra between the area under the curve method (A) and peak method (B) of the 1420-peak. Dots represent the assigned pH based on the calibration curve in Figure 16. Bars show the percentage of spectra that was able to be converted using the calibration curve. Values unable to be converted laid outside of the calibration curve range.

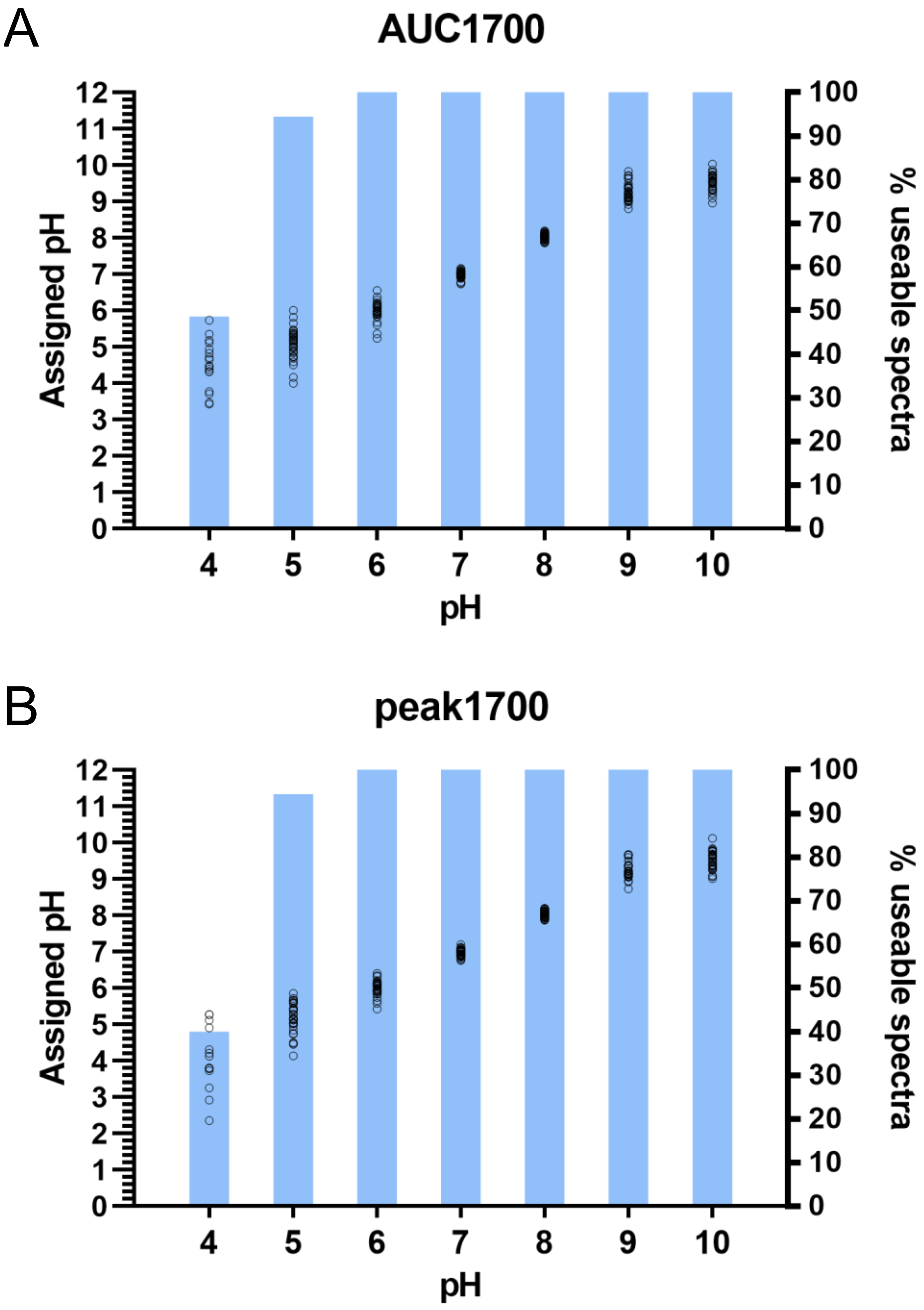

Figure 19. Assigned pH and % useable spectra of the 1700-peak.

Comparison of assigned pH and % useable spectra between the area under the curve method (A) and peak method (B) of the 1700-peak. Dots represent the assigned pH based on the calibration curve in Figure 16. Bars show the percentage of spectra that was able to be converted using the calibration curve. Values unable to be converted laid outside of the calibration curve range.

5.3 MBA-AuNPs efficiently respond to pH changes reversibly

In biological situations pH will fluctuate in response to intracellular and extracellular signals. In addition, and to maintain normal cell function, different organelles and cellular compartments have distinct pH microenvironments. To detect these fluctuations and differences in pH the capability of the MBA-AuNP sensor to respond to pH fluctuations in a reversible manner was therefore assessed. Three different batches of particles were dried down onto a CaF_2 slide and a droplet of either pH 4 or pH 10 was added and spectra were measured in an alternating fashion with water washes between each swap (Figure 20). All attempts were made to measure the same locations in all alternating cycles, but occasionally focus was lost during the swap, and this was not always possible. The time between each wash, which caused a conversion between the protonated and de-protonated forms of MBA (Figure 20, A), was only a few minutes at most. As can be seen (Figure 20, B) the sensor efficiently responded to the pH changes in a reversible manner, even after six alternating cycles. In addition, all batches of MBA-AuNP responded in the same way, showing robustness and reproducibility of the sensor itself.

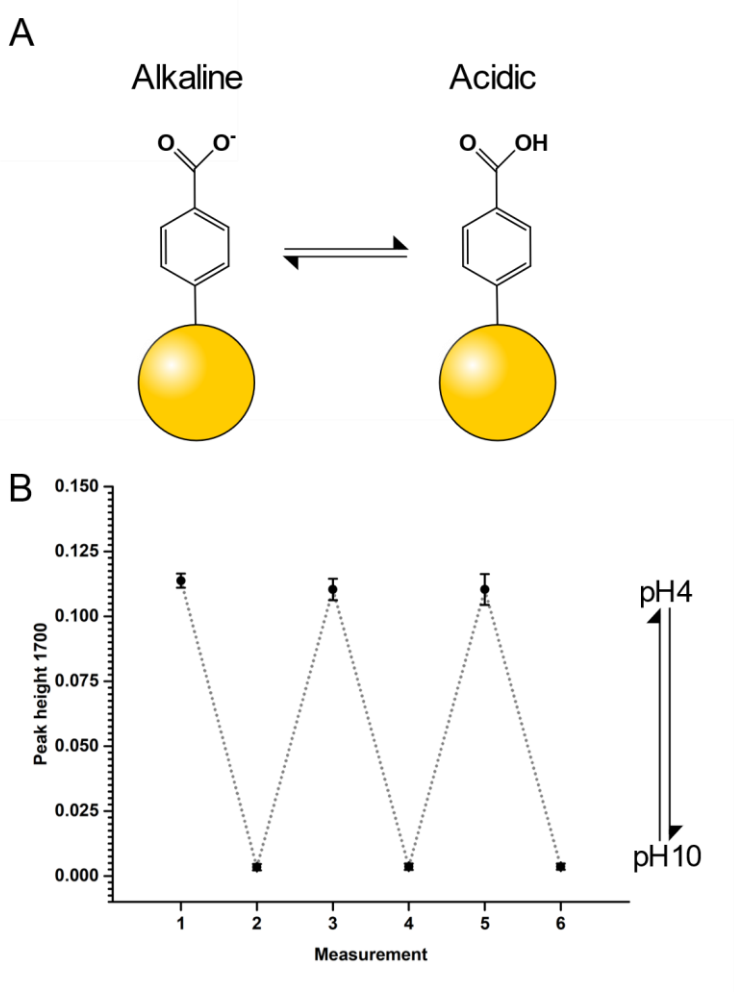

Figure 20. Reversibility of MBA-AuNP pH sensors.
(A) Schematic illustration of the molecular change in MBA in response to pH. (B) Shows the ability of the MBA-AuNP sensor to respond to pH changes. The pH buffers were alternated between pH4 and pH10. Triplicate point maps were collected for each pH (18 spectra total/ timepoint). Higher peak heights indicate more acidic pH values. Error bars are shown as standard deviation.

5.4 MBA-AuNPs do not cause reduced cell viability in RC9 cells

Before introducing the MBA-AuNP into cells for SERS measurements, it was important to confirm that they do not induce a toxic response. To do this a PrestoBlue cell viability assay was performed. PrestoBlue is a reazurin-based reagent which allows the assessment of changes in the metabolism or cellular reducing environment within cells, which are indicators of cell viability or death. Reazurin is a non-fluorescent blue non-toxic cell-permeable compound which, upon entry into live cells, is continuously reduced to resorufin – a red and highly fluorescent compound. This change from non-fluorescence to fluorescence can be detected using an absorbance-based plate reader with an excitation filter of 520 nm and an emission filter of 580-640nm.

The assay was performed on RC9 hESC as described in section 4.4. All samples were normalised to the background levels of a well containing PrestoBlue without cells, and compared to water only control or TritonX 0.03%, which served as a positive control for loss of cell viability. No significant difference in cell viability was observed between the water control and any of the AuNP or MBA alone concentrations tested, whereas TritonX-100 reduced the viability to near background levels (Figure 21). All concentrations of the AuNPs in Molar units and their corresponding concentrations in particles/mL can be found in Table 3. Since no loss of viability was observed, an MBA-AuNP concentration of 2.5×10^{13} was chosen for subsequent Raman tests, as higher number of particles would result in an increase of the Raman signal and uptake of particles into the cells.

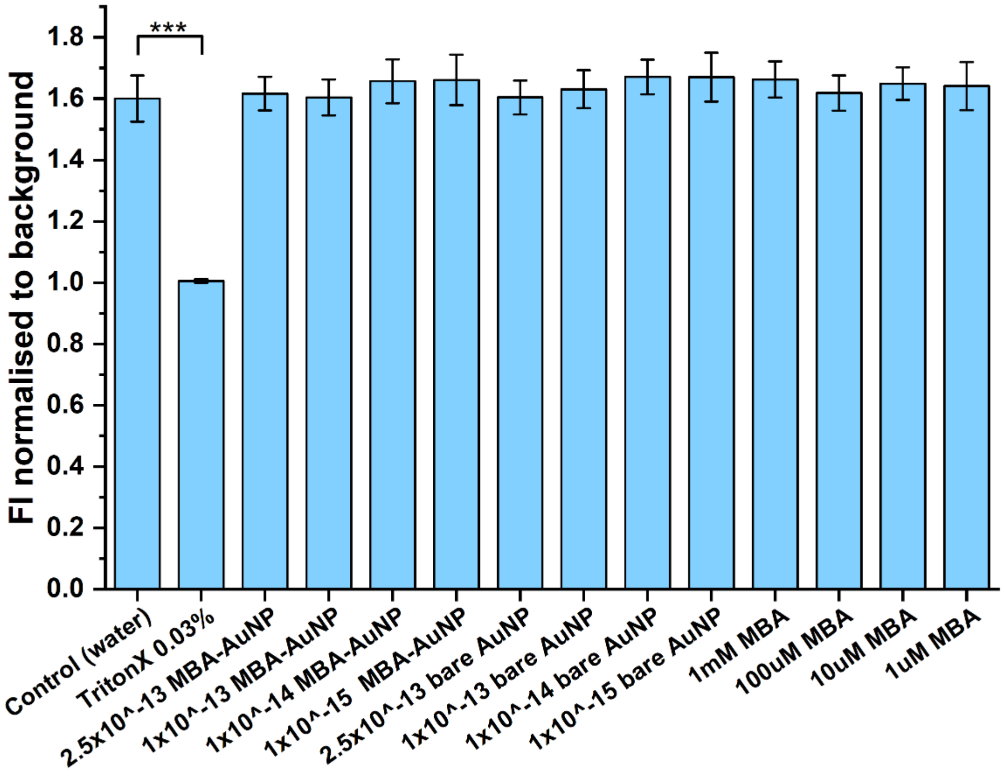

Figure 21. PrestoBlue Cytotoxicity assay of 100nm AuNPs in RC9 hESC.

PrestoBlue cytotoxicity assay carried out in RC9 cells. Cells were cultured in 96 well plates for 24 hours after sample addition before measurements were taken. Treatments were carried out in triplicates on three separate days. All values were normalised to PrestoBlue background levels. MBA-coated AuNP were compared with tritox-X100 treatment, uncoated AuNP (bare), and MBA alone. P-values: ns > 0.05, * < 0.05, ** < 0.01, *** < 0.001, **** < 0.0001, one-way ANOVA with Fischer's LSD test.

Concentration (M)	Concentration (particles/mL)
2.5 x 10^{13} M	1.5 x 10^{8} particles/mL
1 x 10^{13} M	6 x 10^{7} particles/mL
1 x 10^{14} M	6 x 10^{6} particles/mL
1 x 10^{15} M	6 x 10^{5} particles/mL

Table 3. Concentrations of AuNPs tested.

List of concentrations tested in Figure 21, shown in Molar concentration and their equivalents measured in particles/mL.

5.5 Chapter summary

In this chapter we have demonstrated that 100nm AuNP can be successfully conjugated to MBA to create stable SERS active pH sensors. Analysis of the resulting Raman spectra from MBA varies between publications. Using two methods to analyse and obtain calibration curves from either the 1420-peak or 1700-peak, an AUC and peak height method, we determined that the 1700-peak and the peak height method was the most reliable. This decision is somewhat supported by the literature which shows that the 1420-peak is prone to be affected by cell membranes whereas the 1700-peak is less so, making it less ideal for pH measurements within cells [43].

Furthermore, the 1420-peak can actually be divided into two peaks, one at around 1380 cm^{-1} and one at around 1410 cm^{-1} [80,81]. The orientation of the MBA molecule on the AuNP surface influences which of these peaks is the most prominent in the Raman spectrum. The orientation of the MBA molecule is influenced by the functionalisation process, such as the concentration of MBA and the pH of the solution used and the roughness of the AuNP surface. [82]. Differences in the intrinsic pK_a of 2-MBA in solution and immobilised ligand on a silver surface have been reported to be as a result of changes in the electron density on the benzoic acid group caused by the thiol-metal bond when the molecule is covalently attached to the metal surface [83]. It is possible that this is also true for 4-MBA covalently attached to a gold surface via a thiol-gold bond. The information above could explain some discrepancies in the literature regarding the pK_a of MBA, which has been reported at a range between 5.3-8.75 [42,43,81,84,85]. This information further supports the use of the 1700-peak in analysis of spectra from within cells, as it is less affected by cellular background signals and may not change as much depending on functionalisation conditions.

We have also shown that the MBA-AuNP used in this study are able to respond to pH changes in a reversible manner. Finally, the effect of the MBA-AuNP on the viability of hESC was assessed using a PrestoBlue cell viability assay. In agreement with previous experiments in the literature [37,81], no negative effect on cell viability were observed. This data supports the use of MBA-AuNP for the measurement of pH within cells.

6 MBA-AuNP as a SERS pH sensor in live cells

6.1 Introduction

In the previous chapter MBA-AuNPs were produced, a calibration curve was generated and a reliable method for analysing Raman spectra to determine pH was evaluated. The best method for analysis was determined to be by using the normalised peak at 1700 cm^{-1} which corresponds to the C = O stretching of the COOH group in MBA. The MBA-AuNPs were also determined to be able to respond to pH changes in a reversible manner. In addition, MBA-AuNP was shown to cause no detectable negative effects to the cell viability of the hESC line RC9.

Next, we wanted to address the introduction of the MBA-AuNP into RC9 cells for pH measurements using SERS. Previous studies have shown that nanoparticles can end up in the cytoplasm of the cells [37] or inside membrane-bound vesicles of the endolysosomal pathway [86–88]. There are many factors that play a role in where the particles end up within cells, including the temperature; size, charge, shape, and surface coating of the nanoparticles [86–89]. Since there are discrepancies of where the particles end up within cells in the literature, it was first important for us to determine where our particles ended up within the cells before drawing any conclusions of pH SERS measurements.

The main aims of the experiments within this chapter were to first explore the uptake of MBA-AuNP within cells and determine where the particles end up. Secondly, we had to optimise the culture of our cells on a suitable substrate in preparation for SERS measurements. Finally, we performed SERS measurements within cells using MBA-AuNP to assess the sensitivity of the sensor in a biological setting.

6.2 MBA-AuNP uptake within stem cells

The uptake mechanism of the MBA-AuNP into stem cells was documented using live-cell timelapse microscopy. As described in section 4.5.1, RC9 hESC were grown on coverslip-bottomed 6-well plates and imaged using a combination of both phase contrast and brightfield microscopy every 10 minutes for 16 hours (Figure 22). Images in Figure 22 show phase contrast images overlaid with minimum intensity projected brightfield images pseudocoloured in yellow. This allows clear visualisation of the yellow MBA-AuNP within the monochrome phase contrast images. The process for generating these images is explained in more detail in section 4.5.1.

Initially, after 1 hour of addition, very few MBA-AuNP are present within the cells and the surrounding matrix (Figure 22). As time passes increasing amounts of MBA-AuNP (yellow specks) appear within the matrix, and clusters of MBA-AuNP start to form within the growing stem cell colony. At the later timepoints MBA-AuNP can be seen clustering in the perinuclear area.

More detailed observation of the timelapse acquisitions shows that MBA-AuNP uptake from the surrounding matrix appears to be via filopodial and lamellipodial protrusions at the edges of the colonies as they expand and grow (Figure 23 and Figure 24). Figure 23 shows example images at 10 min intervals of MBA-AuNP being actively taken up via filopodial projections, whereas Figure 24 shows uptake via lamellipodial protrusions. MBA-AuNP can be seen clustering and being transported towards the perinuclear regions of the cell (Supplementary Movies 1, 2 and 3). Filopodia and lamellipodia are protrusion phenomena seen during normal cell adhesion, growth, and motility. They are generally considered to be regulated by the family of small Rac and Rho GTPases involved in cytoskeletal remodelling [90]. Both protrusion types play central roles in the cell's ability to sense, respond to, and navigate extracellular stimuli and environments.

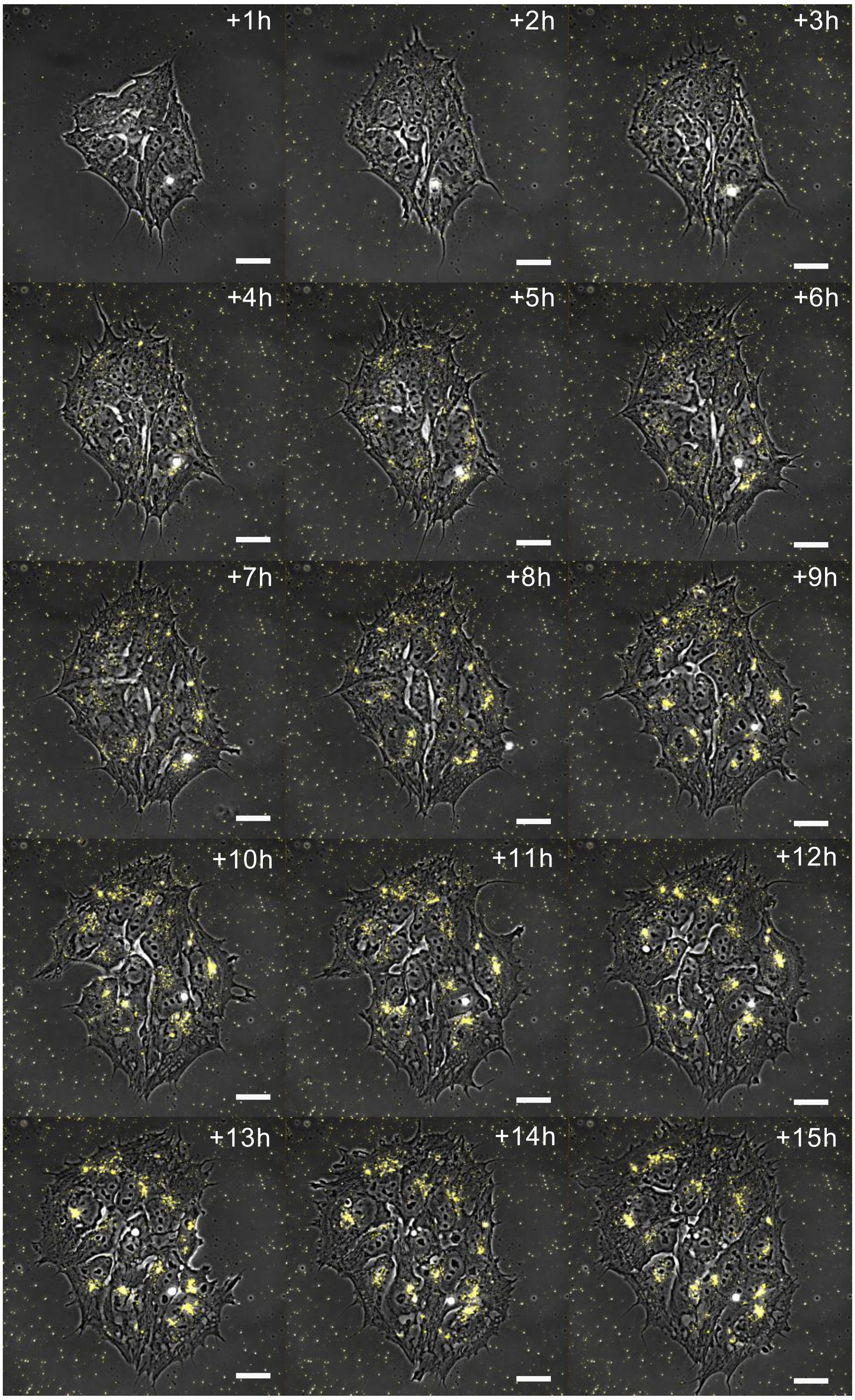

Figure 22. Timelapse of MBA-AuNP uptake using phase contrast microscopy
One-hour-interval frames taken from RC9 timelapse movie acquired using a 63x oil immersion objective, phase contrast, and brightfield illumination, starting from 1 hr after addition of MBA-AuNP. Colonies are visible in phase contrast and MBA-AuNP are visible in yellow pseudocolour of the brightfield channel with inverted LUT. Scale bars are 50 µm.

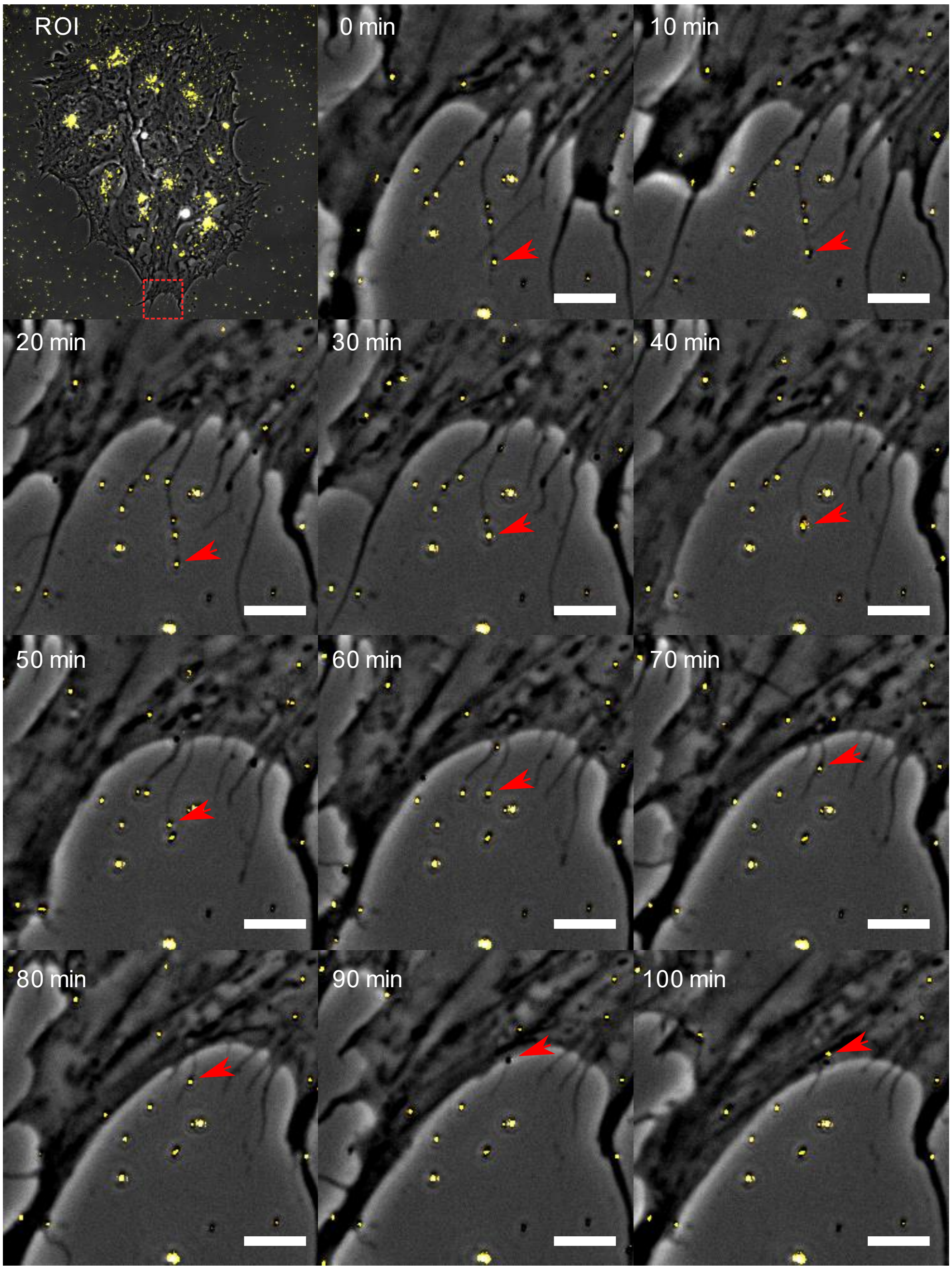

Figure 23. High-magnification timelapse of cellular MBA-AuNP uptake mechanism – Filopodia
Ten-minute-interval frames taken from RC9 timelapse movie acquired using a 63x oil immersion objective, phase contrast, and brightfield illumination. A 100-minute segment was used to highlight filopodial uptake. Cells are visible in phase contrast and MBA-AuNP are visible in yellow pseudocolour of the brightfield channel with inverted LUT. Whole-field image of colony is overlaid with a red box indicating the region used for the timelapse montage. Red arrows highlight an example MBA-AuNP that can be tracked across the timelapse montage. Scale bars are 5 µm.

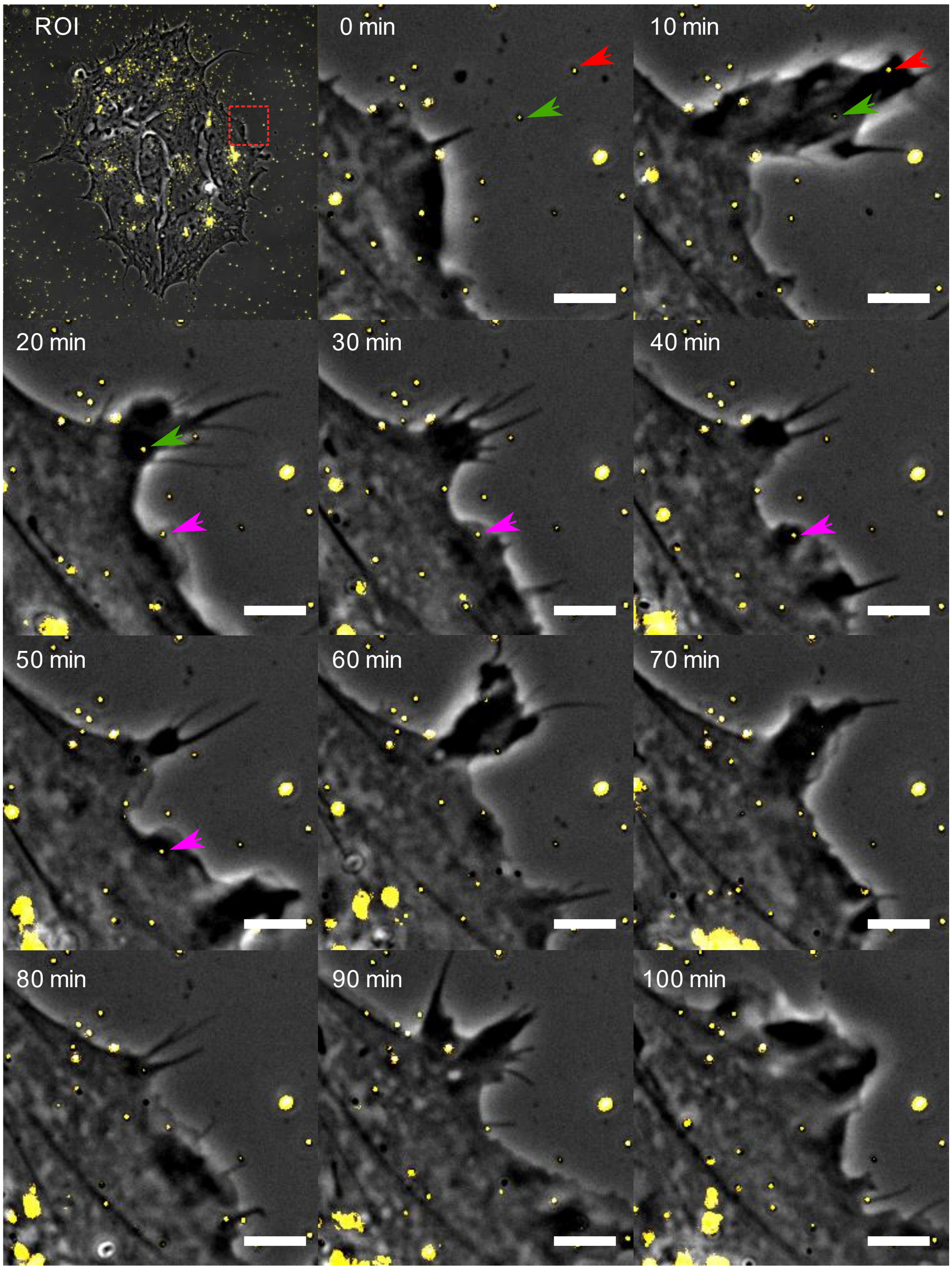

Figure 24. High-magnification timelapse of cellular MBA-AuNP uptake mechanism – Lamellipodial ruffles

Ten-minute-interval frames taken from RC9 timelapse movie acquired using a 63x oil immersion objective, phase contrast, and brightfield illumination. A 100-minute segment was used to highlight ruffling lamellipodium uptake. Cells are visible in phase contrast and MBA-AuNP are visible in yellow pseudocolour of the brightfield channel with inverted LUT. Whole-field image of colony is overlaid with a red box indicating the region used for the timelapse montage. Coloured arrows highlight example MBA-AuNPs that can be tracked across the timelapse montage. Scale bars are 5 µm.

6.3 Localisation of AuNP using confocal laser scanning microscopy

To accurately interpret the pH values collected from cells, it was important to confirm the intracellular location of the MBA-AuNP within cells. In section 6.2 we showed that MBA-AuNP are taken up, transported, and eventually accumulate in perinuclear regions. Studies have found gold nanoparticles to accumulate within vesicles such as endosomes and lysosomes [91]. To confirm whether this was the case for the MBA-AuNP in this study we utilised laser scanning confocal microscopy. Gold nanoparticles can be visualised label-free by collecting laser light that reflects off their surface, and lysosomes can be stained using conventional fluorescently labelled antibodies. For these experiments two lysosomal markers were assessed, LAMP1 and LAMP2. LAMP1 and LAMP2 are estimated to make up roughly 50% of the lysosomal membrane, making them two of the most abundant lysosomal membrane proteins [92]. Cells were stained using primary antibodies for LAMP1 and LAMP2 after 24 hours and 96 hours of incubation with MBA-AuNP (section 4.5.2.1).

6.3.1 Validation of 3D object detection

Images were recorded as described in section 4.5.2.2. To assess and visualise the association of MBA-AuNP with LAMP signal an object detection protocol was created using dedicated image analysis software, Volocity 6.2. Objects were detected in both LAMP and MBA-AuNP channels and were classified as either colocalised, where the LAMP and MBA-AuNP are intimately associated, and non-colocalised, where the LAMP and MBA-AuNP, though sometimes in close proximity, are not intimately associated. To visualise all MBA-AuNP within the image field the confocal Z-stacks were displayed as maximum intensity projections, where all Z planes are flattened together into one single image. These maximum intensity projections have been used to present all immunofluorescence images in figures throughout this study. However, to prevent inaccurate identification of associated objects all object detection was conducted in the native 3D confocal z-stacks. As proof of principle, examples of the 3D object detection can be visualised in Figure 25 to Figure 28. Figure 25 highlights a region in which a maximum intensity projection appears to show a localisation event where the LAMP and MBA-AuNP are not, in fact, truly localised. When observing this image as a maximum intensity projection the LAMP and MBA-AuNP appear to be associated within the bounding box (dotted red line). However, by utilising 3D object detection it is clear that they are not closely associated, as the bounding boxes of the detected objects do not overlap in any dimension (Figure 26).

Figure 27, conversely, shows an example of a real colocalisation event. Again, LAMP and MBA-AuNP appear colocalised when observing the image in maximum intensity projection (Figure 27), similarly to what was seen in the non-localised event. However, the true colocalisation can be confirmed by utilising 3D object detection and visualisation (Figure 28), which show clear overlap between bounding boxes of the detected objects.

As such, visual overlapping signal in maximum intensity projections does not mean a true dual-object colocalisation. By utilising 3D object detection false positives were minimised and true colocalizing objects were accurately identified, highlighting the importance of 3-dimensional imaging and analysis when looking at subcellular phenomena.

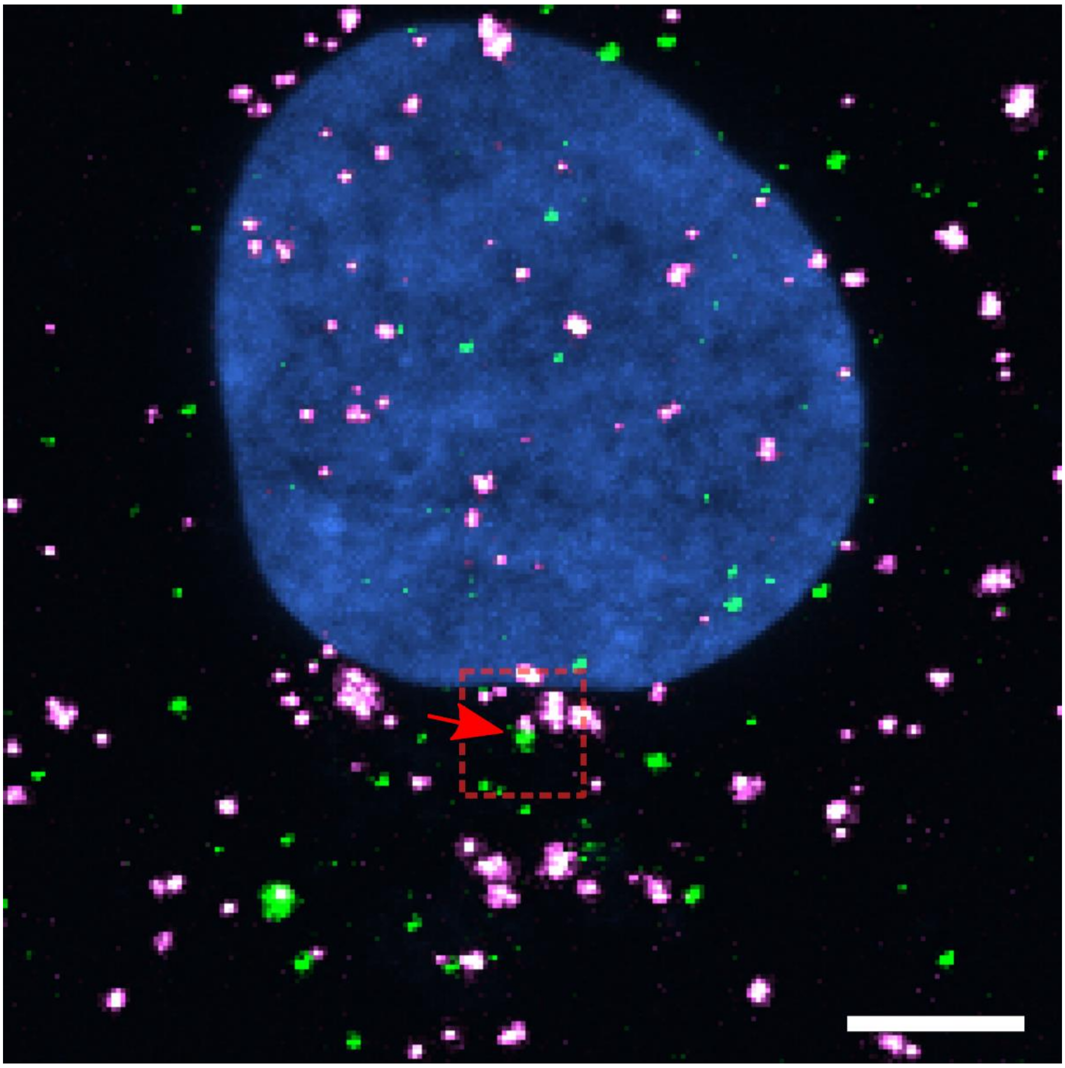

Figure 25. Non-localised close proximity LAMP and MBA-AuNP fluorescence
Representative maximum intensity projection LAMP-2 immunofluorescence and reflection confocal images (IF) of RC9 hESC cultures after 96-hour incubation with MBA-AuNP. Image shows IF overlay of Hoechst (blue), LAMP-2 (green), and AuNP (magenta). Red box and red arrow indicate the region and nanoparticle cluster used for magnified images in Figure 26.
Scale bar is 5 µm.

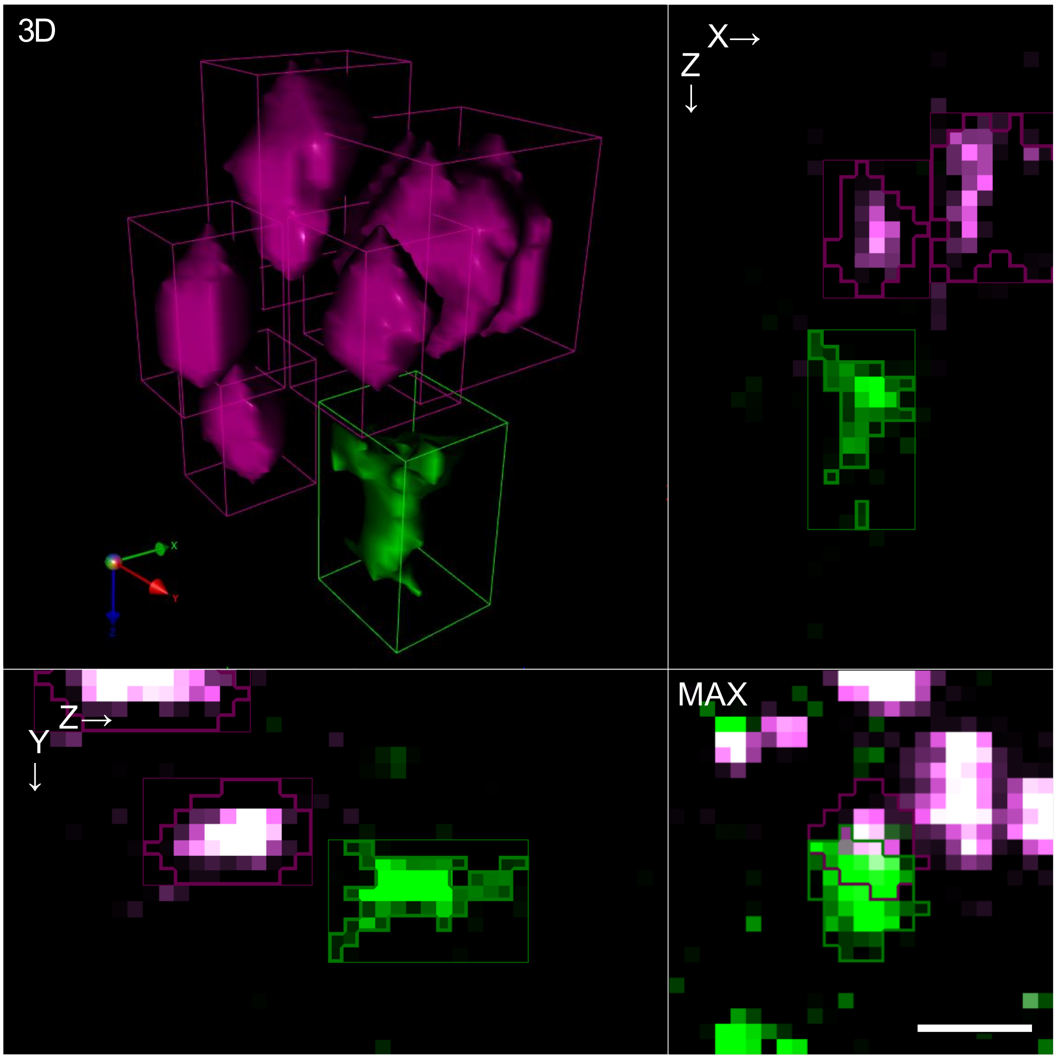

Figure 26. Close-up objects of non-localised close proximity LAMP and MBA-AuNP fluorescence
Inset region from Figure 25 showing physical separation of objects that appear colocalised in a maximum intensity projection. Image shows IF overlays of LAMP-2 (green), and AuNP (magenta). Detected objects are highlighted in magenta (MBA-AuNP) and green (LAMP) and are surrounded by the bounding box of the object. Orthogonal views XZ & YZ, and 3D view all show the clear separation of the objects that appear colocalised in the maximum intensity projection (MAX). Objects from MAX have been removed for clarity. Scale bar is 1 µm.

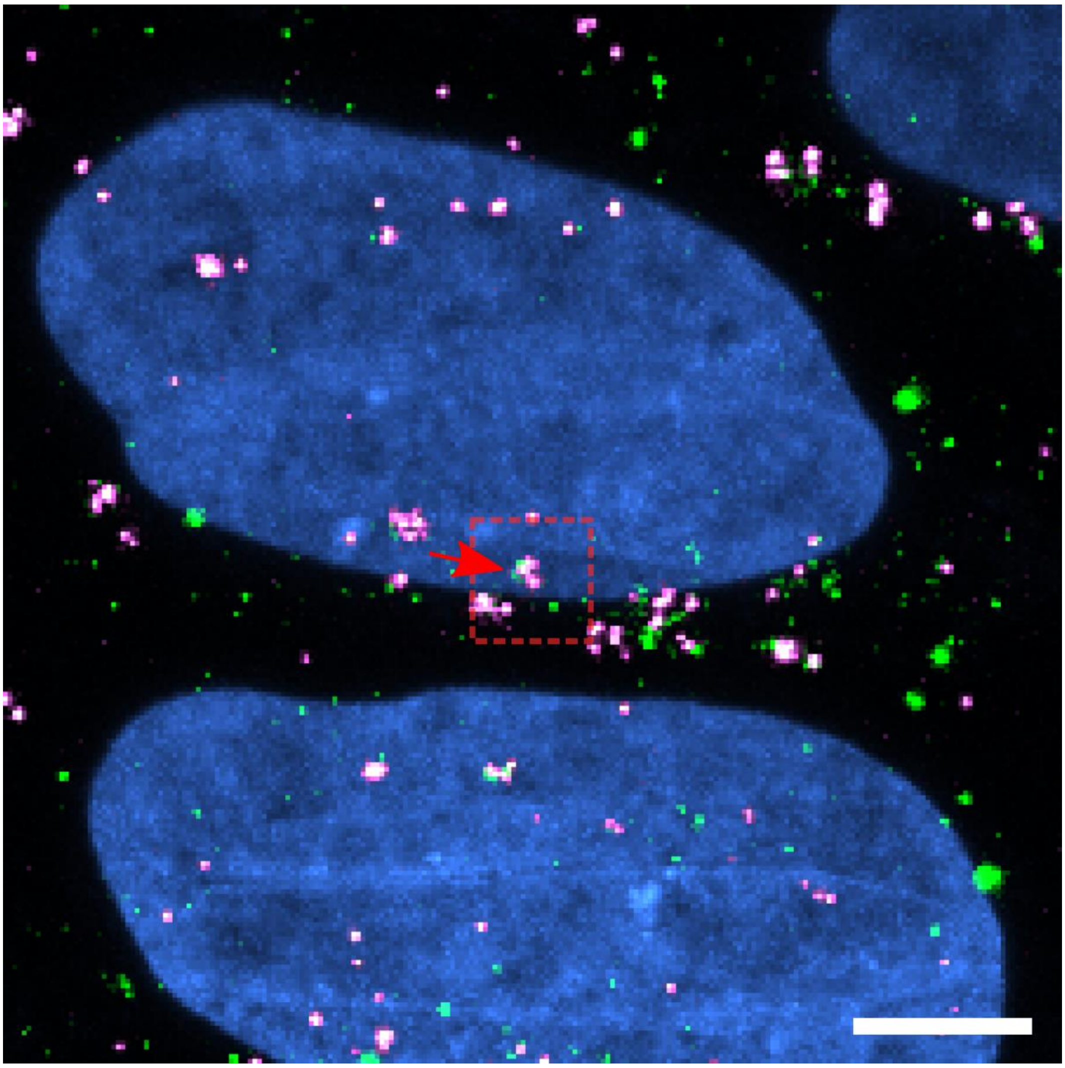

Figure 27.Colocalised close proximity LAMP and MBA-AuNP fluorescence
Representative maximum intensity projection LAMP-1 immunofluorescence and reflection confocal images (IF) of RC9 hESC cultures after 96-hour incubation with MBA-AuNP. Image shows IF overlay of Hoechst (blue), LAMP-1 (green), and AuNP (magenta). Red box and red arrow indicate the region and nanoparticle cluster used for magnified images in Figure 28.
Scale bar is 5 µm.

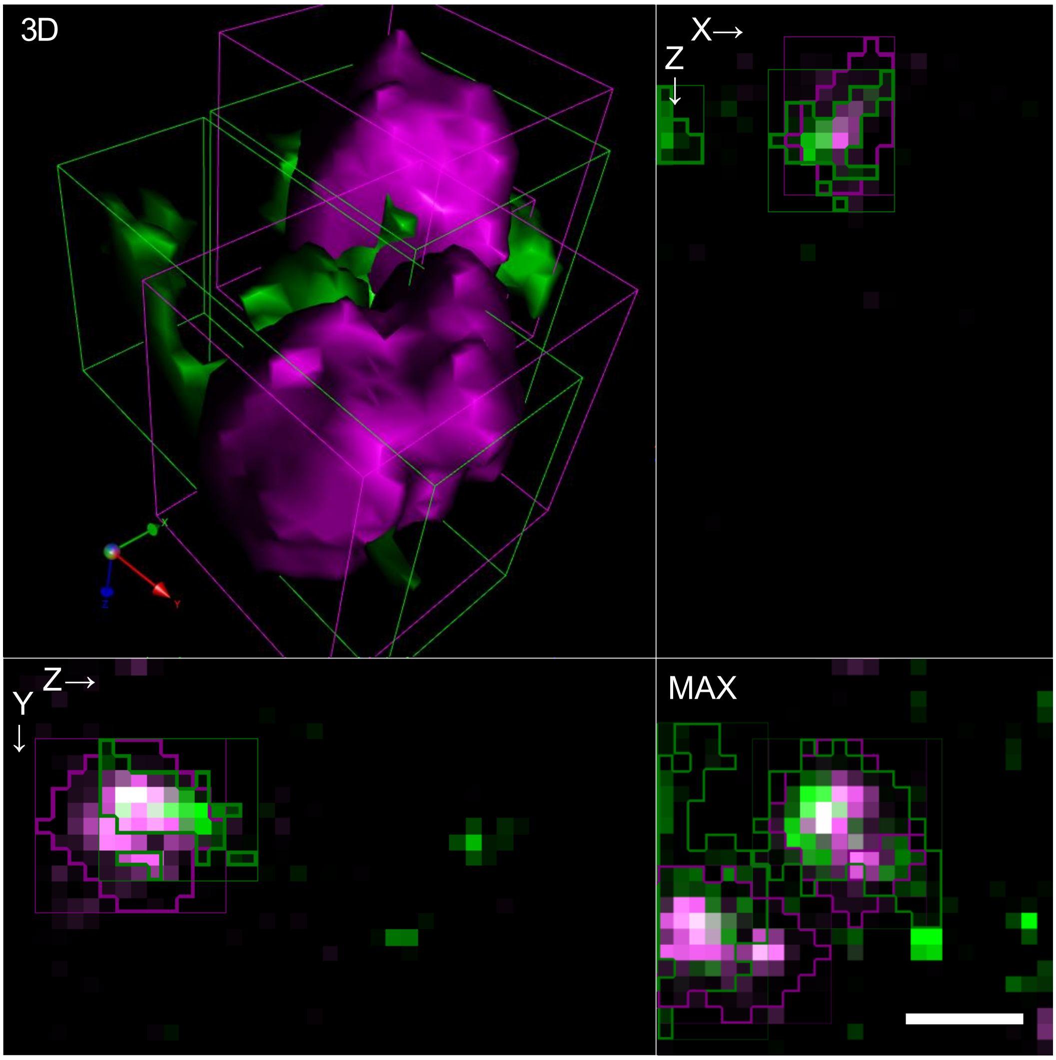

Figure 28. Close-up objects of colocalised close proximity LAMP and MBA-AuNP fluorescence
Inset region from Figure 27 showing high degree of overlap between objects that identified as positively associated MBA-AuNP-LAMP-1 objects. Image shows IF overlays of LAMP-2 (green), and AuNP (magenta). Detected objects are highlighted in magenta (MBA-AuNP) and green (LAMP) and are surrounded by the bounding box of the object. Orthogonal views XZ & YZ, and 3D view all show a considerable overlap in fluorescence, object outlines, and object boundary boxes in all three imaging axes. Scale bar is 1 µm.

6.3.2 Lysosomal uptake of MBA-AuNP after 24h

The uptake of MBA-AuNP by RC9 hESC was assessed after 24 hours incubation. LAMP was visualised by fluorescent excitation using a 488nm laser. Since MBA-AuNP are reflective these could be detected by collecting the reflected light of the 633nm laser.

MBA-AuNP can be seen accumulating perinuclearly (Figure 29, top and middle panels). No MBA-AuNP signal was detected in control cells which had not been incubated or treated with MBA-AuNP and LAMP primary antibodies, confirming that the reflected signal arises from MBA-AuNP presence (Figure 29, bottom panels). Examples of the object detection for LAMP-1 can be seen in Figure 30. LAMP-1 staining can be seen as an abundance of small spots all over the cells, but particularly dense in the perinuclear area (Figure 29, Figure 30). Clusters of very dense LAMP-1 spots are almost exclusively perinuclear. Visually, there is a clear overlapping localisation of LAMP-1 and AuNP, but this will be quantified in section 6.3.4.

The staining pattern from LAMP-2 differs from that of LAMP-1 with far fewer, but brighter, spots all over the cells (Figure 31, Figure 32). Conversely to LAMP-1, no clear visual perinuclear accumulation could be observed for LAMP-2. Since both LAMP-1 and LAMP-2 primary antibodies were detected using the same fluorescent secondary antibody, this observation can be solely attributed to the binding of the primary antibodies. In addition to fewer LAMP-2 objects, no obvious association between LAMP-2 objects and MBA-AuNP could be detected, but again, this observation will be quantified in section 6.3.4.

Careful consideration was given to the object detection parameters, including size filtering and intensity of the detected objects to prevent false positives. As can be seen, some green areas are still not detected as objects (Figure 30, bottom two panels) - a result from the stringent object detection parameters which ensured minimum false positive LAMP detection. So, in reality the association between AuNP and LAMP may be higher than what is portrayed here. In secondary antibody control images, there is invariably occurrences of occasional bright spots, despite the lack of primary antibody onto which the fluorescent secondary binds. This is most likely due to small aggregates of secondary antibody or due to rare occurrences of non-specific binding. These bright spots are similar in appearance to the spots seen with LAMP staining because of the size and nature of the target protein. However, they are rare and, when staining conditions are well optimised, contribute at most only one or two single spots in any of the images, as is the case with this study. In addition to this, and as a result of the very sensitive imaging equipment used, there is invariably background electronic pixel noise in any digital image. This pixel shot noise must be eliminated from any analysis. For this reason, the object detection was set so that no more than two false “LAMP” objects, i.e., those arising from secondary antibody aggregates, were ever detected in the secondary antibody controls.

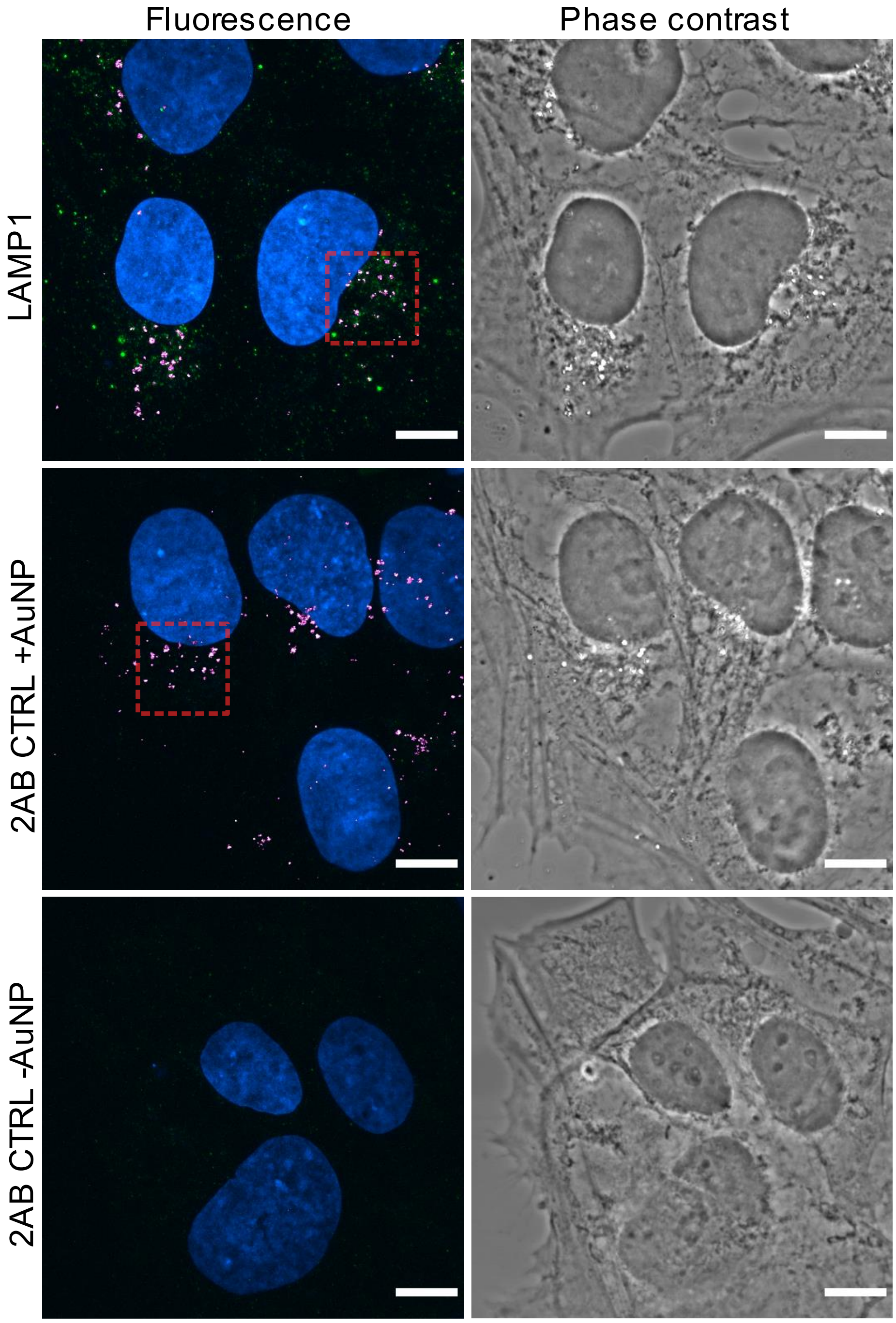

Figure 29. Intracellular localisation of LAMP-1 and AuNP within RC9 hESC after 24h incubation
Representative maximum intensity projection LAMP-1 immunofluorescence (IF) and reflection confocal images of RC9 hESC cultures after 24-hour incubation with MBA-AuNP. Left panels are multichannel IF overlays of Hoechst (blue), LAMP-1 (green), and AuNP (magenta). Right panels are matching single-confocal-plane images in phase contrast. Top panels show cells incubated with primary and secondary antibody for LAMP-1 staining. Middle panels show cells incubated with secondary antibody alone. Bottom panels show secondary-antibody-incubated cells without MBA-AuNP. Red boxes indicate regions use for magnified images in Figure 30.
Scale bars are 10 µm.

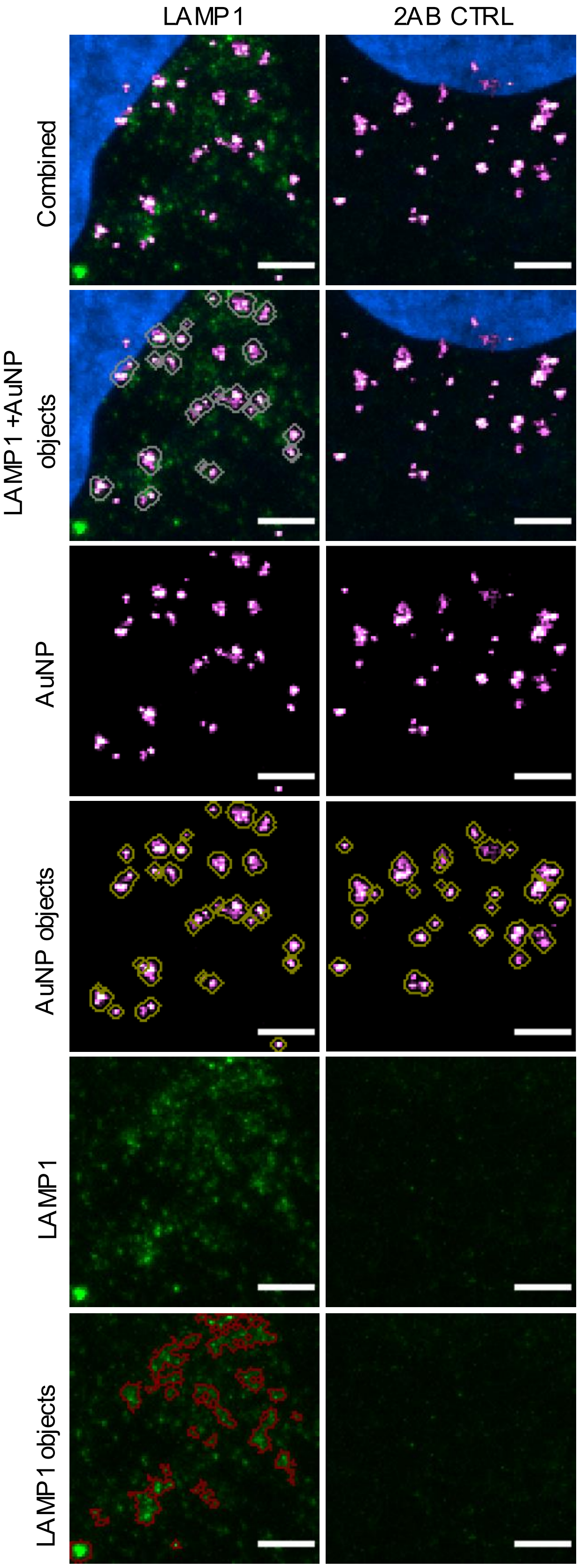

Figure 30. High magnification images of LAMP-1 and AuNP intracellular localisation and object detection

Inset regions taken from Figure 29 showing maximum intensity projection immunofluorescence and reflection confocal images of LAMP-1 staining and AuNP reflection overlaid with detected objects for quantification. Left panels show LAMP-1 stained images and right panels show secondary antibody control images. From top to bottom images show: combined LAMP-1, AuNP, & Hoechst; combined LAMP-1, AuNP, & Hoechst with detected objects positive for both LAMP-1 and AuNP (white outlines); AuNP alone; AuNP with detected objects (yellow objects); LAMP-1 alone; LAMP-1 with detected objects (red outlines). Scale bars are 3 µm.

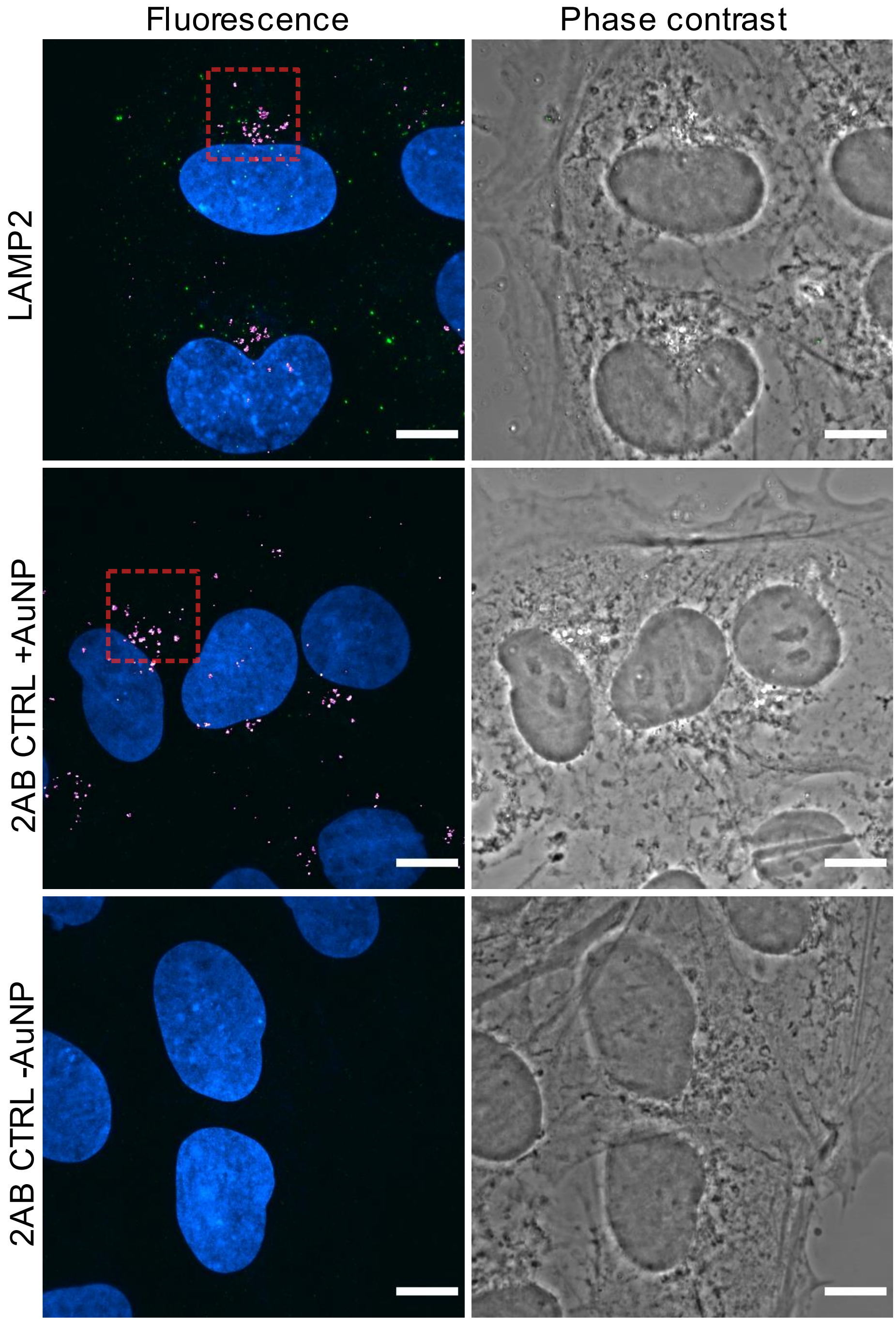

Figure 31. Intracellular localisation of LAMP-2 and AuNP within RC9 hESC after 24h incubation
Representative maximum intensity projection LAMP-2 immunofluorescence (IF) and reflection confocal images of RC9 hESC cultures after 24-hour incubation with MBA-AuNP. Left panels are multichannel IF overlays of Hoechst (blue), LAMP-2 (green), and AuNP (magenta). Right panels are matching single-confocal-plane images in phase contrast. Top panels show cells incubated with primary and secondary antibody for LAMP-2 staining. Middle panels show cells incubated with secondary antibody alone. Bottom panels show secondary-antibody-incubated cells without MBA-AuNP. Red boxes indicate regions use for magnified images in Figure 32.
Scale bars are 10 µm.

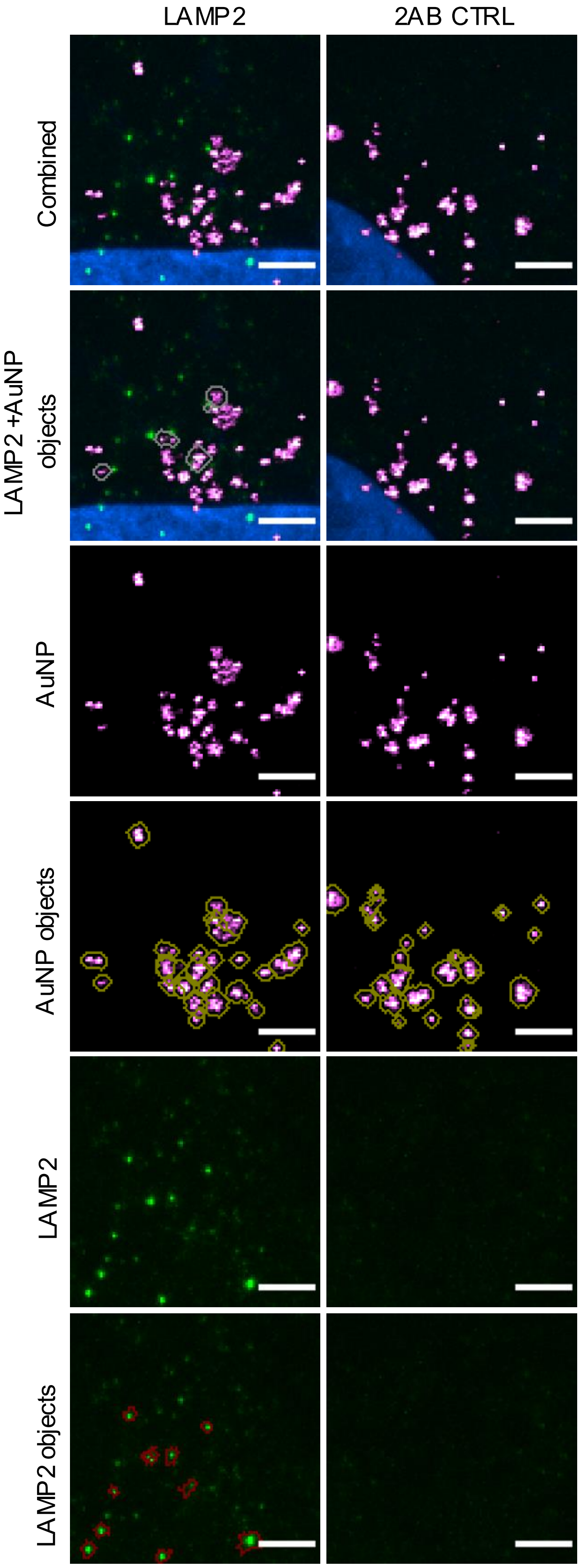

Figure 32. High magnification images of LAMP-2 and AuNP intracellular localisation and object detection

Inset regions taken from Figure 31 showing maximum intensity projection immunofluorescence and reflection confocal images of LAMP-2 staining and AuNP reflection overlaid with detected objects for quantification. Left panels show LAMP-2 stained images and right panels show secondary antibody control images. From top to bottom images show: combined LAMP-2, AuNP, & Hoechst; combined LAMP-2, AuNP, & Hoechst with detected objects positive for both LAMP-2 and AuNP (white outlines); AuNP alone; AuNP with detected objects (yellow objects); LAMP-2 alone; LAMP-2 with detected objects (red outlines). Scale bars are 3 µm.

6.3.3 Lysosomal uptake of MBA-AuNP after 96h

The uptake of MBA-AuNP into RC9 cells and their co-localisation with LAMP-1 and LAMP-2 positive lysosomes was also assessed 96 hours after MBA-AuNP addition (Figure 33 - Figure 36). This was done to make an assessment of the location of the MBA-AuNP after several days' incubation, so that it would be possible to confidently acquire pH measurements from similar locations to those done after 24 hours, allowing time-course experiments to be performed.

As can be seen in Figure 33 - Figure 36, MBA-AuNP still accumulate perinuclearly, and the staining patterns of both LAMP-1 and LAMP-2 are visually similar to what was observed after a 24 hour incubation with MBA-AuNP (section 6.3.2). Again, more LAMP objects and co-localised objects are detected for LAMP-1 compared to LAMP-2. This gave confidence in the supposition that as long as pH measurements are acquired in similar perinuclear regions, the likelihood of measuring the same type of cellular compartment would be high enough to draw conclusions regarding temporal pH changes.

Again, quantification of all the detected objects identified in Figure 34 and Figure 36 can be found in section 6.3.4.

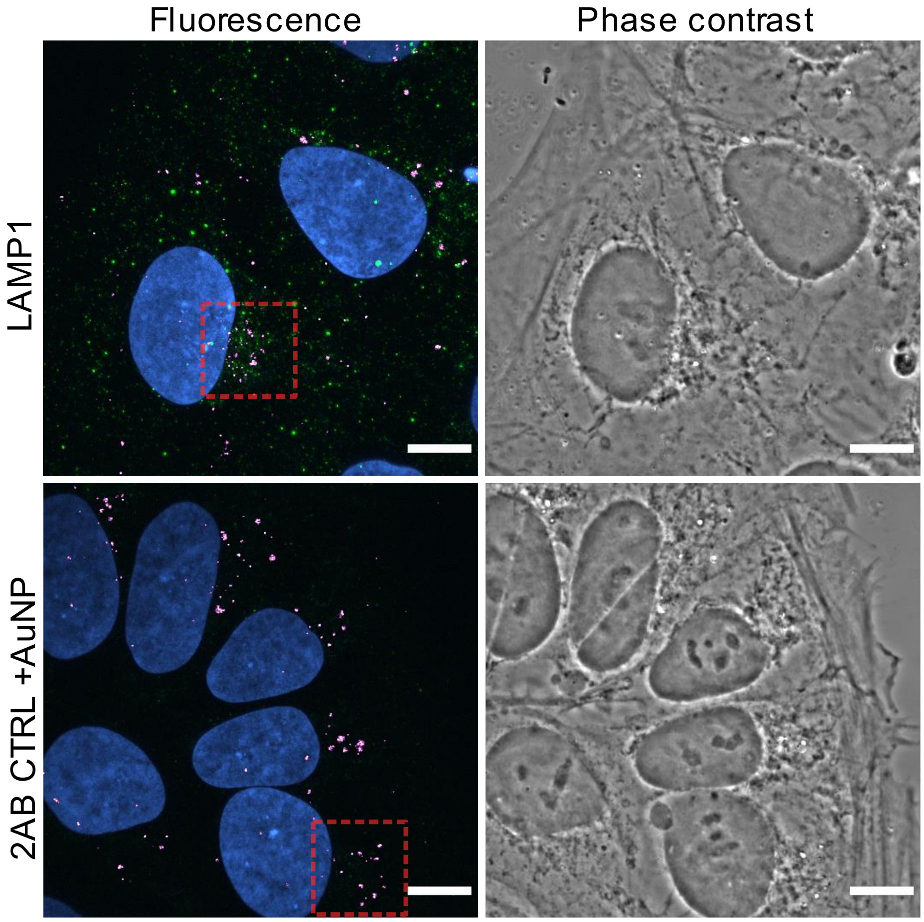

Figure 33. Intracellular localisation of LAMP-1 and AuNP within RC9 hESC after 96h incubation
Representative maximum intensity projection LAMP-1 immunofluorescence and reflection confocal images (IF) of RC9 hESC cultures after 96-hour incubation with MBA-AuNP. Left panels are multichannel IF overlays of Hoechst (blue), LAMP-1 (green), and AuNP (magenta). Right panels are matching single-confocal-plane images in phase contrast. Top panels show cells incubated with primary and secondary antibody for LAMP-1 staining. Middle panels show cells incubated with secondary antibody alone. Red boxes indicate regions use for magnified images in Figure 34. Scale bars are 10 µm.

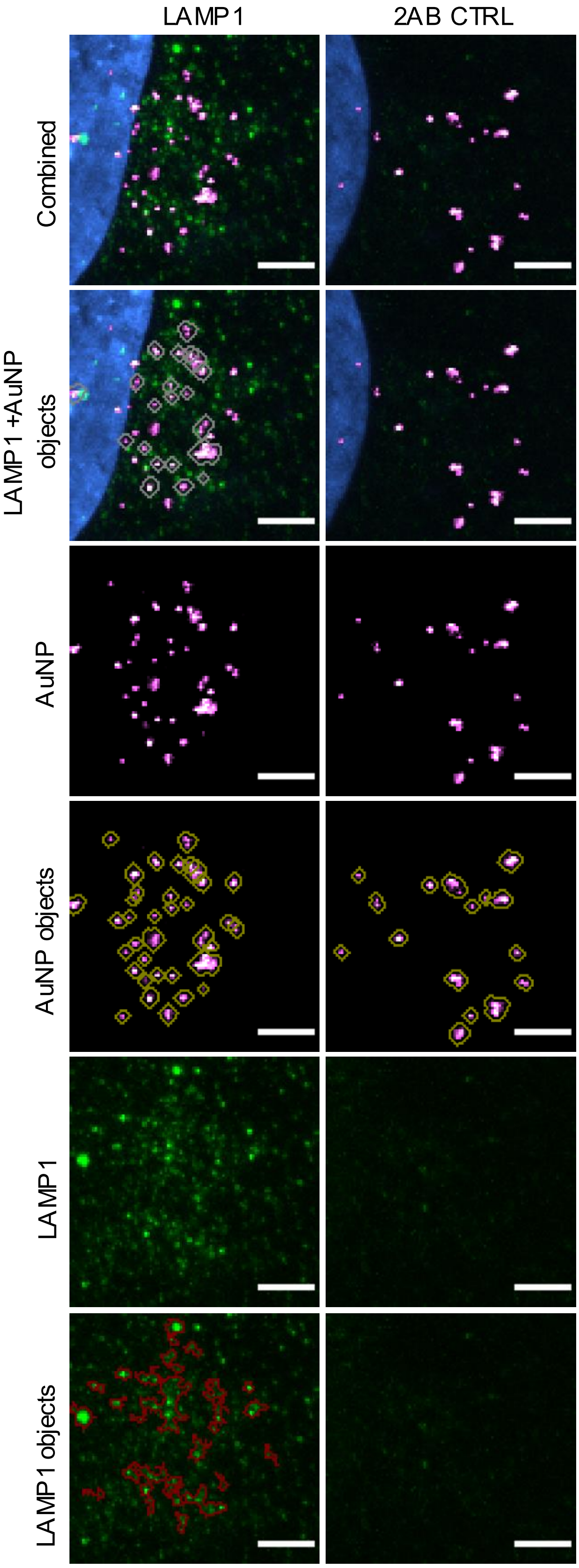

Figure 34. High magnification images of LAMP-1 and AuNP intracellular localisation and object detection after 96h AuNP incubation

Inset regions taken from Figure 33 showing maximum intensity projection immunofluorescence and reflection confocal images of LAMP-1 staining and AuNP reflection overlaid with detected objects for quantification. Left panels show LAMP-1 stained images and right panels show secondary antibody control images. From top to bottom images show: combined LAMP-1, AuNP, & Hoechst; combined LAMP-1, AuNP, & Hoechst with detected objects positive for both LAMP-1 and AuNP (white outlines); AuNP alone; AuNP with detected objects (yellow objects); LAMP-1 alone; LAMP-1 with detected objects (red outlines). Scale bars are 3 µm.

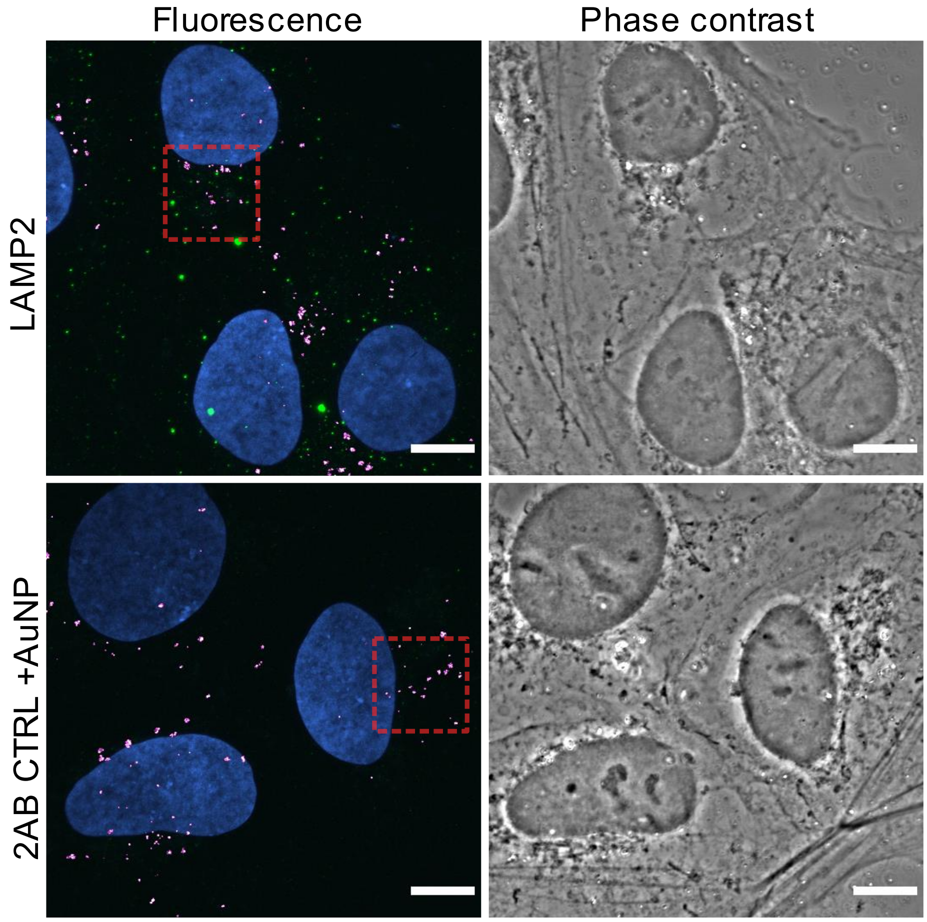

Figure 35. Intracellular localisation of LAMP-2 and AuNP within RC9 hESC after 96h incubation Representative maximum intensity projection LAMP-2 immunofluorescence and reflection confocal images (IF) of RC9 hESC cultures after 96-hour incubation with MBA-AuNP. Left panels are multichannel IF overlays of Hoechst (blue), LAMP-2 (green), and AuNP (magenta). Right panels are matching single-confocal-plane images in phase contrast. Top panels show cells incubated with primary and secondary antibody for LAMP-2 staining. Middle panels show cells incubated with secondary antibody alone. Red boxes indicate regions use for magnified images in Figure 36. Scale bars are 10 µm.

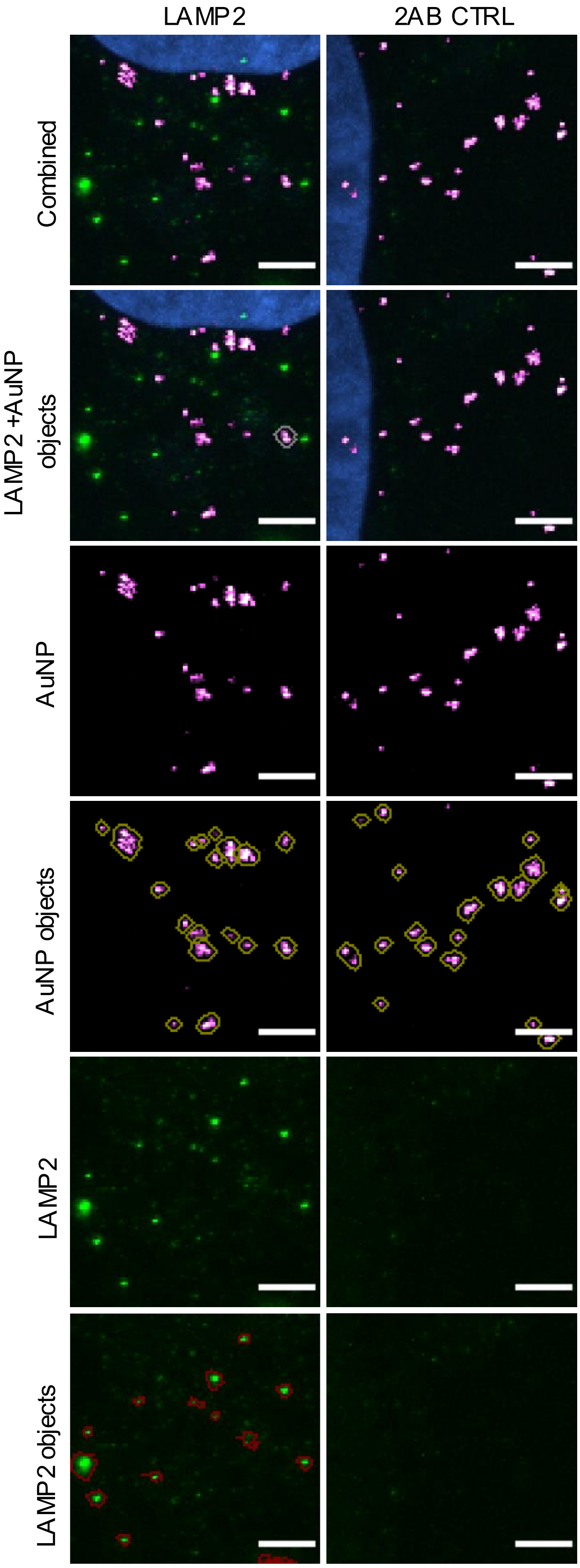

Figure 36. High magnification images of LAMP-2 and AuNP intracellular localisation and object detection after 96h AuNP incubation

Inset regions taken from Figure 35 showing maximum intensity projection immunofluorescence and reflection confocal images of LAMP-2 staining and AuNP reflection overlaid with detected objects for quantification. Left panels show LAMP-2 stained images and right panels show secondary antibody control images. From top to bottom images show: combined LAMP-2, AuNP, & Hoechst; combined LAMP-2, AuNP, & Hoechst with detected objects positive for both LAMP-2 and AuNP (white outlines); AuNP alone; AuNP with detected objects (yellow objects); LAMP-2 alone; LAMP-2 with detected objects (red outlines). Scale bars are 3 µm.

6.3.4 Quantification of LAMP associated MBA-AuNP

For quantification of the number of objects detected in section 6.3.2 and 6.3.3, the total number of objects detected in Volocity software was exported and plotted in OriginLab. The results of the quantification of objects after 24 hours and 96 hours can be seen in Figure 37 and Figure 38 respectively.

Figure 37 show the number of detected objects per collected field after 24 hours incubation with MBA-AuNP. The number of LAMP-1 objects was significantly higher than LAMP-2 objects (Figure 37A), consistent with visual observation in previous sections. No more than two false LAMP objects were detected in the secondary control, showing that the detection parameters are valid and robust. No significant difference was detected in the number of MBA-AuNP between secondary antibody controls and LAMP-stained samples, which means that any differences observed in LAMP and MBA-AuNP co-localisation is due to differences in the LAMP staining and not number of MBA-AuNP (Figure 37B). The number of LAMP associated MBA-AuNP was significantly greater for LAMP-1 compared to LAMP-2 (Figure 37C). To normalise the number of LAMP associated MBA-AuNP to the number of total MBA-AuNP of the field, the percentage of total MBA-AuNP objects that were associated with LAMP was also plotted (Figure 37D). As seen, a range of 13.47-79.41% of the total MBA-AuNP per field for LAMP-1, compared to only 0.00-13.48% for LAMP-2, were associated with corresponding antibody stain.

The results for the quantification of cells after 96 hours of incubation followed the same patterns as for 24 hours of incubation (Figure 38). A notable difference is that the number of LAMP objects detected increased markedly from a median of 83.5 to 183 for LAMP-1 and slightly from 62 to 74.5 for LAMP-2, suggesting an upregulation of overall LAMP expression. The median of MBA-AuNP, however, decreased from 163, 155, 164, and 188.5 to 93, 102, 93.5, and 110 for LAMP-1 secondary control and stain and LAMP-2 secondary control and stain respectively. As no MBA-AuNP was added to the medium after the initial addition, this can be attributed to the expulsion of MBA-AuNP from cells and dilution during cell division, as well as further clustering of MBA-AuNP within vesicles. As a result, fewer LAMP associated MBA-AuNP are detected. The median for the percentage of MBA-AuNP associated with LAMP-1, however, increases from is 28.8% to 46% whereas it stays roughly the same for LAMP-2 with 4.4% at 24 hours and 4.3% at 96 hours. So even if the total number of MBA-AuNP decreases a larger percentage of the remaining particles are associated with LAMP-1.

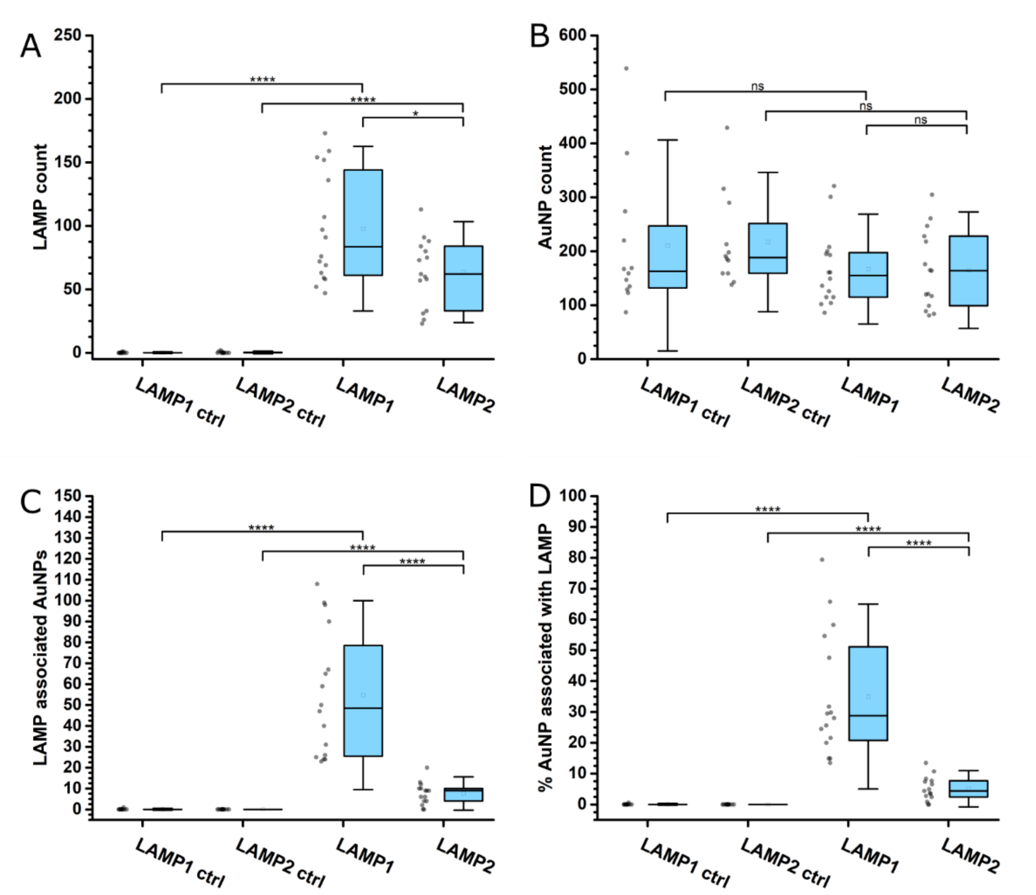

Figure 37. Quantification of LAMP after 24h incubation

Count of LAMP-positive objects and MBA-AuNP-positive objects were tallied for at least 12 fields of confocal images over three technical repeats. (A) LAMP-positive objects detected for LAMP-1 IF, LAMP-2 IF, and both LAMP-1 and LAMP-2 2°AB-only control; (B) MBA-AuNP-positive objects detected for LAMP-1 IF, LAMP-2 IF, and both LAMP-1 and LAMP-2 2°AB-only control; (C) Counts of objects detected as simultaneously positive for both LAMP & MBA-AuNP; (D) Percentage of total MBA-AuNP objects also associated with LAMP-IF positivity. Box & whisker plots show the 25-75th percentile, midline represent the median, and error bars represent SD. Dots represent values from individual image fields (LAMP1 ctrl, n = 12; LAMP2 ctrl, n = 12; LAMP1, n = 16; LAMP2, n = 15). P-values: ns > 0.05, * < 0.05, ** < 0.01, *** < 0.001, **** < 0.0001, Mann-Whitney test.

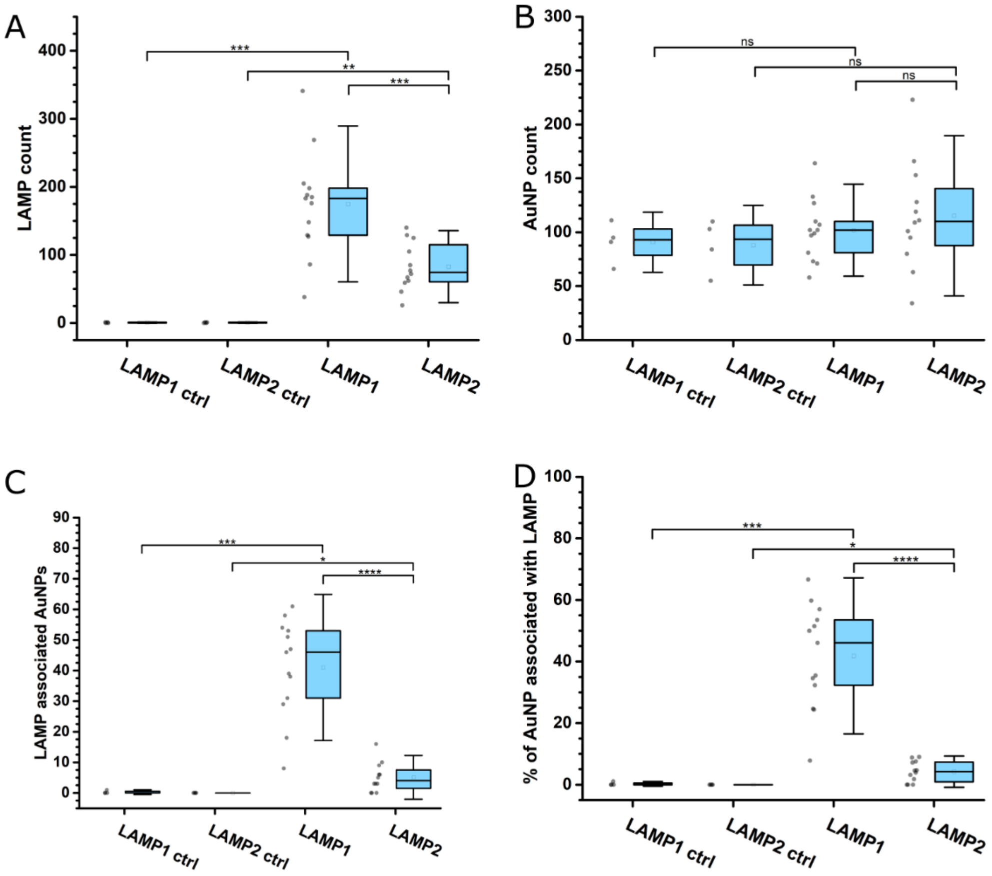

Figure 38. Quantification of LAMP after 96h incubation

Count of LAMP-positive objects and MBA-AuNP-positive objects were tallied for at least 12 fields (except control (=4 fields)) of confocal images over three technical repeats. (A) LAMP-positive objects detected for LAMP-1 IF, LAMP-2 IF, and both LAMP-1 and LAMP-2 2°AB-only control; (B) MBA-AuNP-positive objects detected for LAMP-1 IF, LAMP-2 IF, and both LAMP-1 and LAMP-2 2°AB-only control; (C) Counts of objects detected as simultaneously positive for both LAMP & MBA-AuNP; (D) Percentage of total MBA-AuNP objects also associated with LAMP-IF positivity. Box & whisker plots show the 25-75th percentile, midline represent the median, and error bars represent SD. Dots represent values from individual image fields (LAMP1 ctrl, n = 4; LAMP2 ctrl, n = 4; LAMP1, n = 13; LAMP2, n = 12).

P-values: ns > 0.05, * < 0.05, ** < 0.01, *** < 0.001, **** < 0.0001, Mann-Whitney test.

6.4 Growing cells on CaF_2 for SERS

Before carrying out any Raman experiments, we needed to optimise the culture of the cells onto a suitable substrate since normal plastic or glass-bottomed plates create a high background spectrum. To perform Raman measurements, samples are often placed on calcium fluoride (CaF_2) substrates, since they have the desired optical properties to allow high signal to noise measurements. For certain cell types, such as MCF7 breast cancer cells, growing the cells on CaF_2 does not interfere with normal function and behaviour as the cells readily attach to the surface without the need for extracellular matrix proteins or adhesion-promoting coatings. For hESC, however, the surface needs to be coated with a cell culture matrix for cell attachment. During routine culture vitronectin was used to coat cell culture treated plasticware. Using vitronectin alone to coat CaF_2 resulted in only moderate attachment, and colonies often formed small spheres on day 1 post-passage, indicating poor adherence (Phase contrast image, Figure 39C). To improve the attachment of the hESC colonies to the CaF_2 discs a coating of poly-l-lysine was tested and applied prior to vitronectin coating. Phase contrast images were collected one day after passaging of hESC colonies, and cells were stained with Giemsa stain four days after passaging (for further information see section 4.1.5.2). Clear improvements were observed when simultaneously coating CaF_2 discs with poly-l-lysine and vitronectin; with virtually no spherical clumps of cells, and greater coverage of the disc surface (Figure 39, E) similar to that of the standard vitronectin coated plastic (Figure 39, G). No cells attached to untreated CaF_2 discs, as expected (Figure 39, A). On day three post-passaging the cells were fixed and stained with Giemsa, to visualise the cell density and coverage using the various coatings (Figure 39, B, D, F, and H). The cell coverage three days after passaging was also higher on CaF_2 coating with both poly-l-lysine and vitronectin compared to vitronectin alone (Figure 39, F and D respectively). Again, attachment on CaF_2 coated with poly-l-lysine and vitronectin was similar to standard culture conditions (Figure 39, H).

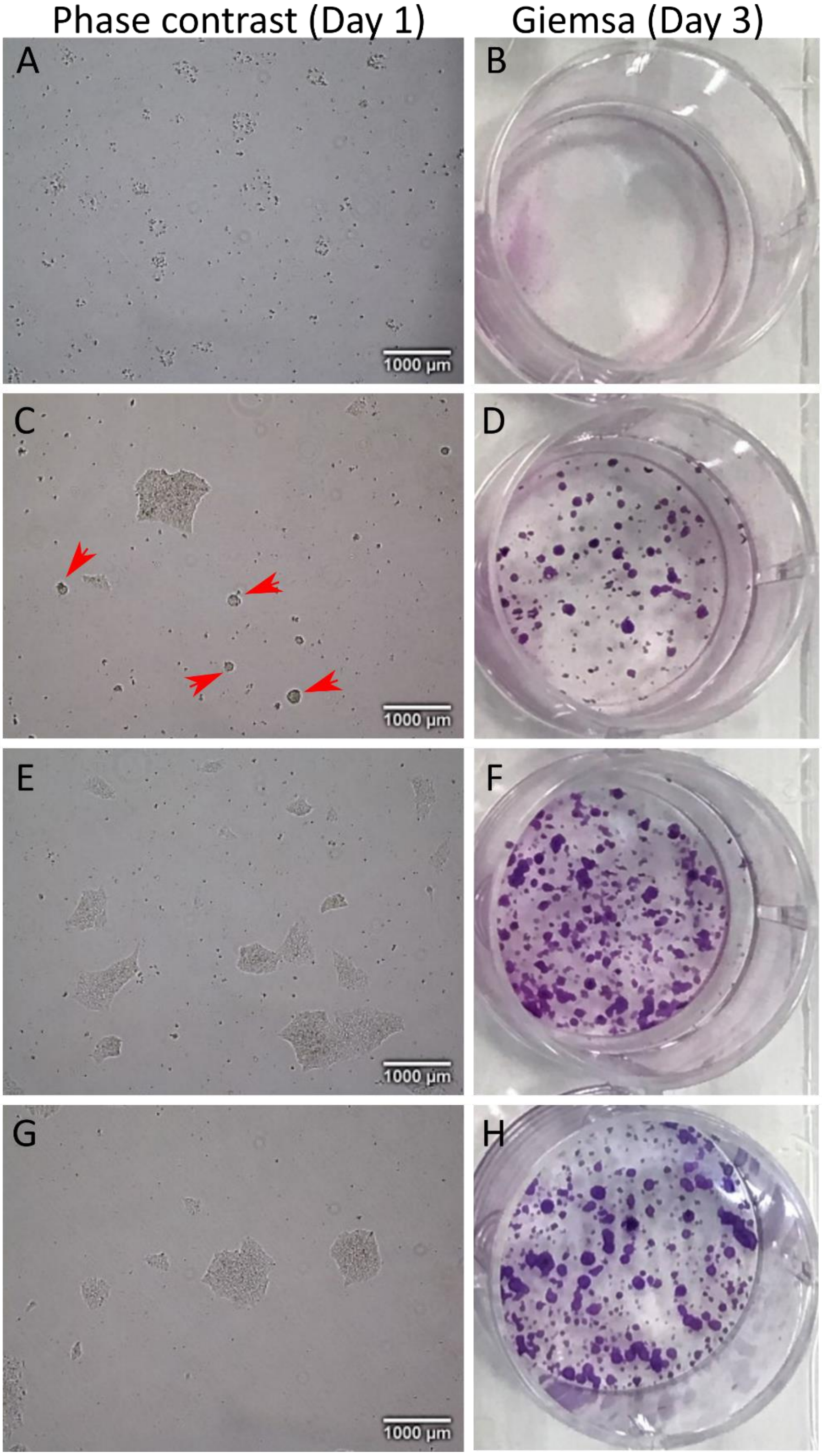

Figure 39. Attachment of RC9 hESC on CaF_2 discs
Growth of hESC on CaF2 discs (A-F) with no coating (A-B), vitronectin alone (C-D), vitronectin and poly-l-lysine (E-F); compared to vitronectin coated tissue culture treated plastic (G-H). Left panels show phase contrast of cells 1 day after passaging. Red arrows indicate poorly adhered colonies. Right panels show cells stained with Giemsa 3 days after passaging. Scalebars are 1 mm.

6.5 Alkalinisation of vesicular pH within live cells in response to V-ATPase inhibitor BafA1 can be detected using MBA-AuNP sensors

The results from section 6.3 suggested that MBA-AuNP accumulating in the perinuclear region of RC9 cells show close association with the lysosomal marker LAMP-1. To test the capability of the MBA-AuNP sensor to detect pH changes in these regions within live cells, a pilot study using Bafilomycin A1 (BafA1) was performed. BafA1 is a macrolide antibiotic and a potent inhibitor of V-ATPase, thereby increasing lysosomal pH and inhibiting autophagy [93,94].

In addition to BafA1 another compound, Clioquinol (ClioQ), was tested. ClioQ is a zinc ionophore which has been suggested to decrease lysosomal pH [95,96]. This compound was used to test if any additional acidification of the lysosomes could be detected. Both BafA1 and ClioQ were incubated with the cells for 1 hour before measurements were taken.

The experimental setup for intracellular SERS is shown in Figure 40. CaF_2 discs with cells grown in 12-well plates were transferred to a 35mm Petri-dish containing 3 mL of room temperature KnockOut™ DMEM. The KnockOut™ DMEM was supplemented with corresponding concentration of either BafA1 or ClioQ. The cells were imaged using a 60x immersion objective. Representative images of a cell in brightfield and darkfield can be seen in Figure 41, A and B respectively. Since the MBA-AuNP are reflective, scattering from out of focus light makes visualisation of clusters possible using darkfield. For SERS measurements the laser was focused on the bright perinuclear regions, and individual spectra were acquired manually for at least 64 different regions per sample.

Figure 42 shows the quantification of all acquired spectra. Mean pH values (shown in red) show no significant difference between cells treated with DMSO control compared to ClioQ, with a pH of 4.31 and 4.49 respectively. As expected, the pH increased significantly to pH 7 for cells treated with BafA1.

Together, these data show that alkalisation of vesicular pH by BafA1 can be detected successfully by SERS. No sign of decrease in pH was detected for ClioQ but longer incubation times may have been required. In interest of time ClioQ was not investigated further.

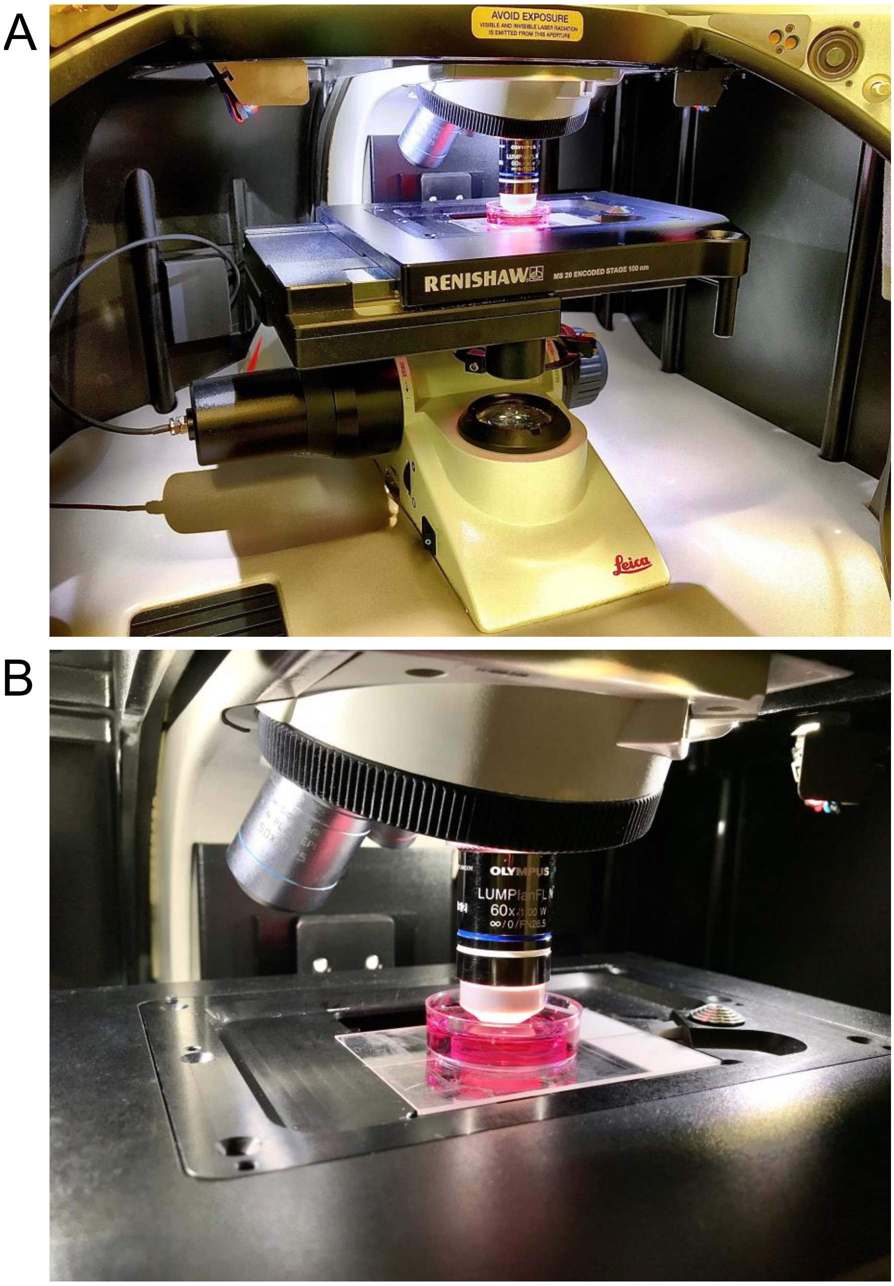

Figure 40. Experimental setup
Photographs of the microscopy chamber of the Renishaw InVia upright configuration with an Olympus LUMPlanFL 60x NA1.0 water-immersion lens and 35 mm Petri dish with cells growing on a CaF_2 disc.

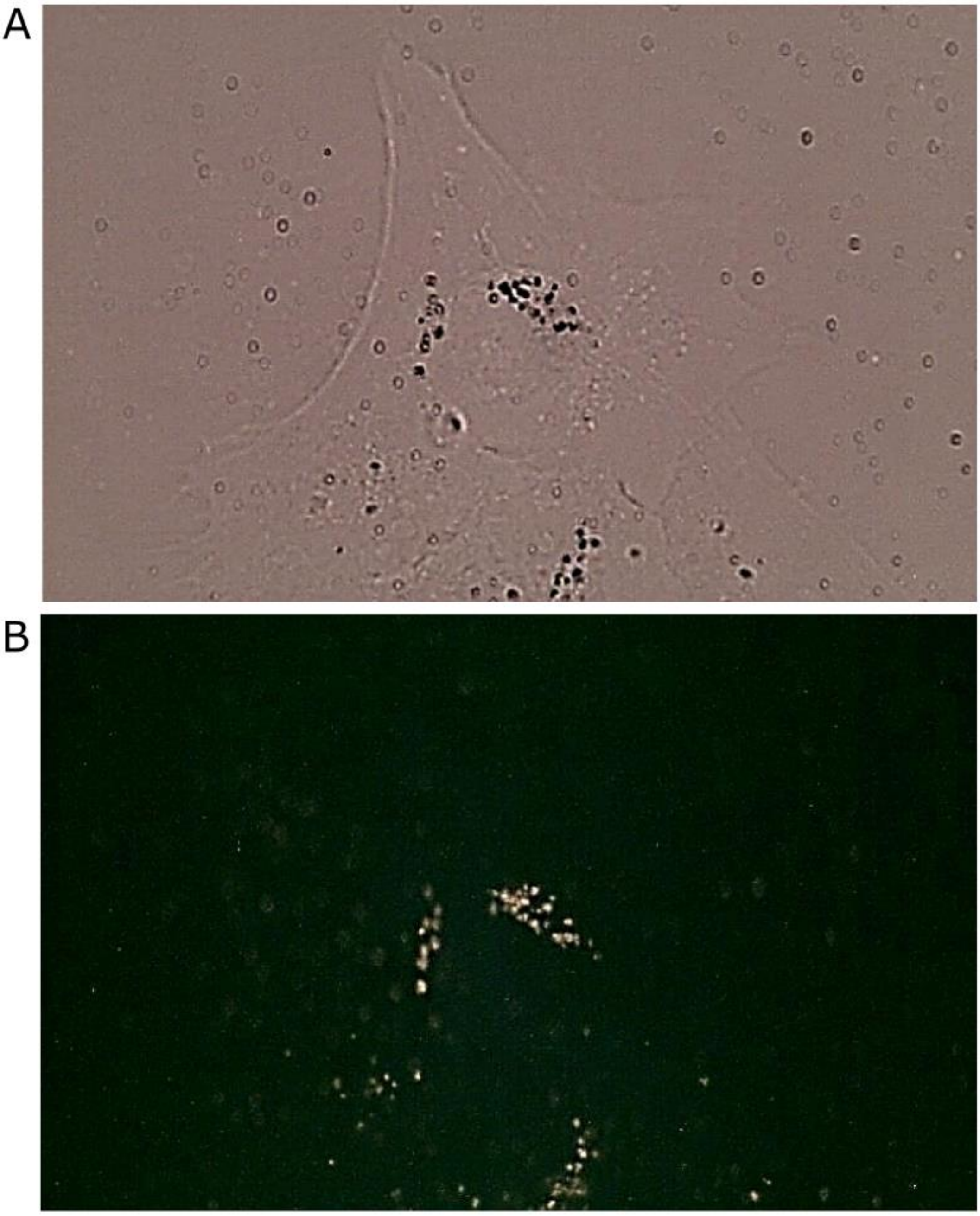

Figure 41. Visualisation of MBA-AuNP within cells in brightfield and darkfield
Example image of brightfield (A) and matching darkfield (B) images from the Renishaw InVia system. Dark intracellular spots in brightfield can be identified as nanoparticles (bright spots) in the matching darkfield image.

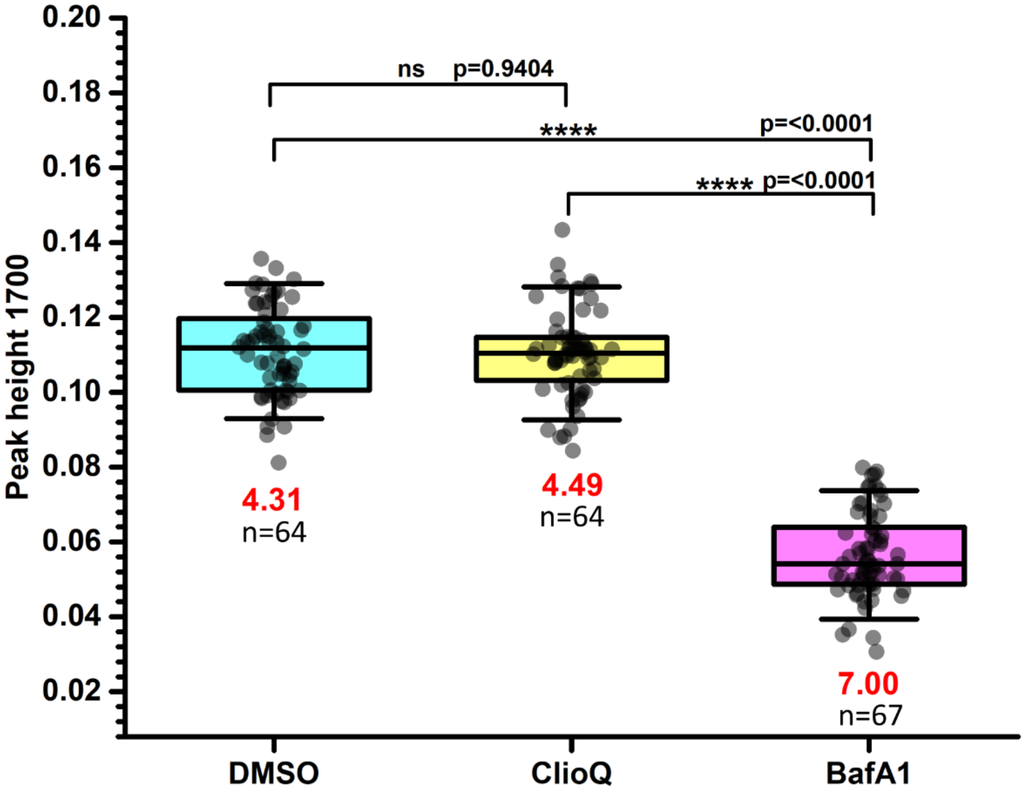

Figure 42. Surface-Enhanced Raman microscopy of MBA-AuNP can detect Bafilomycin-A1-induced changes in RC9 hESC intracellular pH

1700 peak heights for MBA-AuNP spectra measured in RC9 hESC cells incubated for 1 hour with BafA1 (200 nM), ClioQ (250 nM), and DMSO (vehicle). Box & whisker plots show the 25-75th percentile, midline represent the median, and error bars represent SD. Mean pH values, obtained from calibration curve, are shown in red below each box & whisker plot. Dots, overlaid on box & whisker plots, show peak heights of individual spectra.

P-values: ns > 0.05, * < 0.05, ** < 0.01, *** < 0.001, **** < 0.0001, one-way-ANOVA with Tukey post-hoc test.

6.6 BafA1, but not MBA-AuNP affect proliferation of hESC

Previous studies have indicated that lysosomal disruption of stem cells inhibit their ability to differentiate into different germ layers [97,98]. One of the main indicators of proper lysosomal function is the luminal pH. Therefore, the ability to measure pH within stem cells during differentiation might elucidate biological roles and mechanisms in which pH plays a significant part and may aid in improving the efficacy of culture and differentiation of these cells.

In a study performed by Young *et al.* the link between endodermal differentiation and lysosomal function was investigated by disrupting the lysosomal function with BafA1 [97]. They found that when cells were treated with a chronic low dose of 2.5 nM BafA1 during differentiation it led to a significant downregulation of endodermal markers as measured by real-time qPCR (RT-qPCR). However, this was not further linked to a change in pH within the cells. We therefore wanted to investigate whether we could detect differences in lysosomal pH during the differentiation process of hESC treated with BafA1 using MBA-AuNP and SERS.

Initially, to assess a suitable concentration, and the effect this concentration had on cell growth, a proliferation assay was performed. Cells were grown for 1h, 24h, 48h, and 72h in the presence of BafA1 at a concentration of 2nM, 20nM, and 200nM. At each timepoint, cells were fixed then stained using Hoechst dye, and images were recorded.

For analysis and quantification of cell nuclei, the images were exported into Volocity, and an object detection protocol applied as described in section 4.5.3.2. Example images of cells are shown in Figure 43. At timepoint 1 the density of the cells is very similar between the different treatments, but there is a marked decrease in visible nuclei for cells treated with 20nM and 200nM BafA1 after 24 hours onwards. No clear visual difference was observed between all other treatments.

Figure 44 show the quantified results from all acquired images of cells treated with various concentrations of BafA1. There was a clear decrease in the nuclear count after 24 hours in the cells treated with 20nM and 200nM BafA1, a slight decrease was observed for cells treated with 2nM when compared to the control. This was true for both cells treated with BafA1 alone, and co-treated with MBA-AuNP, showing that MBA-AuNP does not have a protective effect against BafA1 (Figure 44A and B respectively).

The effect on proliferation by MBA-AuNP alone was also assessed (Figure 45). No difference in proliferation was detected compared to solvent control, further validating that any differences seen in Figure 44 are due to BafA1 alone, and not the addition of MBA-AuNP.

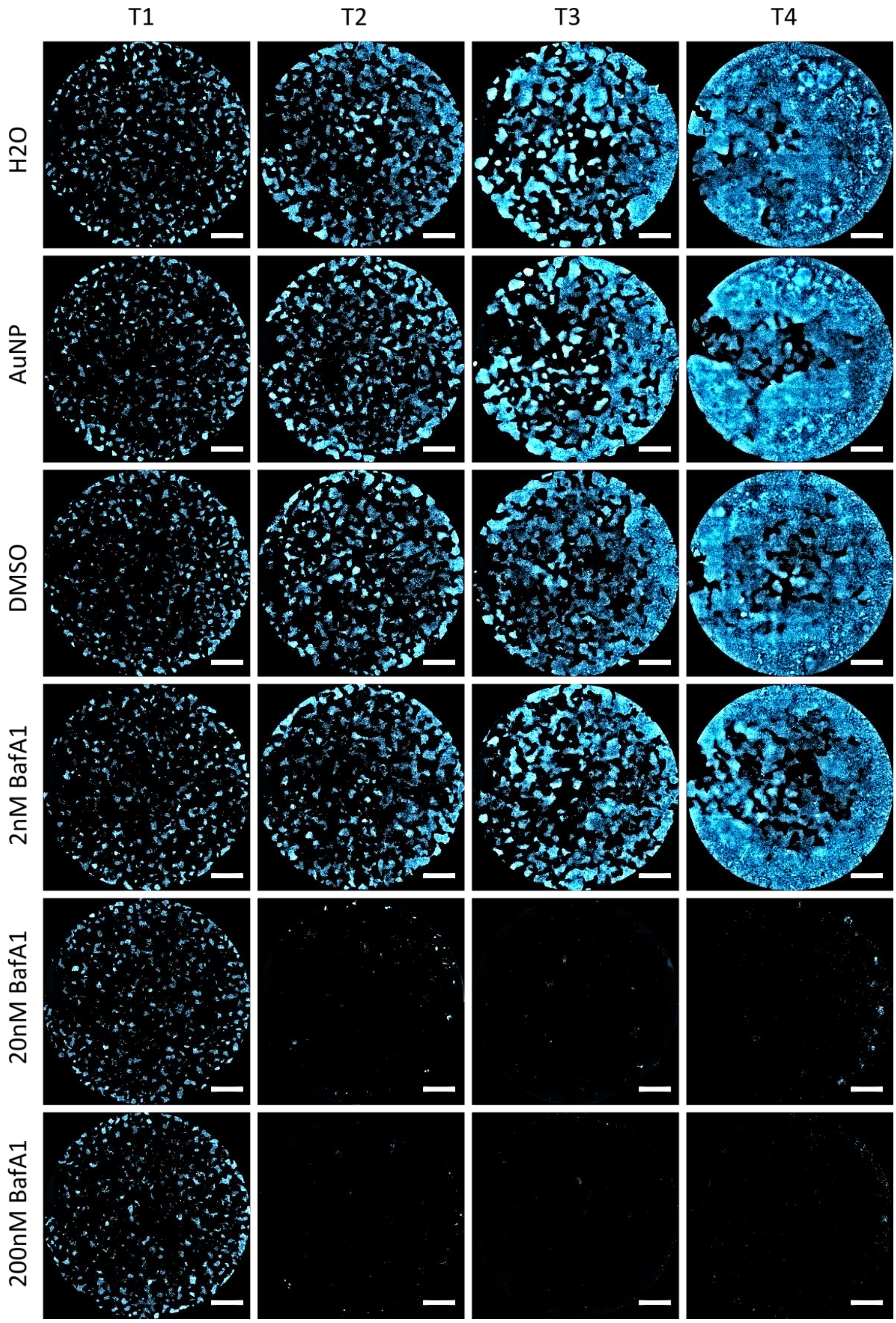

Figure 43. 96-well cell fluorescence-microscopy proliferation assay
Representative images of RC9 hESC cultures pre-incubated with (top to bottom panels): H_2O for 24h; AuNP for 24h; DMSO for 1h; 2 nM BafA1 for 1h; 20 nM BafA1 for 1h; 200 nM BafA1 for 1h before fixation, staining with Hoechst dye, and whole-well imaging at timepoint T1 using a Zeiss Observer 7 microscope and 20x NA 0.75 air objective. Timepoint T2 is a repeated experiment at +24h, followed by +48h (T3), and +72h (T4). Scalebar = 1 mm.

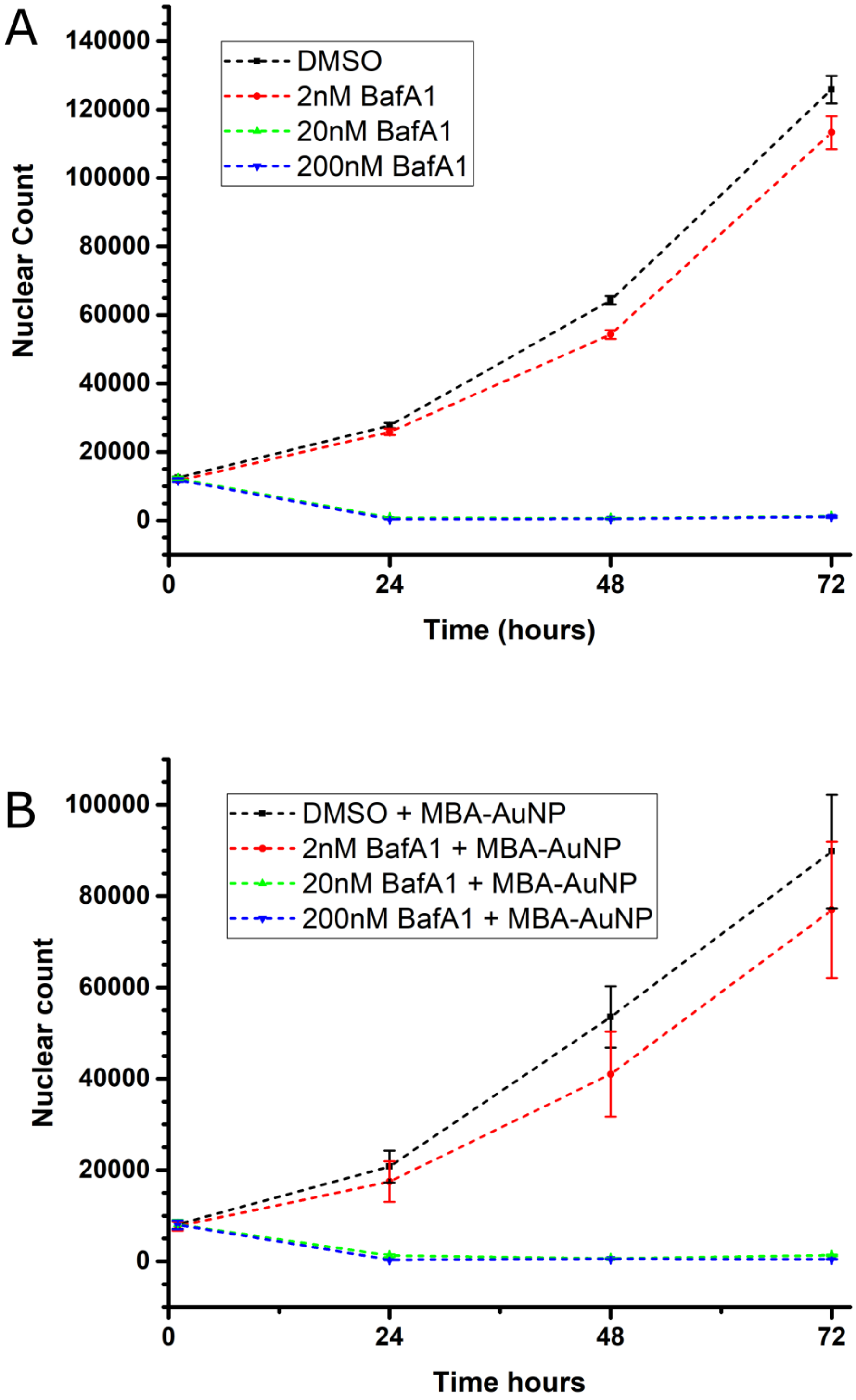

Figure 44. Quantification of detected nuclei in 96-well fluorescence-microscopy proliferation assay: BafA1 treatment

Nuclear counts for BafA1 and vehicle treatment groups at time points T1 (0h), T2 (+24h), T3 (+48h), and T4 (+72h). (A) shows treatment with BafA1 alone. (B) shows co-treatment with BafA1 and MBA-AuNP. Points represent the mean and error bars show standard error (n = 6 for each timepoint).

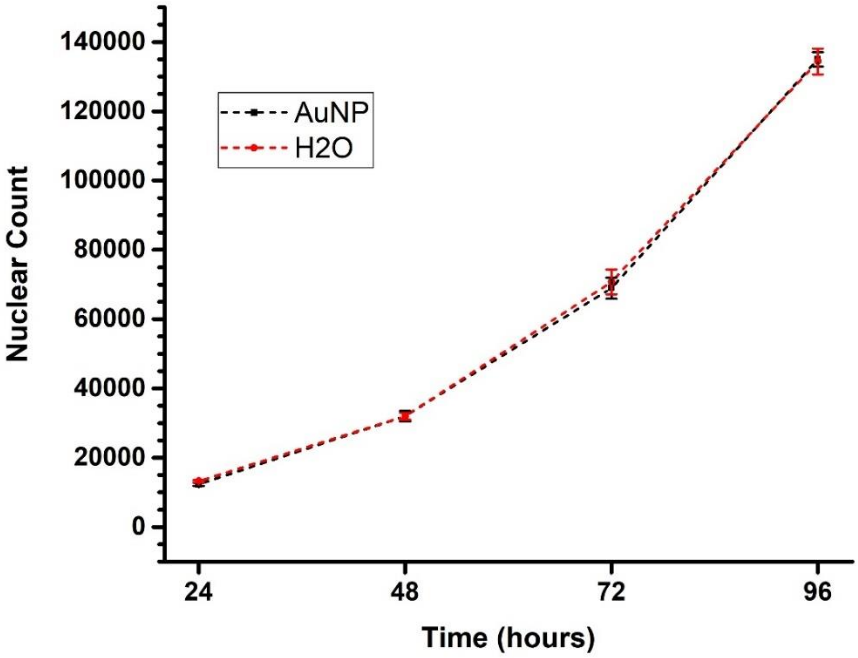

Figure 45. Quantification of detected nuclei in 96-well cell fluorescence-microscopy proliferation assay: MBA-AuNP treatment

Nuclear counts for MBA-AuNP and vehicle treatment 24h, 48h, 72h, and 96h after addition of AuNP and H_2O. Points represent the mean and error bars show standard error (n = 6 for each timepoint).

6.7 MBA-AuNP can detect temporal and concentration dependent changes in pH induced by BafA1

In addition to testing the effect of BafA1 on proliferation of the cells, the intra-lysosomal pH response was assessed using Raman spectroscopy to determine a suitable concentration exhibiting a physiological effect on lysosomal pH while maintaining good cell viability.

In contrast to cells grown in 96-well tissue culture plates for the experiments carried out in section 6.6, an adequate number of cells grown on CaF_2 survived 20nM BafA1 treatment which enabled acquisition of Raman spectra up until 48 hours. At 72 hours a vast number of cells started to die off and it was difficult to find live colonies to acquire spectra from. Therefore, the number of spectra at this timepoint is fewer than all other timepoints.

Figure 46 show averages of all spectra that were collected for each timepoint and treatment group. As explained in chapter 1, the higher the normalised counts of the peak at 1700 cm^{-1}, the more acidic the pH is. Treatments of 20nM BafA1 show the lowest averaged counts at all timepoints, compared to 2nM and vehicle control, hence have the most alkaline pH, as expected. For 2nM BafA1 the averaged counts are slightly lower than DMSO at 1 hour, higher than DMSO at 24 hours and lower at both 48 hours and 72 hours.

The data were quantified, and statistical examination was performed (Figure 47). All collected spectra can be seen as points overlaid on the box plots. Averaged pH values for all treatments are shown in red below each box plot. There is a significant difference in pH at all timepoints between the DMSO control and 20nM BafA1, with BafA1 showing lower counts, and higher pH values. No significant difference was observed between the 2nM BafA1 treatment and DMSO control until 72 hours of treatment. No significant difference in pH was seen between any timepoint for the vehicle controls, indicating that MBA-AuNP themselves do not negatively affect intra-lysosomal pH over time.

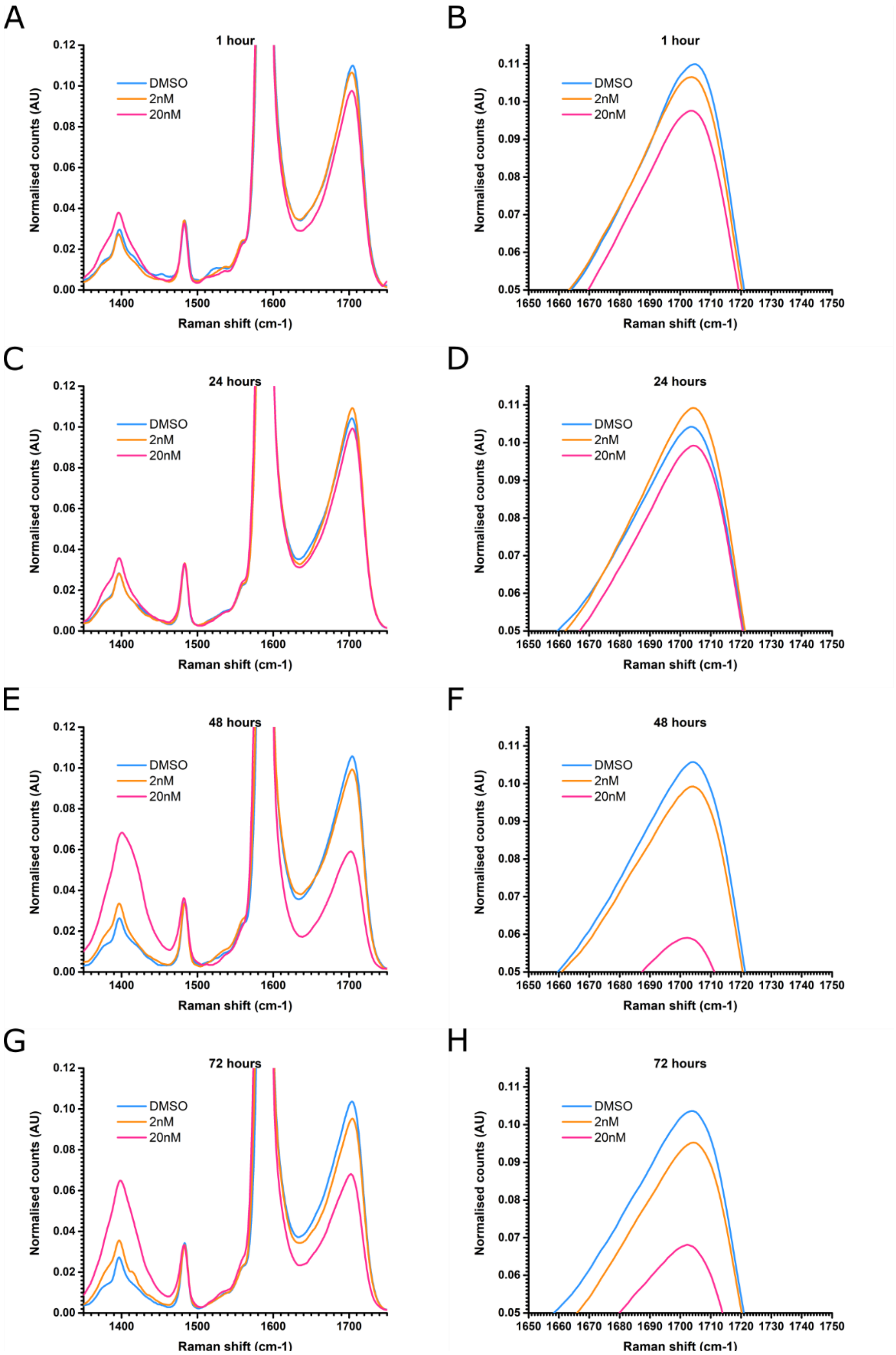

Figure 46. Averaged Raman spectra of BafA1-timepoint-treated RC9 hESC cells
Averaged Raman spectra of RC9 hESC cells treated with DMSO or BafA1 for 1h (A, B), 24hr (C, D), 48h (E, F) and 72h (G, H). Spectra represent an average of all spectra collected for each treatment group (DMSO, 2 nM BafA1, and 20 nM BafA1) over three repeats. (A, C, E, G) full range spectra. (B, D, F ,H) Uppermost part of 1700 peak.

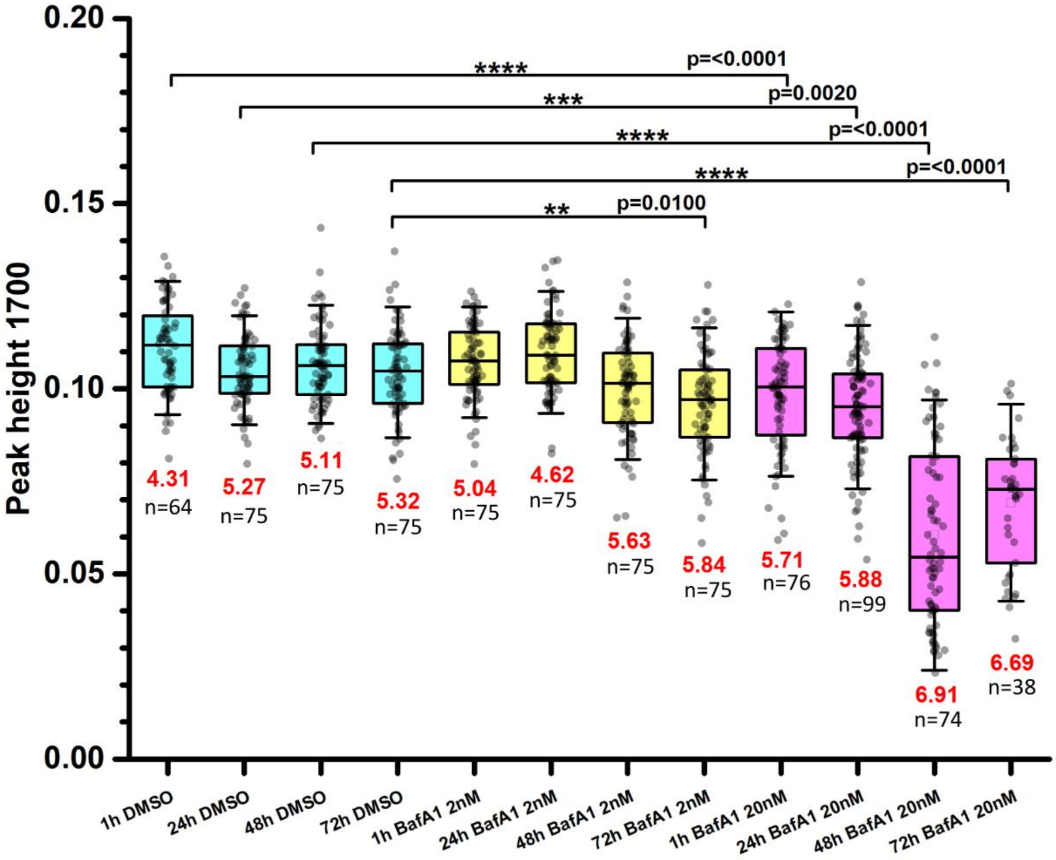

Figure 47. 1700-peak height time course for BafA1-treated RC9 hESC cells

1700-peak heights for MBA-AuNP spectra measured in RC9 hESC cells incubated with DMSO control or BafA1 (2 nM and 20 nM) for 1h, 24h, 48h, and 72h. Box & whisker plots show the 25-75th percentile, midline represent the median, and error bars represent SD. Mean pH values, obtained from calibration curve, are shown in red below each box & whisker plot. The number of spectra collected are shown as 'n =' below each averaged pH value. Dots, overlaid on box & whisker plots, show peak heights of individual spectra.

P-values: ns > 0.05, * < 0.05, ** < 0.01, *** < 0.001, **** < 0.0001, one-way-ANOVA with Tukey post-hoc test.

6.8 Discussion

The experiments in this chapter have shown that hESC can successfully be grown on CaF_2 discs coated with poly-l-lysine and vitronectin allowing quality Raman imaging with high signal to noise ratio to be performed.

Using live-cell timelapse phase and brightfield microscopy, we have elucidated dynamic cellular mechanisms by which MBA-AuNP are incorporated into cells; a process which, by definition, cannot be documented by methods that use fixed cells, such as electron microscopy.

The association of the MBA-AuNP with lysosomal markers LAMP-1 and LAMP-2 were assessed using fluorescent confocal imaging. Both LAMP-1 and LAMP-2 are thought to share common functions *in vivo*, since mice with either LAMP-1 or LAMP-2 single deficiency still present as viable and fertile, whereas double deficiency leads to embryonic lethality [92]. Furthermore, in LAMP-1 single deficient mice there was an upregulation in LAMP-2 and lysosomal properties remained intact [99]. Despite this evidence of a common functionality, LAMP-1 single deficient mice showed a much milder phenotype than LAMP-2 single deficiency. Conversely, LAMP-2 single deficiency mice showed a much higher mortality rate at roughly 50% by postnatal day 20-40 [100]. In humans, LAMP-2 deficiency presents as Danon disease [101]. All this suggests that LAMP-2 has a more specific function than LAMP-1. In our experiments we have shown that after cellular uptake, MBA-AuNP accumulate perinuclearly and associate with LAMP-1. Interestingly, LAMP-2 which as mentioned above has been suggested previously to display similar localisation and function to LAMP-1 [92], did not regularly localise closely with MBA-AuNP. In addition, the staining pattern of LAMP-2 differs from that of LAMP-1, which had denser staining patterns and greater perinuclear clustering. Since the same secondary antibody was used for both LAMP-1 and LAMP-2 this difference can be solely attributed to the difference in primary antibody binding. These are in agreement with previous findings in the literature which suggest that LAMP-1 and LAMP-2 may be differentially expressed in certain tissues and exhibit both independent and similar functions [102]. In the future, co-staining of both LAMP-1 and LAMP-2 could be carried out to investigate the colocalisation and distribution of LAMP-1 and LAMP-2 in various hESC lines. For this study the LAMP-1 results alone were sufficient to confirm an association of MBA-AuNP with lysosomes. Since LAMP-1 and LAMP-2 are both considered well-established markers for lysosomes, both have been used in the literature interchangeably as identifiers of lysosomes in general [97,98]. Our results, together with findings in the literature, suggests that there are differences between the expression of LAMP-1 and LAMP-2 and that they may delineate subset populations of lysosomes with varying functions. Their expression may also be cell line and tissue dependent, which is an important consideration in the decision of which one to use in studies as it may impact the resulting data greatly.

We have also demonstrated, by acquiring Raman spectra from MBA-AuNP which accumulated perinuclearly within cells, that changes in lysosomal pH caused by BafA1 can be detected using our MBA-AuNPs and SERS, confirming the utility of MBA-AuNP in studies observing physiological pH changes in sub-cellular compartments in live cells. Concentration and temporal assessment of BafA1 also revealed that a concentration of 2nM BafA1 is able to cause a significant decrease in lysosomal pH after 72 hours of incubation. All cells die after 24h with 200nM and most cells die after 48h-72h with 20nM. If BafA1 was to be used to investigate the effects of pH changes on differentiation of hESC, a concentration of 2nM would be the most amenable concentration of those tested. Moreover, this concentration was similar to what has been used previously in the literature [97].

The data presented in this chapter support the view that MBA-AuNP is trafficked within the endolysosomal pathways, and that it is possible to obtain pH measurements within these compartments using SERS nanosensors.

7 Functional application of MBA-AuNP in a lysosomal storage disease model (Batten disease)

7.1 Introduction

Gold nanoparticles have been shown both in literature and from the experiments outlined in chapter 2 to accumulate in lysosomes following their cellular uptake [103]. Results from chapter 2 also showed that pH measurement from MBA-AuNP within these endoslysosomal vesicles were possible within hESC.

We wanted to assess if it was possible to utilise this intrinsic accumulation to investigate the intracellular pH within the context of lysosomal storage diseases. For this purpose, primary cell lines, consisting of heterogeneous populations of cells isolated from the subventricular zone (SVZ) of sheep, were sourced from Dr Tom Burdon's lab, at the Roslin Institute. The SVZ of the brain contains a large variety of neural progenitor cell types and is one of two sites that still displays neurogenesis in the adult brain [104]. In total, 6 primary sheep cell lines: two from wild-type sheep, two from heterozygous knockout, and two from homozygous knockouts of the CLN3 gene, known to cause Juvenile Batten Disease, were sourced. See section 4.1.2.2 for more information regarding the cell lines and their derivation.

Batten disease refers to a range of autosomal recessive lysosomal storage diseases caused by the mutation in any 1 of 13 genes [105]. Despite being a fairly rare condition, with an estimated occurrence of 1 in 12,500 live births in certain populations or 1 in 100,000 worldwide, Batten disease is the most common paediatric neurodegenerative disease [105,106]. Phenotypic signs of the disease include impairment and progressive loss of vision, seizures, decline in mental, cognitive, and motor functions; and ultimately premature death [105,106]. Until recently the function of the proteins and pathways that are involved in the disease progression had only been partially understood; however, thanks to an extensive arsenal of well-characterised models this is starting to change [105].

This chapter outlines how MBA-AuNP and SERS can be utilised to detect differences in pH within lysosomal vesicles in Batten disease, and also validate the newly isolated primary SVZ cells isolated from sheep. This model could ultimately aid in the determination of cellular response in lysosomal pH to disease treatments.

7.2 Serum starvation increases MBA-AuNP uptake

Initial attempts to perform SERS on MBA-AuNP within the sheep SVZ cells was largely unsuccessful, as bright regions of nanoparticles; those with visible dense accumulation of MBA-AuNP, were hard to locate and an acceptable signal was difficult to obtain both by using the same settings as had been previously used for SERS within hESC and by increasing laser power and/or acquisition time. Previous studies have shown that the presence of serum within the cell culture medium can negatively affect the uptake of gold nanoparticles within cells [37]. Considering this, serum deprivation was tested to see if it could increase the uptake of MBA-AuNP into the cells and thereby facilitate reliable SERS measurements with clear signal to noise ratio and a high number of usable spectra. Images were acquired on the Renishaw InVia microscope and, as shown in Figure 48, culturing the cells with MBA-AuNP in serum-free medium for 24 hours led to a notable increase in the number of nanoparticles and, importantly, MBA-AuNP accumulations, within the cells compared to medium containing 10% FBS. In addition, more particles were seen in the matrix surrounding the cells in the serum-free condition, similarly to what was seen when culturing hESC. The increased uptake and accumulation of MBA-AuNP made it possible to obtain more intense SERS spectra, and it was therefore decided to adopt this protocol for further experiments.

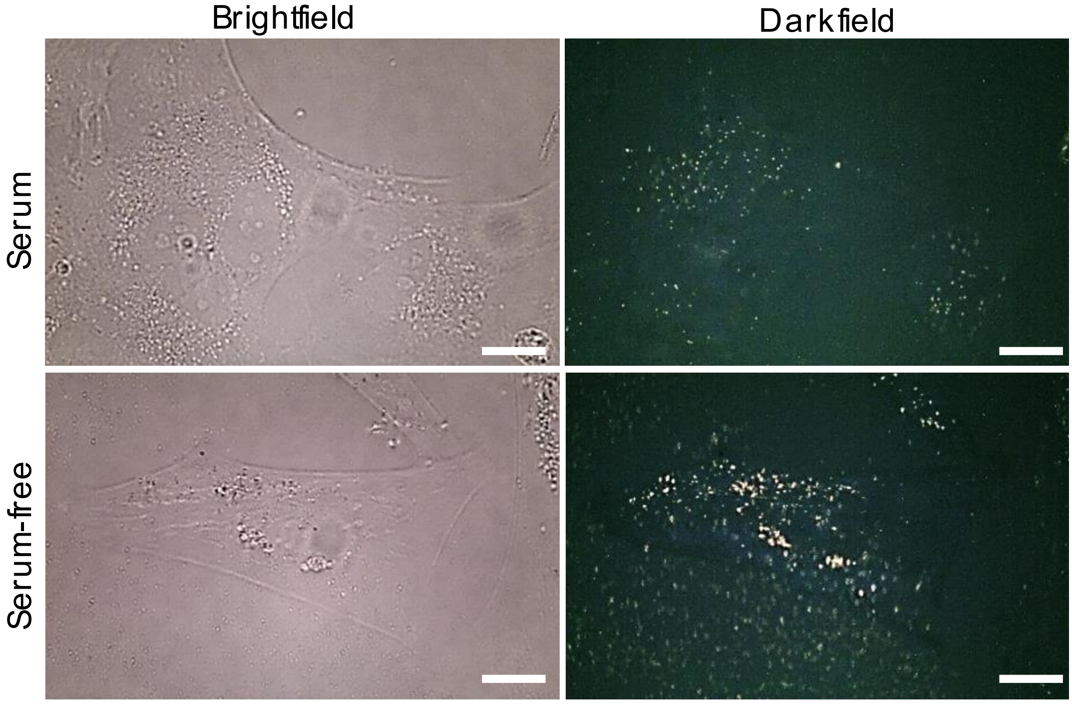

Figure 48. Uptake of MBA-AuNP is affected by serum in media
The uptake of MBA-AuNPs is greatly influenced by the presence of FBS in the media. Figure shows brightfield and darkfield images of sheep SVZ cells incubated for 24 hours in FBS containing (A) or serum-free (B) cell culture medium. Scalebar = 20µm.

7.3 CLN3 KO SVZ cells have higher intralysosomal pH than HET and WT in Batten disease model

Sheep SVZ cell lines were seeded onto one side of CaF_2 discs at a density of $2x10^4$ cells/ well in a 12 well plate as described in section 4.1.2.2 and 4.3.3. After 24 hours of MBA-AuNP incubation in serum-free medium the cells were washed 3x in PBS and fresh serum-free medium was added to each well. The cells were transported to the Renishaw InVia microscope and kept in a heated incubator with 5% CO_2 and passively humidified air until imaging. To make imaging more manageable the six primary sheep SVZ cell lines were divided into two sets, each containing one wildtype (WT), heterozygote (HET), and knockout (KO) cell line. Cell lines within a single set were always imaged on the same day to ensure consistency, and each experiment was repeated at least three times on different days. Figure 49 shows the averaged Raman spectra of the sheep SVZ cells. In both sets, the KO cell lines had consistently lower 1700 nm peak counts than the WT and HET cell lines, which themselves remained largely the same as each other. This means that the pH of KO cells is more alkaline than WT and HET cells, as the 1700 nm peak count increases when pH decreases, which is in agreement with previous reports [107,108].

Figure 50 displays the quantification of the same data shown in Figure 49. Each dot on the histograms represents the individual peak height of the 1700 nm peak of each Raman spectrum collected. Since the data followed a normal distribution, an ordinary one-way ANOVA was performed to establish whether there was a significant difference between the samples. For set 1 no significant difference was seen between either genotype (Figure 50, B). When sets 1 and 2 were grouped together, and for set 2 on its own, the KO genotypes were significantly more alkaline (lower counts) than the WT and HET genotypes (Figure 50, A, C respectively). No significant difference was detected between WT and HET genotypes when looking at either the sets in isolation or grouped.

As a result of the range of peak heights seen within any one genotype, and since some of the peak heights lie in the extremity of, or outwith the calibration curve range, assigning a value of pH to each individual peak was not always possible. For clarity, and to demonstrate not only the validity, but also the limitations, of the MBA-AuNP range as a sensor, the individual peak data were converted to pH values using the calibration curve outlined in chapter 5 and plotted alongside the percentage of spectra able to be converted into pH (Figure 51). As can be seen, more than 90% of the collected spectra were able to be converted into pH values for all genotypes.

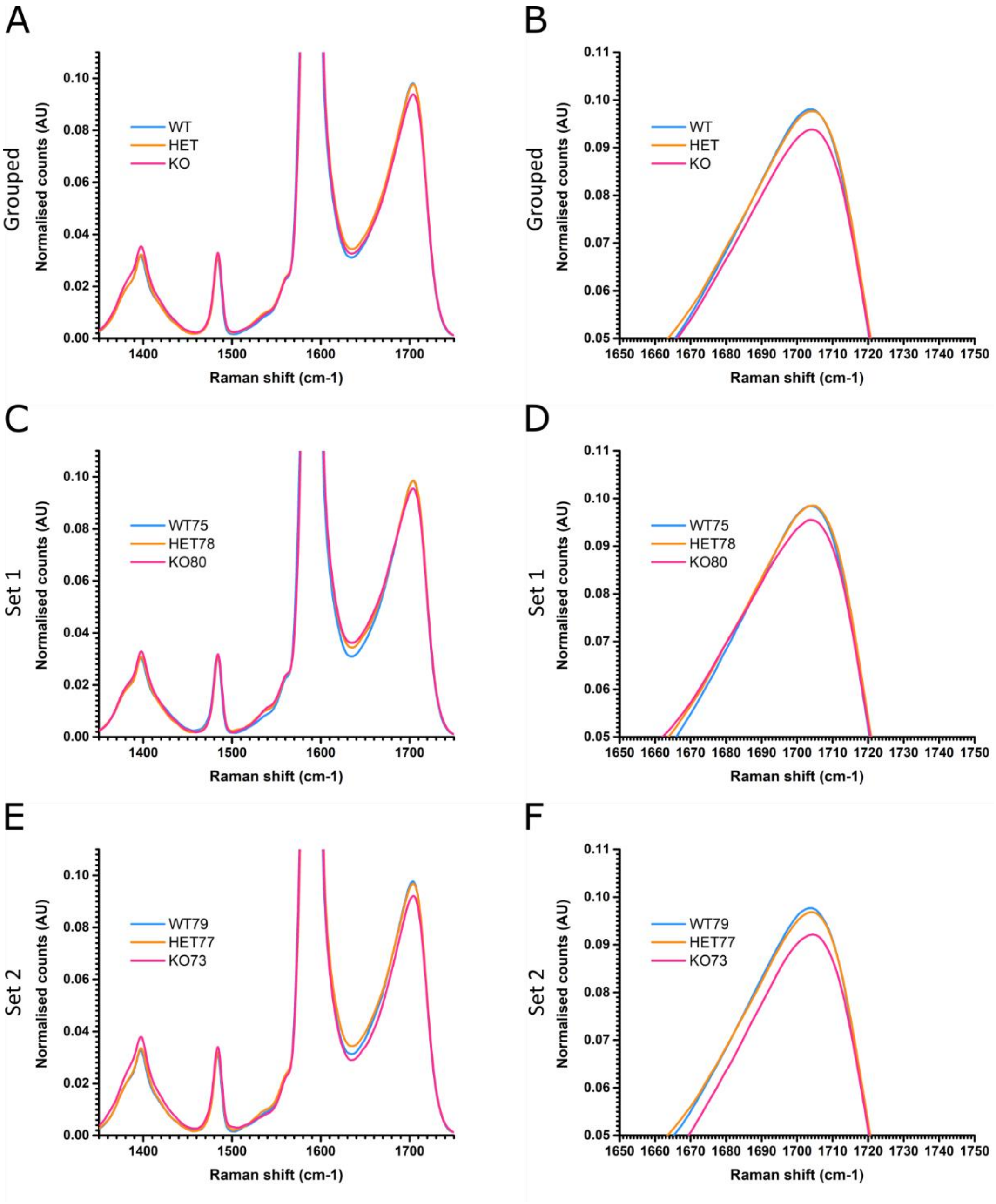

Figure 49. Averaged Raman spectra of Sheep SVZ cells

Averaged Raman spectra of sheep SVZ cells from wildtype, heterozygous knockouts, and full knockouts of the CLN3 gene. Experiments were carried out on primary cell cultures isolated from 2 sheep of each genotype. The 6 cell lines were divided into sets of 2 (set 1 = WT75, HET78 and KO80, and set 2 = WT79, HET77 and KO73) which were assessed together in 3 technical repeats for each set (n =3 for set 1 and n = 3 for set 2). Spectra represent an average of all spectra collected for each genotype (n = 75 over three repeats). (A-B) both sets grouped by genotype. (C-D) Spectra for set 1. (E-F) spectra for set 2. (A, C, E) full range spectra. (B, D, F) Uppermost part of 1700 nm peak.

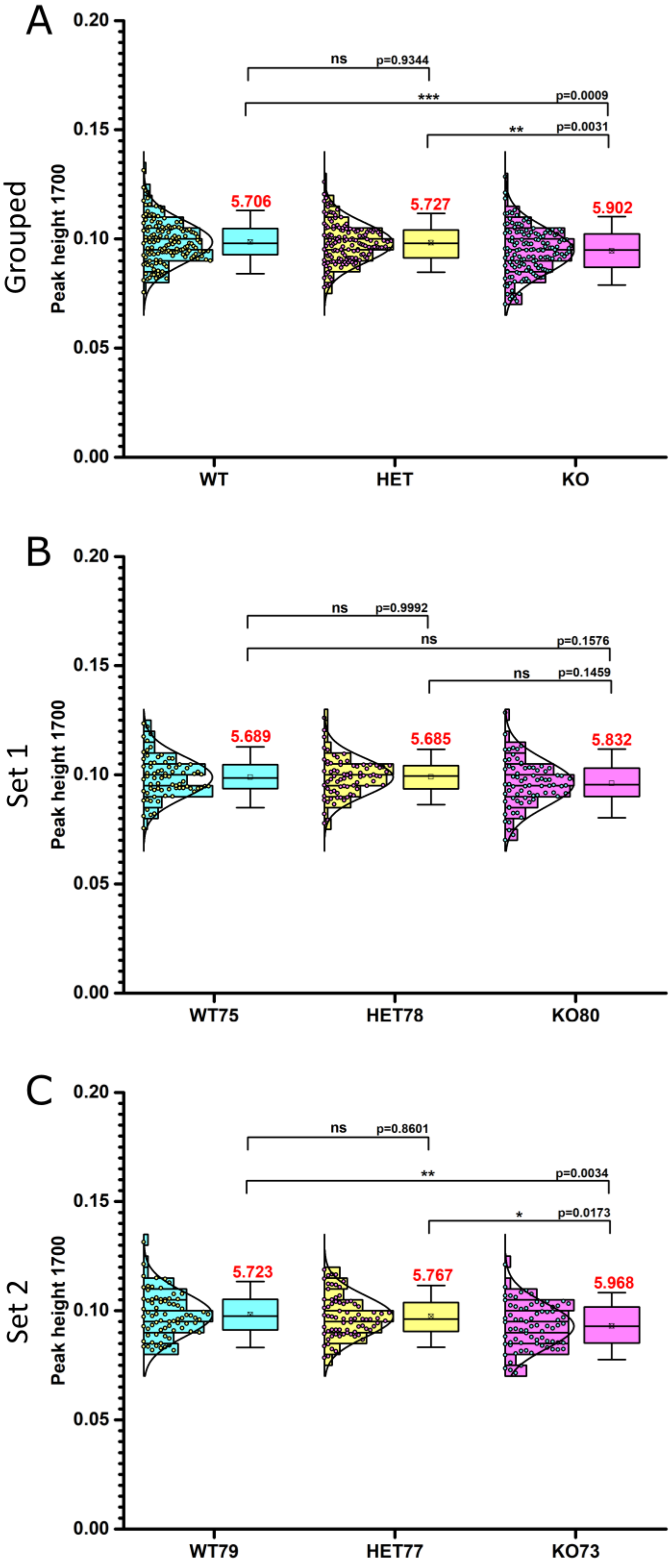

Figure 50. Quantification of peak height of the 1700 peak Quantification of the peak height from the 1700 nm peak. Solid bars show the 25-75th percentile, midline represent the median, and error bars represent the standard deviation. Normal distributions of the data and individual data points are shown to the left of each bar chart. Mean pH values obtained from calibration curve are shown in red above bar charts. (A) both sets grouped together. (B) Set 1 consisting of cell lines WT75, HET78 and KO80. (C) Set 2 consisting of cell lines WT79, HET77 and KO73. P-values: ns > 0.05, * < 0.05, ** < 0.01, *** < 0.001, **** < 0.0001, one-way-ANOVA with Tukey post-hoc test.

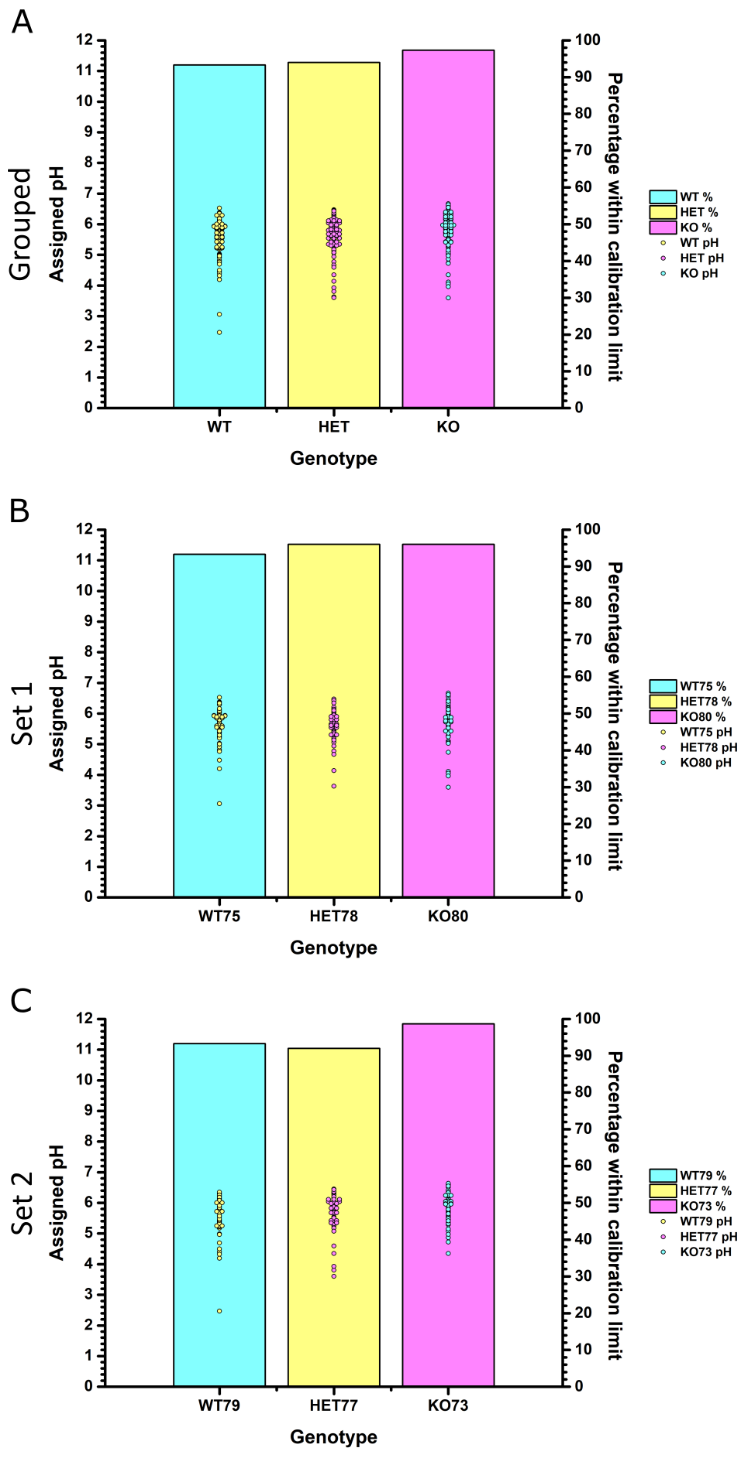

Figure 51. Assigned pH and percentage

Graphic illustration of the pH variation within sheep SVZ cells. Bars represent the percentage of spectra that were within the calibration limit of the sensor, and dots show the pH assigned to each spectrum that were within the calibration limit. (A) both sets grouped together. (B) Set 1 consisting of cell lines WT75, HET78 and KO80. (C) Set 2 consisting of cell lines WT79, HET77 and KO73.

7.4 CLN3 KO SVZ cells have higher autofluorescence than HET or WT in Batten disease model

Tissues from Batten Disease patients are known to have characteristic autofluorescent accumulations [106,109–113]. As a confirmatory assay to further validate and test the sheep SVZ cells as a model for Batten disease we assessed whether there was a detectable difference in autofluorescence between the different genotypes.

7.4.1 Imaging of autofluorescence

Initially, live cells were observed using a Zeiss Observer widefield microscope, but this attempt was unfruitful as the autofluorescence emitted from individual cells was far too low for detection using the standard light source and Axiocam that was fitted to this microscope.

Therefore, in order to detect the weak autofluorescent signal, a high-sensitivity microscope equipped with two emCCD (electron-multiplication charge coupled device) cameras, which allowed very long low-noise exposures and multiple-frame on-chip signal-averaging was employed. The upright configuration of the microscope and silicon oil immersion lens required for high-sensitivity imaging necessitated the fixation of cells before imaging. At least 10 fields were recorded for 2 coverslips per genotype on 2 different occasions. Example images are shown in Figure 52. The autofluorescence of the overlaid blue, red and green channels for WT, HET, and KO can be seen in Figure 52 (A, C and E). For easier visualisation, a pseudocolour LUT of the intensity was also applied (Figure 52; B, D, F). In general, the KO genotype showed a visually higher fluorescent signal compared to the HET and WT genotypes. However, this difference was not always obvious to the naked eye and so the intensities were quantified using specialist image analysis software, Volocity, as discussed in the next section.

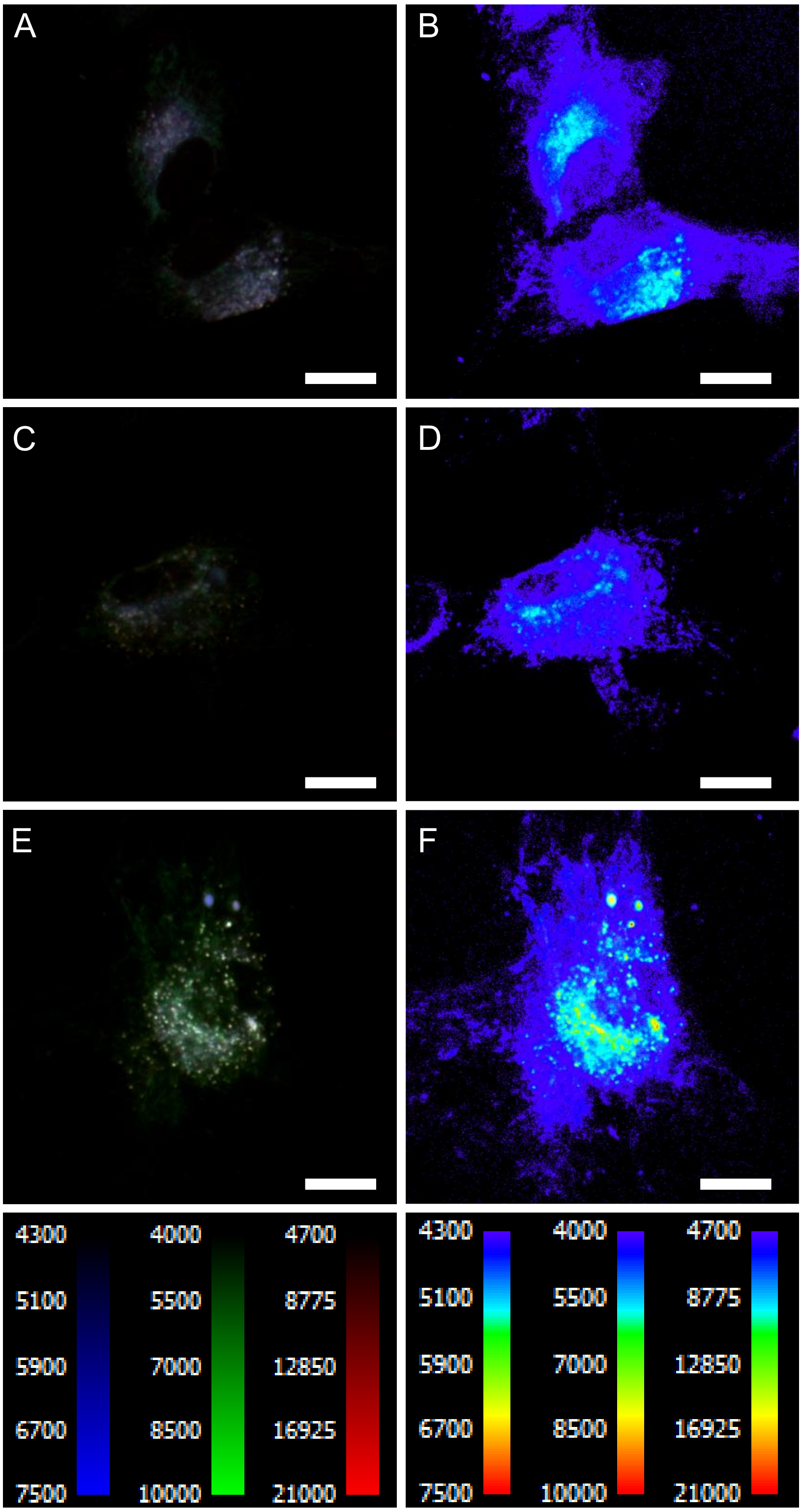

Figure 52. Autofluorescence of battens disease SVZ cells
Example images of multichannel autofluorescence from wildtype (A, B), heterozygote (C, D), and CLN3 knockout sheep SVZ cells (E, F). Autofluorescence mainly comes from vesicle-like structures within the cytoplasm of the cells. Pseudocolour LUTs applied were Blue/Green/Red (A, C, E) and Rainbow (B, D, F). Pseudocolour intensity references are shown below each column.
Scalebar = 20 µm.

7.4.2 Quantification of autofluorescence in Batten disease

To quantify the weak autofluorescent signals obtained in the previous section, an object detection protocol was utilised within Volocity software as described in section 4.5.4.3. Quantified intensities for each channel were plotted as both averages of the blue, green, and red channels or separately (Figure 53). When combining all channels, the autofluorescence of the KO genotype was significantly higher than both WT and HET. No significant difference was observed between the WT and HET genotypes. Splitting all channels reveals that most of this autofluorescence is attributed to the red channel, where there is less overlap between the genotypes. While the same trend exists for the green channel, there is a deviation from the trend in the blue channel, where it appears that the HETs have higher autofluorescence in this spectral range.

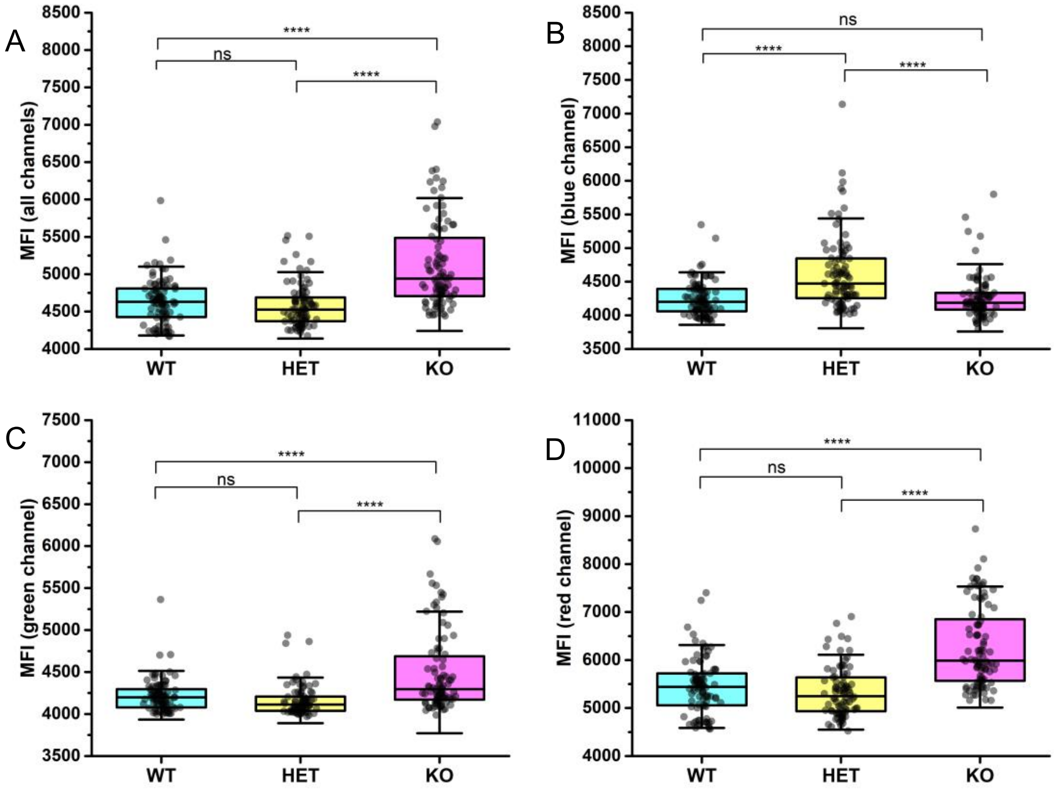

Figure 53. Quantification of autofluorescence

Quantification of autofluorescence in wildtype, heterozygous knockout, and full knockout sheep SVZ cells. (A) Average mean fluorescence intensity (MFI) of all channels, (B) MFI from the blue channel, (C) MFI from the green channel, and (D) MFI from the red channel. Box & whisker plots show the 25-75th percentile, midline represent the median, and error bars represent the standard deviation. Dots are MFI of each individual image (WT n=91, HET n=89, KO n=86). P-values: ns > 0.05, * < 0.05, ** < 0.01, *** < 0.001, **** < 0.0001, one-way-ANOVA with Tukey post-hoc test.

7.5 CLN3 KO SVZ cells have lower levels of PPT1 activity

Another confirmatory assay that has been used to diagnose Batten disease is a fluorometric assay based on the activity of the lysosomal enzyme palmitoyl-protein thioesterase 1 (PPT1) [77]. PPT1 has been confirmed to be deficient in patients with neuronal ceroid lipofuscinoses caused by mutations in the CLN1, CLN2 and CLN3 genes [77,109,114,115].

Protein from primary SVZ cells obtained from wild-type, heterozygote and homozygous knockout sheep were collected as described in section 4.6. The protein was transported to the Roslin Institute, where a PPT1 enzymatic activity assay was carried out by Samantha Eaton according to published protocol [77].

The results obtained from the assay are displayed in Figure 54. Knockout cells show a marked reduction in the PPT1 activity compared to the wild-type cells, whereas the heterozygotes show only a slight reduction. These results are in agreement with what has been reported previously [77].

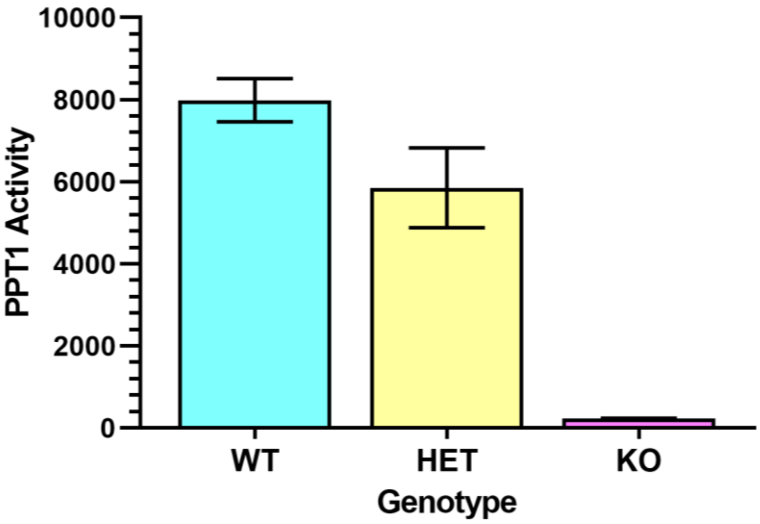

Figure 54. Batten's disease PPT1 enzymatic activity test
PPT1 activity test conducted by Samantha Eaton, Roslin Institute. Enzymatic activity of PPT1 for each genotype group is shown in arbitrary fluorescence units. Bar charts represent the mean with standard deviation bars for n = 2 per genotype group.

7.6 Conclusion

This chapter shows that MBA-AuNP sensors are able to distinguish small changes in pH within cellular vesicles in the context of lysosomal storage disease in sheep SVZ cells, *in vitro*. Although small changes were detectable, there is still a lot of improvements to be made in the design of the sensor. Firstly, the pKa of the MBA-AuNP based on calibration curves in Chapter 1 lie at around pH 7, which means that the most sensitive window lies at between pH 6-8. Small changes outwith this window will therefore be harder to detect, unless a large sample size is collected. By designing a reporter molecule with a pKa of around 5, this aspect could be better tailored to the desired application. Furthermore, the uptake of the MBA-AuNP into the lysosome or other cellular compartments can be difficult to control and relies entirely on the cells innate uptake and internal distribution mechanisms. In this study the culture conditions of the cells had to be altered to increase the uptake of the MBA-AuNP by culturing the cells in serum-free medium. When culturing the cells in serum-free medium, larger aggregates within the cells and more particles in the surrounding matrix were observed compared to when cultured in serum-containing medium. This observation may in part be attributed to the binding of the MBA-AuNP to serum proteins. MBA-AuNP could sometimes be visually detected in protein aggregates within the medium (not shown). These trapped MBA-AuNP would be washed away sequentially during media changes and would not be allowed to settle in the matrix. Furthermore, binding of proteins to the gold surface may protect against aggregation of the particles and may therefore lead to a higher percentage of single MBA-AuNP and smaller aggregates. Although this approach has been reported previously [37] we found that it led to higher intra-lysosomal pH values compared to experiments in chapter 2, which involved the culture of hESC in serum-free conditions as standard. This discrepancy could be due to differences in cell lines, but an increase of lysosomal pH in response to serum starvation has been reported previously [116,117]. This means that although the reported pH values can discriminate differences in pH between diseased and healthy cells, it might not be able to accurately report physiological pH values, unless culture conditions are kept at a physiological optimum. To improve the accuracy of reporting physiological pH values, the efficiency of MBA-AuNP delivery to the SVZ cells could be improved in future studies. Alternatively, cultures could be optimised such that serum-free media which maintain healthy cultures and assist MBA-AuNP uptake are found, but do not cause starvation stress in the growing cells.

As no cell culture chamber was available on the Renishaw InVia microscope, it was not possible to perform long imaging sessions; since there was no temperature, gas, or humidity control. Future experiments may be more informative and unbiased if maps of the cells could be made rather than point spectra at similar regions of interest; however, due to the long acquisition times required to make whole-cell maps, and the fact that lack of environmental control made long-term imaging unviable on this system, it was not possible in this study. Alternatively, but less comprehensive a solution than full environmental control, the addition of HEPES buffer into the medium may also help to prevent pH fluctuations in the medium caused by exposure to air if a chamber is unavailable. A prototype custom cell culture chamber, which could help maintain optimal environmental conditions, was designed, and printed, but due to toxicity of the printing material and time constraints this was not pursued to a full working prototype (data not shown).

The advantage of using MBA-AuNP as a sensor, when compared to fluorescent probes, would be that it is possible to determine the pH from discrete locations – such as individual lysosomes. However, due to the sensitivity of MBA itself, the individual measurements have an inherent range in which readings are most accurate, i.e., pH 6-8, which means that the measurement of more acidic organelles such as lysosomes can be ascertained with less certainty than those within the ideal pKa range of the sensor molecule. To determine the pH of cellular compartments accurately and reliably at the extremes of physiological acidity, it would be necessary to develop a sensor which is optimally sensitive in the 4-6 pH region rather than at pH 6-8. In this study, it was necessary to acquire large sample sizes to achieve statistical power to discriminate slight pH differences. A more optimised pH sensor would require fewer measurements, making acquisition of data faster. Moreover, with an optimised sensor, it may be possible to accurately determine the pH of individual lysosomes with single measurements rather than averaging many spectra from many cells.

Confirmatory assays of the autofluorescence and PPT1 activity within the KO sheep SVZ cells was in agreement with what would be expected in the case of lysosomal storage disease. This suggests that these cells are a good model for Batten disease. Our results showed that one of the main contributors of autofluorescence came from a component that emitted in the red range of the visible light spectrum. In Batten disease, there is an accumulation of autofluorescent storage material called ceroid which are lipofuscin-like pathological lipopigments [105,106,118]. Lipofuscin has been shown previously to be autofluorescent in the red channel, showing up as perinuclear red-fluorescent puncta, which agrees with the results in section 7.4.1 [119].

8 Conclusions

As stated in chapter 3 the aims of the experiments presented within this thesis were to investigate the utility of MBA-AuNP as a pH sensor within live cells using SERS. This involved the assessment of the method of analysis, cellular localisation of the sensor, sensitivity, and ability of the sensor to be applied in a biological context.

As mentioned previously there is no single consensus method within the literature to analyse the Raman spectrum of MBA to acquire pH values. Previously both the maximum peak intensity and area under the curve (AUC) have been utilised. Certain researchers primarily use the pH sensitive peak at 1420 cm^{-1}, the pH peak at 1700 cm^{-1}, or a combination of both [8,42,57,79]. Normalisation has been carried out using either of the pH insensitive peaks at 1080 cm^{-1} and 1590 cm^{-1}. Furthermore, smaller peaks have also been assessed, although since their intensity is relatively low, they are not as useful as the two main pH sensitive peaks already mentioned [43,85]. In this study we chose to compare a peak maximum or AUC method to generate calibration curves. This was done by either normalising the 1420-peak or the 1700-peak to the 1590-peak and plotting the resulting maximum peak intensities or AUC values. By doing this we realised that the maximum peak intensities did not change at a consistent rate for the 1420-peak, which resulted in a higher pK_a of the sensor when using this method compared to all other methods tested. This indicated that it is very important to choose the method of analysis carefully, as the sensitivity of the sensor at certain pH values may be affected if the suboptimal method is chosen. In general, most of the tested methods showed a pK_a of around pH 7, similar to what has been reported previously in the literature [8,42,81]. Many researchers appear to primarily use the 1420-peak rather than the 1700-peak for analysis and calibration curve generation [42,57]. In our hands the 1700-peak showed a much more consistent response to pH and appeared more reliable for pH measurements. One reason why this peak may not be used as frequently is that the intensity is not as strong as the 1420-peak and unless the spectrum has a high signal-to-noise-ratio it may prove difficult to properly calibrate and retrieve pH measurements using it. Since Raman is an inherently weak phenomenon longer acquisition times and/or higher laser powers may be required to achieve these high signal-to-noise ratios, which may not always be desired in a biological context as it may be harmful for the cells. Using our experimental method, the cells appeared to maintain healthy morphology and viability throughout the experimental window; however, it was only possible to achieve good signal-to-noise ratios from clustered particles and not individual particles. The MBA-AuNP were also shown to cause no reduction in cell viability, even at the highest tested concentrations.

Cellular localisation of the nanoparticles within cells is another area where the literature is quite divided. Some researchers report uptake into the cytoplasm, whereas others report uptake into vesicles [37,86–88,120]. This is quite unsurprising as there is a vast range of sizes, shapes, and surface modifications used, all which may impact the uptake routes of the nanoparticles into cells. Determination of the intracellular localisation of nanoparticles is commonly achieved using transmission electron microscopy (TEM) [37,44,121]. However, the downside with TEM is that it needs to be carried out on fixed sectioned cells, is expensive, and requires specialist technical skills [121]. There are some examples of research in which confocal microscopy has been utilised to visualise AuNP uptake either through fluorescent labelling or using their inherent reflective properties [121–124].

We noticed that the MBA-AuNP could be visualised under normal phase contrast microscopy while doing regular cell maintenance and routine imaging. To quickly and inexpensively assess the uptake of the particles we carried out a timelapse acquisition using high magnification phase contrast microscopy. We combined normal brightfield images, in which the particles show up as black dots, with phase contrast images, a method which to our knowledge has never been used before. This allowed clear label free visualisation of the particles using fairly standard microscopy equipment. This method has an advantage over TEM because it allows real-time visualisation of the uptake mechanisms, albeit with lower magnification.

The cellular localisation of the MBA-AuNP was also assessed using laser scanning confocal microscopy by detecting the nanoparticles label-free by collecting scattered laser light using reflection mode and fluorescent staining for the lysosomal markers LAMP-1 and LAMP-2. Within the literature LAMP-1 and LAMP-2 appear to be used quite interchangeably for the labelling of lysosomes [97,98,120]. In our experiments we found that the staining pattern of LAMP-1 and LAMP-2 differed markedly from one another, with LAMP-1 showing dense perinuclear staining with lots of small spots all over the cell, whereas LAMP-2 showed far fewer but brighter spots all over the cells. LAMP-1 was closely associated with MBA-AuNP in the perinuclear regions, whereas LAMP-2 did not follow this pattern. This result suggests that LAMP-1 and LAMP-2 may play different roles within hESC; however, this would need to be investigated further and was beyond the scope of this thesis. We did confirm close association of the MBA-AuNP with LAMP-1 but not LAMP-2, which still suggests that the MBA-AuNP are eventually trafficked into lysosomes. By targeting only particles which accumulate perinuclearly, where most of the LAMP-1 signal and MBA-AuNP clusters reside, there is quite high certainty that the resulting Raman spectra are from within vesicles within the endolysosomal pathway, specifically LAMP-1 positive vesicles. In addition, we confirmed that MBA-AuNP are still found located in these perinuclear LAMP-1 positive regions even after 96 hours after MBA-AuNP addition. This means that it would still be possible to collect SERS spectra even after 96 hours, allowing timelapse experiments to be performed within this time window.

The effect of the particles on cell proliferation and growth was also assessed and showed no negative effect of particle addition compared to controls, even at 96 hours after MBA-AuNP addition, suggesting that MBA-AuNP themselves have no impact on cell proliferation and growth.

Using BafA1 we investigated the concentration and temporal effect on hESC, since previous studies had shown that an increase in lysosomal pH prevent endodermal differentiation. We assessed the effect of various concentrations of BafA1 on cell proliferation and growth, which showed that a concentration of 2nM was optimal as it only affected cell proliferation minimally. SERS was also carried out using MBA-AuNP on cells treated with BafA1 for 1h, 24h, 48h and 72h, to determine how the pH was affected within the lysosomes over time when treated with low or high concentrations of BafA1. As already observed in the proliferation assay, cells started dying extensively at the higher concentrations, but also showed a much stronger alkalisation of the lysosomes at the same time. A low chronic dose of 2nM was, however, able to cause significant alkalisation by 72h, by an average of around 0.52 pH units. This data supports the future usage of 2nM BafA1, which is a concentration similar to what has previously been used in the literature by Young *et al*, 2.5nM [97]. In the experiments performed by Young *et al*. mouse embryonic bodies were treated with a chronic low dose of 2.5nM BafA1 to see if this affected the mRNA concentration of endodermal markers. They did not however, assess the effect this low dose of BafA1 had on pH within the lysosomes. Future experiments would entail the differentiation of hESC into the three germ layers while under a chronic low dose of 2nM BafA1 to see if the change in mRNA levels also correlate to a change in pH. By utilising BafA1 in combination with other compounds such as ClioQ, which have been suggested to reacidify the lysosome, the connection between lysosomal pH and differentiation could be explored further, though this would require considerate optimisation of ClioQ culture and measurement conditions.

The experiments in the previous section also highlighted that MBA-AuNP may not be as sensitive as might be desired when measuring the pH within cellular organelles with low pH. As mentioned previously the MBA-AuNP sensors had a pK_a of around 7, which is where the sensor is most sensitive. The sensitivity levels off at the extremes, which means that the accuracy of individual pH measurements at very low and very high values diminishes. This means that it is necessary to acquire far more individual pH measurements at the extremes, and that the most accurate representation is to average the raw peak maximum or AUC values before the conversion into pH values from the calibration curve. If determination of pH values from individual clusters of MBA-AuNP are required, improvements to the pK_a of the sensor must be made – either by designing or identifying a more suitable pH responsive molecule or by exploring different analysis methods of the MBA-AuNP.

Lastly, we have applied the MBA-AuNP to a SVZ Batten disease model to demonstrate the capability of the sensor to measure lysosomal pH in a pathological setting with more subtle pH variations. The pH was shown to be significantly more alkaline in cells isolated from homozygous knockout sheep than both heterozygous and wild-type, which were at a similar pH level. SERS can therefore be used as a valid method to investigate pH in disease model studies, and by further optimising the pK_a of the pH sensor, easier and more accurate pH measurements from acidic organelles such as lysosomes can be made.

In conclusion, MBA-AuNP have shown potential for the measurement of pH within cells. However, there are several aspects which can be improved upon and experiments which could be conducted to further the research. With regards to the method itself it would be beneficial to assess more reporter molecules in addition to MBA, since the pK_a of MBA is not optimal for the measurement of pH within acidic cellular compartments. Further optimisation of the calibration method may also improve the sensitivity and accuracy of pH detection using the sensor, for example comprehensive comparison of all potential peak and peak ratios. To properly compare the method with other state of the art techniques - such as those involving the variety of pH-sensitive fluorophores - it would be important to also perform comparative experiments of the two techniques, which could directly highlight the advantages of one over the other. With regards to culture conditions of cells being measured, we have noted in our experiments that the medium itself plays a considerable role in the uptake of the AuNP and subsequently affects the ability to perform pH measurements. To properly apply this technique to a variety of cell types this would need to be considered, and it may be necessary to optimise culture conditions to prevent cell stress and to ensure sufficient particle uptake. This could be achieved either by optimising the media composition or by surface modifications of the MBA-AuNP themselves. As previously mentioned, a prototype environmental microscope culture chamber was created during this study but was not employed due to time constraints, 3D printing equipment failures, and budget. This chamber could have significantly improved the health of cells while under microscope conditions. Any future work could improve reliability and repeatability of pH measurements by employing a device of this type.

9 References

1. Swietach, P. What is pH regulation, and why do cancer cells need it? *Cancer Metastasis Rev.* **38**, 5–15 (2019) doi:10.1007/s10555-018-09778-x.

2. Lian, Y., Zhang, W., Ding, L., Zhang, X., Zhang, Y. & Wang, X. dong. Nanomaterials for Intracellular pH Sensing and Imaging. in *Novel Nanomaterials for Biomedical, Environmental and Energy Applications* 241–273 (2019). doi:10.1016/B978-0-12-814497-8.00008-4.

3. Putnam, R. W. Intracellular pH regulation. in *Cell Physiology Source Book* 303–321 (2012). doi:10.1016/B978-0-12-387738-3.00017-2.

4. Boron, W. F. Transport of H+ and of ionic weak acids and bases. *The Journal of Membrane Biology* vol. 72 at https://doi.org/10.1007/BF01870311 (1983) doi:10.1007/BF01870311.

5. Casey, J. R., Grinstein, S. & Orlowski, J. Sensors and regulators of intracellular pH. *Nature Reviews Molecular Cell Biology* vol. 11 50–61 at https://doi.org/10.1038/nrm2820 (2010) doi:10.1038/nrm2820.

6. Bizzarri, R. The Proton Sensitivity of Fluorescent Proteins: Towards Intracellular pH Indicators. in *Fluorescent Proteins II. Springer Series on Fluorescence* 59–97 (2011). doi:10.1007/4243_2011_30.

7. Loiselle, F. B. & Casey, J. R. Measurement of Intracellular pH. *Membr. Transp. Drug Discov. Dev. Methods Mol. Biol.* **637**, 311–331 (2010) doi:10.1007/978-1-60761-700-6_17.

8. Jaworska, A., Jamieson, L. E., Malek, K., Campbell, C. J., Choo, J., Chlopicki, S. & Baranska, M. SERS-based monitoring of the intracellular pH in endothelial cells: The influence of the extracellular environment and tumour necrosis factor-α. *Analyst* **140**, 2321–2329 (2015) doi:10.1039/c4an01988a.

9. Jaworska, A., Malek, K. & Kudelski, A. Intracellular pH – Advantages and pitfalls of surface-enhanced Raman scattering and fluorescence microscopy – A review. *Spectrochim. Acta - Part A Mol. Biomol. Spectrosc.* **251**, 1386–1425 (2021) doi:10.1016/j.saa.2020.119410.

10. Boron, W. F. Regulation of intracellular pH. *Am. J. Physiol. - Adv. Physiol. Educ.* **28**, 160–179 (2004) doi:10.1152/advan.00045.2004.

11. Han, J. & Burgess, K. Fluorescent indicators for intracellular pH. *Chem. Rev.* **110**, 2709–2728 (2010) doi:10.1021/cr900249z.

12. Masuda, A., Oyamada, M., Nagaoka, T., Tateishi, N. & Takamatsu, T. Regulation of cytosol-nucleus pH gradients by K+/H+ exchange mechanism in the nuclear envelope of neonatal rat astrocytes. *Brain Res.* **807**, 70–77 (1998) doi:10.1016/S0006-8993(98)00737-9.

13. Fang, B., Wang, D., Huang, M., Yu, G. & Li, H. Hypothesis on the relationship

between the change in intracellular pH and incidence of sporadic alzheimer's disease or vascular dementia. *International Journal of Neuroscience* vol. 120 591–595 at https://doi.org/10.3109/00207454.2010.505353 (2010) doi:10.3109/00207454.2010.505353.

14. Jiang, Y., Sato, Y., Im, E., Berg, M., Bordi, M., Darji, S., Kumar, A., Mohan, P. S., Bandyopadhyay, U., Diaz, A., Cuervo, A. M. & Nixon, R. A. Lysosomal dysfunction in down syndrome is app-dependent and mediated by APP-βCTF (c99). *J. Neurosci.* **39**, 5255–5268 (2019) doi:10.1523/JNEUROSCI.0578-19.2019.

15. Colacurcio, D. J. & Nixon, R. A. Disorders of lysosomal acidification—The emerging role of v-ATPase in aging and neurodegenerative disease. *Ageing Research Reviews* vol. 32 75–88 at https://doi.org/10.1016/j.arr.2016.05.004 (2016) doi:10.1016/j.arr.2016.05.004.

16. Webb, B. A., Chimenti, M., Jacobson, M. P. & Barber, D. L. Dysregulated pH: A perfect storm for cancer progression. *Nature Reviews Cancer* vol. 11 671–677 at https://doi.org/10.1038/nrc3110 (2011) doi:10.1038/nrc3110.

17. Koltai, T. Cancer: Fundamentals behind pH targeting and the double-edged approach. *Onco. Targets. Ther.* **9**, 6343—6360 (2016) doi:10.2147/OTT.S115438.

18. Thomson, J. A. Embryonic stem cell lines derived from human blastocysts. *Science (80-.).* **282**, 1145–1147 (1998) doi:10.1126/science.282.5391.1145.

19. Takahashi, K. & Yamanaka, S. Induction of Pluripotent Stem Cells from Mouse Embryonic and Adult Fibroblast Cultures by Defined Factors. *Cell* **126**, 663–676 (2006) doi:10.1016/j.cell.2006.07.024.

20. Takahashi, K., Tanabe, K., Ohnuki, M., Narita, M., Ichisaka, T., Tomoda, K. & Yamanaka, S. Induction of Pluripotent Stem Cells from Adult Human Fibroblasts by Defined Factors. *Cell* **131**, 861–872 (2007) doi:10.1016/j.cell.2007.11.019.

21. Baker, D. E. C., Harrison, N. J., Maltby, E., Smith, K., Moore, H. D., Shaw, P. J., Heath, P. R., Holden, H. & Andrews, P. W. Adaptation to culture of human embryonic stem cells and oncogenesis in vivo. *Nat. Biotechnol.* **25**, 207–215 (2007) doi:10.1038/nbt1285.

22. Amps, K., Andrews, P. W., Anyfantis, G., Armstrong, L., Avery, S., Baharvand, H., Baker, J., Baker, D., Munoz, M. B., Beil, S., Benvenisty, N., Ben-Yosef, D., Biancotti, J.-C., Bosman, A., Brena, R. M., Brison, D., Caisander, G., Camarasa, M. V, Chen, J., *et al.* Screening ethnically diverse human embryonic stem cells identifies a chromosome 20 minimal amplicon conferring growth advantage. *Nat. Biotechnol.* **29**, 1132–1144 (2011) doi:10.1038/nbt.2051.

23. Pells, S., Koutsouraki, E., Morfopoulou, S., Valencia-Cadavid, S., Tomlinson, S. R., Kalathur, R., Futschik, M. E. & De Sousa, P. a. Novel Human Embryonic Stem

Cell Regulators Identified by Conserved and Distinct CpG Island Methylation State. *PLoS One* **10**, e0131102 (2015) doi:10.1371/journal.pone.0131102.

24. Wang, L., Han, X., Qu, G., Su, L., Zhao, B. & Miao, J. A pH probe inhibits senescence in mesenchymal stem cells. *Stem Cell Res. Ther.* **9**, (2018) doi:10.1186/s13287-018-1081-0.

25. Li, H., Collado, M., Villasante, A., Strati, K., Ortega, S., Cãamero, M., Blasco, M. A. & Serrano, M. The Ink4/Arf locus is a barrier for iPS cell reprogramming. *Nature* **460**, 1136–1139 (2009) doi:10.1038/nature08290.

26. Phanthong, P., Raveh-Amit, H., Li, T., Kitiyanant, Y. & Dinnyes, A. Is aging a barrier to reprogramming? Lessons from induced pluripotent stem cells. *Biogerontology* vol. 14 591–602 at https://doi.org/10.1007/s10522-013-9455-2 (2013) doi:10.1007/s10522-013-9455-2.

27. Wang, B., Miyagoe-Suzuki, Y., Yada, E., Ito, N., Nishiyama, T., Nakamura, M., Ono, Y., Motohashi, N., Segawa, M., Masuda, S. & Takeda, S. Reprogramming efficiency and quality of induced pluripotent stem cells (ipscs) generated from muscle-derived fibroblasts of mdx mice at different ages. *PLoS Curr.* RRN1274 (2011) doi:10.1371/currents.RRN1274.

28. Cheng, Z., Ito, S., Nishio, N., Xiao, H., Zhang, R., Suzuki, H., Okawa, Y., Murohara, T. & Isobe, K. I. Establishment of induced pluripotent stem cells from aged mice using bone marrow-derived myeloid cells. *J. Mol. Cell Biol.* **3**, 91–98 (2011) doi:10.1093/jmcb/mjq044.

29. Chao, S. C., Wu, G. J., Huang, S. F., Dai, N. T., Huang, H. K., Chou, M. F., Tsai, Y. T., Lee, S. P. & Loh, S. H. Functional and molecular mechanism of intracellular pH regulation in human inducible pluripotent stem cells. *World J. Stem Cells* **10**, 196–211 (2018) doi:10.4252/wjsc.v10.i12.196.

30. Ulmschneider, B., Grillo-Hill, B. K., Benitez, M., Azimova, D. R., Barber, D. L. & Nystul, T. G. Increased intracellular pH is necessary for adult epithelial and embryonic stem cell differentiation. *Journal of Cell Biology* vol. 215 345–355 at https://doi.org/10.1083/jcb.201606042 (2016) doi:10.1083/jcb.201606042.

31. Raman, C. V. & Krishnan, K. S. A new type of secondary radiation [11]. *Nature* vol. 121 501–502 at https://doi.org/10.1038/121501c0 (1928) doi:10.1038/121501c0.

32. Bantz, K. C., Meyer, A. F., Wittenberg, N. J., Im, H., Kurtuluş, O., Lee, S. H., Lindquist, N. C., Oh, S.-H. & Haynes, C. L. Recent progress in SERS biosensing. *Phys. Chem. Chem. Phys.* **13**, 11551–11567 (2011) doi:10.1039/c0cp01841d.

33. Smith, E. & Dent, G. Surface-Enhanced Raman Scattering and Surface-Enhanced Resonance Raman Scattering. *Mod. Raman Spectrosc. - A Pract. Approach* 113–133 (2004) doi:10.1002/0470011831.

34. Bumbrah, G. S. & Sharma, R. M. Raman spectroscopy – Basic principle,

instrumentation and selected applications for the characterization of drugs of abuse. *Egypt. J. Forensic Sci.* **6**, 209–215 (2016) doi:10.1016/j.ejfs.2015.06.001.

35. Langer, J., de Aberasturi, D. J., Aizpurua, J., Alvarez-Puebla, R. A., Auguié, B., Baumberg, J. J., Bazan, G. C., Bell, S. E. J., Boisen, A., Brolo, A. G., Choo, J., Cialla-May, D., Deckert, V., Fabris, L., Faulds, K., Javier García de Abajo, F., Goodacre, R., Graham, D., Haes, A. J., *et al.* Present and future of surface-enhanced Raman scattering. *ACS Nano* vol. 14 28–117 at https://doi.org/10.1021/acsnano.9b04224 (2020) doi:10.1021/acsnano.9b04224.

36. Le Ru, E. C. & Etchegoin, P. G. SERS enhancement factors and related topics. *Princ. Surface-Enhanced Raman Spectrosc.* 185–264 (2009) doi:10.1016/B978-0-444-52779-0.X0001-3.

37. Ochsenkühn, M. A., Jess, P. R. T., Stoquert, H., Dholakia, K. & Campbell, C. J. Nanoshells for surface-enhanced raman spectroscopy in eukaryotic cells: Cellular response and sensor development. *ACS Nano* **3**, 3613–3621 (2009) doi:10.1021/nn900681c.

38. Jing, Y., Wang, R., Wang, Q., Xiang, Z., Li, Z., Gu, H. & Wang, X. An overview of surface-enhanced Raman scattering substrates by pulsed laser deposition technique: fundamentals and applications. *Advanced Composites and Hybrid Materials* vol. 4 885–905 at https://doi.org/10.1007/s42114-021-00330-0 (2021) doi:10.1007/s42114-021-00330-0.

39. Smith, R., Wright, K. L. & Ashton, L. Raman spectroscopy: An evolving technique for live cell studies. *Analyst* vol. 141 3590–3600 at https://doi.org/10.1039/c6an00152a (2016) doi:10.1039/c6an00152a.

40. Palonpon, A. F., Ando, J., Yamakoshi, H., Dodo, K., Sodeoka, M., Kawata, S. & Fujita, K. Raman and SERS microscopy for molecular imaging of live cells. *Nat. Protoc.* **8**, 677–692 (2013) doi:10.1038/nprot.2013.030.

41. Jiang, J., Auchinvole, C., Fisher, K. & Campbell, C. J. Quantitative measurement of redox potential in hypoxic cells using SERS nanosensors. *Nanoscale* 12104–12110 (2014) doi:10.1039/C4NR01263A.

42. Jamieson, L. E., Jaworska, A., Jiang, J., Baranska, M., Harrison, D. J. & Campbell, C. J. Simultaneous intracellular redox potential and pH measurements in live cells using SERS nanosensors. *Analyst* **140**, 2330–2335 (2015) doi:10.1039/C4AN02365J.

43. Capocefalo, A., Mammucari, D., Brasili, F., Fasolato, C., Bordi, F., Postorino, P. & Domenici, F. Exploring the potentiality of a SERS-active pH nano-biosensor. *Front. Chem.* **7**, (2019) doi:10.3389/fchem.2019.00413.

44. Auchinvole, C. A. R., Richardson, P., McGuinnes, C., Mallikarjun, V., Donaldson, K., McNab, H. & Campbell, C. J. Monitoring intracellular redox potential changes using SERS nanosensors. *ACS Nano* **6**, 888–896 (2012)

doi:10.1021/nn204397q.

45. Chávez, J. C., Darszon, A., Treviño, C. L. & Nishigaki, T. Quantitative Intracellular pH Determinations in Single Live Mammalian Spermatozoa Using the Ratiometric Dye SNARF-5F. *Front. Cell Dev. Biol.* **7**, (2020) doi:10.3389/fcell.2019.00366.

46. Paradiso, A. M., Tsien, R. Y. & Machen, T. E. Na+-H+ exchange in gastric glands as measured with a cytoplasmic-trapped, fluorescent pH indicator. *Proc. Natl. Acad. Sci. U. S. A.* **81**, 7436–7440 (1984) doi:10.1073/pnas.81.23.7436.

47. Nishigaki, T., Wood, C. D., Shiba, K., Baba, S. A. & Darszon, A. Stroboscopic illumination usine light-emitting diodes reduces phototoxicity in fluorescence cell imaging. *Biotechniques* **41**, (2006) doi:10.2144/000112220.

48. Abpbio.com. BCECF. https://www.abpbio.com/product/bcecf/ (2022).

49. Liu, J., Diwu, Z. & Leung, W. Y. Synthesis and photophysical properties of new fluorinated benzo[c]xanthene dyes as intracellular pH indicators. *Bioorganic Med. Chem. Lett.* **11**, 2903–2905 (2001) doi:10.1016/S0960-894X(01)00595-9.

50. Ramshesh, V. K. & Lemasters, J. J. Imaging of mitochondrial pH using SNARF-1. *Methods Mol. Biol.* **810**, 243–248 (2012) doi:10.1007/978-1-61779-382-0_16.

51. Tiemeier, G. L., de Koning, R., Wang, G., Kostidis, S., Rietjens, R. G. J., Sol, W. M. P. J., Dumas, S. J., Giera, M., van den Berg, C. W., Eikenboom, J. C. J., van den Berg, B. M., Carmeliet, P. & Rabelink, T. J. Lowering the increased intracellular pH of human-induced pluripotent stem cell-derived endothelial cells induces formation of mature Weibel-Palade bodies. *Stem Cells Transl. Med.* **9**, 758–772 (2020) doi:10.1002/sctm.19-0392.

52. Clear, K. J., Virga, K., Gray, L. & Smith, B. D. Using membrane composition to fine-tune the pKa of an optical liposome pH sensor. *J. Mater. Chem. C* **4**, 2925–2930 (2016) doi:10.1039/c5tc03480a.

53. Wencel, D., Abel, T. & McDonagh, C. Optical chemical pH sensors. *Analytical Chemistry* vol. 86 15–29 at https://doi.org/10.1021/ac4035168 (2014) doi:10.1021/ac4035168.

54. Thivierge, C., Han, J., Jenkins, R. M. & Burgess, K. Fluorescent proton sensors based on energy transfer. *J. Org. Chem.* **76**, 5219–5228 (2011) doi:10.1021/jo2005654.

55. Wang, F., Widejko, R. G., Yang, Z., Nguyen, K. T., Chen, H., Fernando, L. P., Christensen, K. A. & Anker, J. N. Surface-enhanced Raman scattering detection of pH with silica-encapsulated 4-mercaptobenzoic acid-functionalized silver nanoparticles. *Anal. Chem.* **84**, 8013–8019 (2012) doi:10.1021/ac3018179.

56. Bi, Y., Di, H., Zeng, E., Li, Q., Li, W., Yang, J. & Liu, D. Reliable Quantification of pH Variation in Live Cells Using Prussian Blue-Caged Surface-Enhanced Raman Scattering Probes. *Anal. Chem.* **92**, 9574–9582 (2020)

doi:10.1021/acs.analchem.0c00714.

57. Law, S. M., Stanfield, S. J., Hardisty, G. R., Dransfield, I., Campbell, C. J. & Gray, R. D. Human cystic fibrosis monocyte derived macrophages display no defect in acidification of phagolysosomes when measured by optical nanosensors. *J. Cyst. Fibros.* **19**, 203–210 (2020) doi:10.1016/j.jcf.2019.09.003.

58. Jamieson, L. E., Camus, V. L., Bagnaninchi, P. O., Fisher, K. M., Stewart, G. D., Nailon, W. H., McLaren, D. B., Harrison, D. J. & Campbell, C. J. Targeted SERS nanosensors measure physicochemical gradients and free energy changes in live 3D tumor spheroids. *Nanoscale* **8**, 16710–16718 (2016) doi:10.1039/c6nr06031e.

59. Kneipp, J., Kneipp, H., Wittig, B. & Kneipp, K. Following the dynamics of pH in endosomes of live cells with SERS nanosensors. *J. Phys. Chem. C* **114**, 7421–7426 (2010) doi:10.1021/jp910034z.

60. Schwartzberg, A. M., Oshiro, T. Y., Zhang, J. Z., Huser, T. & Talley, C. E. Improving nanoprobes using surface-enhanced Raman scattering from 30-nm hollow gold particles. *Anal. Chem.* **78**, 4732–4736 (2006) doi:10.1021/ac060220g.

61. Zhang, Y., de Aberasturi, D. J., Henriksen-Lacey, M., Langer, J. & Liz-Marzan, L. M. Live-cell surface-enhanced Raman spectroscopy imaging of intracellular pH: From two dimensions to three dimensions. *ACS Sensors* **5**, 3194–3206 (2020) doi:10.1021/acssensors.0c01487.

62. Zhang, Q., Wen, H., Watanabe, K., Kotani, I., Ricci, M., Fortuni, B., Dao, A. T. N., Masuhara, A., Hirai, K., Kasai, H., Inose, T. & Uji-I, H. Low-Cytotoxic Gold-Coated Silver Nanoflowers for Intracellular pH Sensing. *ACS Appl. Nano Mater.* **3**, 7643–7650 (2020) doi:10.1021/acsanm.0c01278.

63. Pallaoro, A., Braun, G. B., Reich, N. O. & Moskovits, M. Mapping Local pH in live cells using encapsulated fluorescent SERS nanotags. *Small* **6**, 618–622 (2010) doi:10.1002/smll.200901893.

64. Zheng, X. S., Hu, P., Cui, Y., Zong, C., Feng, J. M., Wang, X. & Ren, B. BSA-coated nanoparticles for improved SERS-based intracellular pH sensing. *Anal. Chem.* **86**, 12250–12257 (2014) doi:10.1021/ac503404u.

65. Bi, L., Wang, Y., Yang, Y., Li, Y., Mo, S., Zheng, Q. & Chen, L. Highly Sensitive and Reproducible SERS Sensor for Biological pH Detection Based on a Uniform Gold Nanorod Array Platform. *ACS Appl. Mater. Interfaces* **10**, 15381–15387 (2018) doi:10.1021/acsami.7b19347.

66. Huang, Y., Liu, W., Wang, D., Gong, Z. & Fan, M. Evaluation of the intrinsic pH sensing performance of surface-enhanced Raman scattering pH probes. *Microchem. J.* **154**, 104565 (2020) doi:10.1016/j.microc.2019.104565.

67. Jahn, I. J., Mühlig, A. & Cialla-May, D. Application of molecular SERS

nanosensors: where we stand and where we are headed towards? *Anal. Bioanal. Chem.* **412**, 5999–6007 (2020) doi:10.1007/s00216-020-02779-2.

68. Sero, J. E. & Stevens, M. M. Nanoneedle-Based Materials for Intracellular Studies. in *Advances in Experimental Medicine and Biology* vol. 1295 191–219 (2021). doi:10.1007/978-3-030-58174-9_9.

69. Chiappini, C., Martinez, J. O., De Rosa, E., Almeida, C. S., Tasciotti, E. & Stevens, M. M. Biodegradable nanoneedles for localized delivery of nanoparticles in vivo: Exploring the biointerface. *ACS Nano* **9**, 5500–5509 (2015) doi:10.1021/acsnano.5b01490.

70. Pan, C., Li, X., Sun, J., Li, Z., Zhang, L., Qian, W., Wang, P. & Dong, J. A Multiplexed SERS-Active Microneedle for Simultaneous Redox Potential and pH Measurements in Rat Joints. *ACS Appl. Bio Mater.* **2**, 2102–2108 (2019) doi:10.1021/acsabm.9b00117.

71. Antonenko, Y. N. & Bulychev, A. A. Measurements of local pH changes near bilayer lipid membrane by means of a pH microelectrode and a protonophore-dependent membrane potential. Comparison of the methods. *Biochim. Biophys. Acta - Biomembr.* **1070**, 279–282 (1991) doi:10.1016/0005-2736(91)90176-9.

72. Martel, S., Clément, J. L., Muller, A., Culcasi, M. & Pietri, S. Synthesis and 31P NMR characterization of new low toxic highly sensitive pH probes designed for in vivo acidic pH studies. *Bioorganic Med. Chem.* **10**, 1451–1458 (2002) doi:10.1016/S0968-0896(01)00414-X.

73. Hesse, S. J. A., Ruijter, G. J. G., Dijkema, C. & Visser, J. Measurement of intracellular (compartmental) pH by 31P NMR in Aspergillus niger. in *Journal of Biotechnology* vol. 77 5–15 (2000). doi:10.1016/S0168-1656(99)00203-5.

74. Lutz, N. W., Fur, Y. Le, Chiche, J., Pouysse, J. & Cozzone, P. J. Quantitative in vivo characterization of intracellular and extracellular pH profiles in heterogeneous tumors: A novel method enabling multiparametric pH analysis. *Cancer Res.* **73**, 4616–4628 (2013) doi:10.1158/0008-5472.CAN-13-0767.

75. Perruchoud, L. H., Jones, M. D., Sutrisno, A., Zamble, D. B., Simpson, A. J. & Zhang, X. A. A ratiometric NMR pH sensing strategy based on a slow-proton-exchange (SPE) mechanism. *Chem. Sci.* **6**, 6305–6311 (2015) doi:10.1039/c5sc02145f.

76. Cytodiagnostics.com. Gold Nanoparticle Properties. https://www.cytodiagnostics.com/pages/gold-nanoparticle-properties (2022).

77. Van Diggelen, O. P., Keulemans, J. L. M., Winchester, B., Hofman, I. L., Vanhanen, S. L., Santavuori, P. & Voznyi, Y. V. A rapid fluorogenic palmitoyl-protein thioesterase assay: Pre- and postnatal diagnosis of INCL. in *Molecular Genetics and Metabolism* vol. 66 240–244 (1999).

doi:10.1006/mgme.1999.2809.

78. Fleming, H., McAughtrie, S., Mills, B., Tanner, M. G., Marks, A. & Campbell, C. J. Dual purpose fibre-SERS pH sensing and bacterial analysis. *Analyst* **143**, 5918–5925 (2018) doi:10.1039/c8an01322e.

79. Bando, K., Zhang, Z., Graham, D., Faulds, K., Fujita, K. & Kawata, S. Dynamic pH measurements of intracellular pathways using nano-plasmonic assemblies. *Analyst* **145**, 5768–5775 (2020) doi:10.1039/d0an00986e.

80. Scarpitti, B. T., Morrison, A. M., Buyanova, M. & Schultz, Z. D. Comparison of 4-Mercaptobenzoic Acid Surface-Enhanced Raman Spectroscopy-Based Methods for pH Determination in Cells. *Appl. Spectrosc.* **74**, 1423–1432 (2020) doi:10.1177/0003702820950768.

81. Puppulin, L., Hosogi, S., Sun, H., Matsuo, K., Inui, T., Kumamoto, Y., Suzaki, T., Tanaka, H. & Marunaka, Y. Bioconjugation strategy for cell surface labelling with gold nanostructures designed for highly localized pH measurement. *Nat. Commun.* **9**, 1–16 (2018) doi:10.1038/s41467-018-07726-5.

82. Michota, A. & Bukowska, J. Surface-enhanced Raman scattering (SERS) of 4-mercaptobenzoic acid on silver and gold substrates. *J. Raman Spectrosc.* **34**, 21–25 (2003) doi:10.1002/jrs.928.

83. Ma, C. & Harris, J. M. Surface-enhanced raman spectroscopy investigation of the potential-dependent acid-base chemistry of silver-immobilized 2-mercaptobenzoic acid. *Langmuir* **27**, 3527–3533 (2011) doi:10.1021/la1044859.

84. Wei, H., Willner, M. R., Marr, L. C. & Vikesland, P. J. Highly stable SERS pH nanoprobes produced by co-solvent controlled AuNP aggregation. *Analyst* **141**, 5159–5169 (2016) doi:10.1039/c6an00650g.

85. Williams, A., Flynn, K. J., Xia, Z. & Dunstan, P. R. Multivariate spectral analysis of pH SERS probes for improved sensing capabilities. *J. Raman Spectrosc.* **47**, 819–827 (2016) doi:10.1002/jrs.4910.

86. Huefner, A., Septiadi, D., Wilts, B. D., Patel, I. I., Kuan, W. L., Fragniere, A., Barker, R. A. & Mahajan, S. Gold nanoparticles explore cells: Cellular uptake and their use as intracellular probes. *Methods* **68**, 354–363 (2014) doi:10.1016/j.ymeth.2014.02.006.

87. Kapara, A., Brunton, V., Graham, D. & Faulds, K. Investigation of cellular uptake mechanism of functionalised gold nanoparticles into breast cancer using SERS. *Chem. Sci.* **11**, 5819–5829 (2020) doi:10.1039/d0sc01255f.

88. Tkachenko, A. G., Xie, H., Liu, Y., Coleman, D., Ryan, J., Glomm, W. R., Shipton, M. K., Franzen, S. & Feldheim, D. L. Cellular trajectories of peptide-modified gold particle complexes: Comparison of nuclear localization signals and peptide transduction domains. *Bioconjug. Chem.* **15**, 482–490 (2004)

doi:10.1021/bc034189q.

89. Behzadi, S., Serpooshan, V., Tao, W., Hamaly, M. A., Alkawareek, M. Y., Dreaden, E. C., Brown, D., Alkilany, A. M., Farokhzad, O. C. & Mahmoudi, M. Cellular uptake of nanoparticles: Journey inside the cell. *Chemical Society Reviews* vol. 46 4218–4244 at https://doi.org/10.1039/c6cs00636a (2017) doi:10.1039/c6cs00636a.

90. Schaks, M., Giannone, G. & Rottner, K. Actin dynamics in cell migration. *Essays Biochem.* **63**, 483–495 (2019) doi:10.1042/EBC20190015.

91. Liu, M., Li, Q., Liang, L., Li, J., Wang, K., Li, J., Lv, M., Chen, N., Song, H., Lee, J., Shi, J., Wang, L., Lal, R. & Fan, C. Real-Time visualization of clustering and intracellular transport of gold nanoparticles by correlative imaging. *Nat. Commun.* **8**, 15646 (2017) doi:10.1038/ncomms15646.

92. Eskelinen, E. L. Roles of LAMP-1 and LAMP-2 in lysosome biogenesis and autophagy. *Molecular Aspects of Medicine* vol. 27 495–502 at https://doi.org/10.1016/j.mam.2006.08.005 (2006) doi:10.1016/j.mam.2006.08.005.

93. Bowman, E. J., Siebers, A. & Altendorf, K. Bafilomycins; A class of inhibitors of membrane ATPases from microorganisms, animal cells, and plant cells. *Proc. Natl. Acad. Sci. U. S. A.* **85**, 7972–7976 (1988) doi:10.1073/pnas.85.21.7972.

94. Yoshimori, T., Yamamoto, A., Moriyama, Y., Futai, M. & Tashiro, Y. Bafilomycin A1, a specific inhibitor of vacuolar-type H+-ATPase, inhibits acidification and protein degradation in lysosomes of cultured cells. *J. Biol. Chem.* **266**, 17707–17712 (1991) doi:10.1016/s0021-9258(19)47429-2.

95. Seo, B. R., Lee, S. J., Cho, K. S., Yoon, Y. H. & Koh, J. Y. The zinc ionophore clioquinol reverses autophagy arrest in chloroquine-treated ARPE-19 cells and in APP/mutant presenilin-1-transfected Chinese hamster ovary cells. *Neurobiol. Aging* **36**, 3228–3238 (2015) doi:10.1016/j.neurobiolaging.2015.09.006.

96. Koh, J. Y., Kim, H. N., Hwang, J. J., Kim, Y. H. & Park, S. E. Lysosomal dysfunction in proteinopathic neurodegenerative disorders: Possible therapeutic roles of cAMP and zinc. *Molecular Brain* vol. 12 at https://doi.org/10.1186/s13041-019-0439-2 (2019) doi:10.1186/s13041-019-0439-2.

97. Young, N. P., Kamireddy, A., Van Nostrand, J. L., Eichner, L. J., Shokhirev, M. N., Dayn, Y. & Shaw, R. J. AMPK governs lineage specification through Tfeb-dependent regulation of lysosomes. *Genes Dev.* **30**, 535–552 (2016) doi:10.1101/gad.274142.115.

98. Villegas, F., Lehalle, D., Mayer, D., Rittirsch, M., Stadler, M. B., Zinner, M., Olivieri, D., Vabres, P., Duplomb-Jego, L., De Bont, E. S. J. M., Duffourd, Y., Duijkers, F., Avila, M., Geneviève, D., Houcinat, N., Jouan, T., Kuentz, P., Lichtenbelt, K. D., Thauvin-Robinet, C., *et al.* Lysosomal Signaling Licenses

Embryonic Stem Cell Differentiation via Inactivation of Tfe3. *Cell Stem Cell* **24**, 257–270 (2019) doi:10.1016/j.stem.2018.11.021.

99. Andrejewski, N., Punnonen, E. L., Guhde, G., Tanaka, Y., Lüllmann-Rauch, R., Hartmann, D., Von Figura, K. & Saftig, P. Normal lysosomal morphology and function in LAMP-1-deficient mice. *J. Biol. Chem.* **274**, 12692–12701 (1999) doi:10.1074/jbc.274.18.12692.

100. Tanaka, Y., Guhde, G., Suter, A., Eskelinen, E. L., Hartmann, D., Lüllmann-Rauch, R., Janssen, P. M. L., Blanz, J., Von Figura, K. & Saftig, P. Accumulation of autophagic vacuoles and cardiomyopathy LAMP-2-deficient mice. *Nature* **406**, 902–906 (2000) doi:10.1038/35022595.

101. Endo, Y., Furuta, A. & Nishino, I. Danon disease: a phenotypic expression of LAMP-2 deficiency. *Acta Neuropathologica* vol. 129 391–398 at https://doi.org/10.1007/s00401-015-1385-4 (2015) doi:10.1007/s00401-015-1385-4.

102. Furuta, K., Yang, X. L., Chen, J. S., Hamilton, S. R. & August, J. T. Differential expression of the lysosome-associated membrane proteins in normal human tissues. *Arch. Biochem. Biophys.* **365**, 183–195 (1999) doi:10.1006/abbi.1999.1147.

103. Cesbron, Y., Shaheen, U., Free, P. & Lévy, R. TAT and HA2 facilitate cellular uptake of gold nanoparticles but do not lead to cytosolic localisation. *PLoS One* **10**, e0121683 (2015) doi:10.1371/journal.pone.0121683.

104. Lacar, B., Young, S. Z., Platel, J.-C., Bordey, A., Vaccarino, F. M. & Szele, F. G. Imaging and recording subventricular zone progenitor cells in live tissue of postnatal mice. *Front. Neurosci.* **4:43**, (2010) doi:10.3389/fnins.2010.00043.

105. Johnson, T. B., Cain, J. T., White, K. A., Ramirez-Montealegre, D., Pearce, D. A. & Weimer, J. M. Therapeutic landscape for Batten disease: current treatments and future prospects. *Nature Reviews Neurology* vol. 15 161–178 at https://doi.org/10.1038/s41582-019-0138-8 (2019) doi:10.1038/s41582-019-0138-8.

106. Seehafer, S. S. & Pearce, D. A. Spectral properties and mechanisms that underlie autofluorescent accumulations in Batten disease. *Biochem. Biophys. Res. Commun.* **382**, 247–251 (2009) doi:10.1016/j.bbrc.2009.02.099.

107. Golabek, A. A., Kida, E., Walus, M., Kaczmarski, W., Michalewski, M. & Wisniewski, K. E. CLN3 protein regulates lysosomal pH and alters intracellular processing of alzheimer's amyloid-β protein precursor and cathepsin D in human cells. *Mol. Genet. Metab.* **70**, 203–213 (2000) doi:10.1006/mgme.2000.3006.

108. Mukherjee, A. B., Appu, A. P., Sadhukhan, T., Casey, S., Mondal, A., Zhang, Z. & Bagh, M. B. Emerging new roles of the lysosome and neuronal ceroid lipofuscinoses. *Molecular Neurodegeneration* vol. 14 at

https://doi.org/10.1186/s13024-018-0300-6 (2019) doi:10.1186/s13024-018-0300-6.

109. Appu, A. P., Bagh, M. B., Sadhukhan, T., Mondal, A., Casey, S. & Mukherjee, A. B. Cln3-mutations underlying juvenile neuronal ceroid lipofuscinosis cause significantly reduced levels of Palmitoyl-protein thioesterases-1 (Ppt1)-protein and Ppt1-enzyme activity in the lysosome. *J. Inherit. Metab. Dis.* **42**, 944–954 (2019) doi:10.1002/jimd.12106.

110. Bozorg, S., Ramirez-Montealegre, D., Chung, M. & Pearce, D. A. Juvenile Neuronal Ceroid Lipofuscinosis (JNCL) and the Eye. *Survey of Ophthalmology* vol. 54 463–471 at https://doi.org/10.1016/j.survophthal.2009.04.007 (2009) doi:10.1016/j.survophthal.2009.04.007.

111. Croce, A. C. & Bottiroli, G. Autofluorescence spectroscopy and imaging: A tool for biomedical research and diagnosis. *Eur. J. Histochem.* **58**, (2014) doi:10.4081/ejh.2014.2461.

112. Di Guardo, G. Lipofuscin, lipofuscin-like pigments and autofluorescence. *Eur. J. Histochem.* **59**, (2015) doi:10.4081/ejh.2015.2485.

113. Armstrong, Gum, G., Webb, A. & Jolly, R. Quantitative autofluorescence in the ovine and canine ocular fundus in ceroid-lipofuscinosis (Batten's disease). *Vet. Res. Commun.* **12**, 453–456 (1988) doi:10.1007/BF01075474.

114. Atiskova, Y., Bartsch, S., Danyukova, T., Becker, E., Hagel, C., Storch, S. & Bartsch, U. Mice deficient in the lysosomal enzyme palmitoyl-protein thioesterase 1 (PPT1) display a complex retinal phenotype. *Sci. Rep.* **9**, 14185 (2019) doi:10.1038/s41598-019-50726-8.

115. Sheth, J., Mistri, M., Bhavsar, R., Pancholi, D., Kamate, M., Gupta, N., Kabra, M., Mehta, S., Nampoothiri, S., Thakker, A., Jain, V., Shah, R. & Sheth, F. Batten disease: Biochemical and molecular characterization revealing novel PPT1 and TPP1 gene mutations in Indian patients. *BMC Neurol.* **18**, 203 (2018) doi:10.1186/s12883-018-1206-1.

116. Yu, L., McPhee, C. K., Zheng, L., Mardones, G. A., Rong, Y., Peng, J., Mi, N., Zhao, Y., Liu, Z., Wan, F., Hailey, D. W., Oorschot, V., Klumperman, J., Baehrecke, E. H. & Lenardo, M. J. Termination of autophagy and reformation of lysosomes regulated by mTOR. *Nature* **465**, 942–946 (2010) doi:10.1038/nature09076.

117. Webb, B. A., Cook, J., Wittmann, T. & Barber, D. L. pHLARE: A genetically encoded ratiometric lysosome ph biosensor. *bioRxiv* (2020) doi:10.1101/2020.06.03.132720.

118. Seehafer, S. S. & Pearce, D. A. You say lipofuscin, we say ceroid: Defining autofluorescent storage material. *Neurobiology of Aging* vol. 27 576–588 at https://doi.org/10.1016/j.neurobiolaging.2005.12.006 (2006) doi:10.1016/j.neurobiolaging.2005.12.006.

119. Bandyopadhyay, U., Nagy, M., Fenton, W. A. & Horwich, A. L. Absence of lipofuscin in motor neurons of SOD1-linked ALS mice. *Proc. Natl. Acad. Sci. U. S. A.* **111**, 11055–11060 (2014) doi:10.1073/pnas.1409314111.

120. Zhou, H., Gong, X., Lin, H., Chen, H., Huang, D., Li, D., Shan, H. & Gao, J. Gold nanoparticles impair autophagy flux through shape-dependent endocytosis and lysosomal dysfunction. *J. Mater. Chem. B* **6**, 8127–8136 (2018) doi:10.1039/c8tb02390e.

121. Kim, C. S., Li, X., Jiang, Y., Yan, B., Tonga, G. Y., Ray, M., Solfiell, D. J. & Rotello, V. M. Cellular imaging of endosome entrapped small gold nanoparticles. *MethodsX* **2**, 306–315 (2015) doi:10.1016/j.mex.2015.06.001.

122. Shen, Y., Liang, L., Zhang, S., Huang, D., Zhang, J., Xu, S., Liang, C. & Xu, W. Organelle-targeting surface-enhanced Raman scattering (SERS) nanosensors for subcellular pH sensing. *Nanoscale* **10**, 1622–1630 (2018) doi:10.1039/c7nr08636a.

123. Liu, G., Li, Q., Ni, W., Zhang, N., Zheng, X., Wang, Y., Shao, D. & Tai, G. Cytotoxicity of various types of gold-mesoporous silica nanoparticles in human breast cancer cells. *Int. J. Nanomedicine* **10**, 6075—6087 (2015) doi:10.2147/IJN.S90887.

124. Kah, J. C. Y., Olivo, M. C., Lee, C. G. L. & Sheppard, C. J. R. Molecular contrast of EGFR expression using gold nanoparticles as a reflectance-based imaging probe. *Mol. Cell. Probes* **22**, 14–23 (2008) doi:10.1016/j.mcp.2007.06.010.